SHEAR-WAVE VELOCITY STRUCTURE IN THE CRUST AND UPPER MANTLE BENEATH THE CENTRAL TIEN SHAN FROM SURFACE-WAVE TOMOGRAPHY

A Dissertation Presented to

The Faculty of the Department of Earth and Atmospheric Sciences

University of Houston

In Partial Fulfillment

of the Requirements for the Degree

Doctor of Philosophy

By

Arianna Lisi

May 2014

SHEAR-WAVE VELOCITY STRUCTURE IN THE CRUST AND UPPER MANTLE BENEATH THE CENTRAL TIEN SHAN FROM SURFACE-WAVE TOMOGRAPHY

Arianna Lisi

APPROVED

Dr. Aibing Li

Dr. Stuart A. Hall

Dr. Michael Murphy

Dr. Fenglin Niu

Dean, College of Natural Sciences and Mathematics

ACKNOWLEDGEMENTS

My special thanks go to Dr. Aibing Li for her constant support and encouragement that was really helpful for me throughout all these years. Her teaching and contributions to this thesis have been really precious to conclude this study. I would also like to thank Dr. Mike Murphy for the helpful discussion I had with him. I wish to thank S. Roecker for collecting the seismic data that made this project possible. My gratitude goes to my husband and sons for their encouragment.

SHEAR-WAVE VELOCITY STRUCTURE IN THE CRUST AND UPPER MANTLE BENEATH THE CENTRAL TIEN SHAN FROM SURFACE-WAVE TOMOGRAPHY

An Abstract of a Dissertation

Presented to

The Faculty of the Department of Earth and Atmospheric Sciences

University of Houston

In Partial Fulfillment

of the Requirements for the Degree

Doctor of Philosophy

By

Arianna Lisi

May 2014

ABSTRACT

The Tien Shan in central Asia is the world's largest and most active intracontinental orogen, with a shortening rate of 20 mm/yr. Its tectonic reactivation started 20-25 Ma, which has been attributed to the India-Eurasia collision. Despite many geological and geophysical studies in the Tien Shan, the mechanism of building this intraplate mountain belt remains debatable. Here I constructed a 3-D shear-wave velocity model beneath the central Tien Shan using Rayleigh-wave data recorded at 41 broadband stations in the study area. Phase velocities are obtained from the two-plane-wave inversion at periods of 20 to 133 s and from the ambient noise tomography at 8 to 30 s and are used to determine shear-wave velocity variations beneath the central Tien Shan.

Low-velocity anomalies in the upper crust correlate well with thick sediments in the Tarim basin, Lake Issky Kul, and Naryn basin. The lowest velocity in the lower crust is beneath the central high range, suggesting a weak crust. A fast velocity anomaly is imaged beneath the northern Tarim block to the Naryn basin from 30 to 70 km, indicating the underthrusting of the Tarim basement. These observations support that the formation of the Tien Shan is due to both a strong Tarim and a weak Tien Shan lithosphere.

A circular slow anomaly to 150 km depth is observed beneath the Naryn basin in the west, while the eastern central Tien Shan is characterized by a fast anomaly. In addition, the fast anomaly that represents the Tarim lithosphere stops sharply at the Naryn basin but continues and deepens under the eastern part. Such variation of velocity structure along the Tien Shan strike implies that the western and eastern range is undergoing different mountain building procedures. A favorable interpretation is that the subducted Tarim

lithosphere was delaminated in the west and the slow anomaly there reflects the hot asthenosphere. In contrast, the Tarim lithosphere is still present beneath the eastern part, which may be removed in the future to develop the scenario as in the western part.

CONTENTS

1 INTRODUCTION

1.1 Tectonic history of the Tien Shan

The Tien Shan in Central Asia is the world's largest and most active intraplate mountain belt, which is located from 1000 to 3000 km north of the India-Asia suture. It extends ~2500 km along WSW-ENE direction from the Aral Sea in Uzbekistan, via northern Tajikistan, Uzbekistan, Kazakhstan and Kyrgyzstan to northern Xinjiang in China and has a maximum width of ~400 km at its western extent (Fig. 1.1). It is one of the largest accretionary orogens in the planet (Cawood *et al.*, 2009) and records the long-lived, north-to-south (present coordinates) Central Asian Orogenic Belt (Windley *et al.*, 2007).

The range resulted as a collage of many continental blocks, several volcanic islands arcs and accretionary prisms (Fig. 1.2), and evolved into a major collisional orogeny at the end of Paleozoic after the closure of a roughly east-west trending ocean basin (Burtman, 1975; Allen *et al.*, 1992) with continuous deformation till Mesozoic time (Hendrix *et al.*, 1992). Tectonic activity resumed about 20-25 Ma (Sobel and Dumitru, 1997; Yang and Liu, 2002) due to the Alpine-Himalayan collision (Tapponier and Molnar, 1979; Avouac *et al.*, 1993) although the details about how these are related are still controversial.

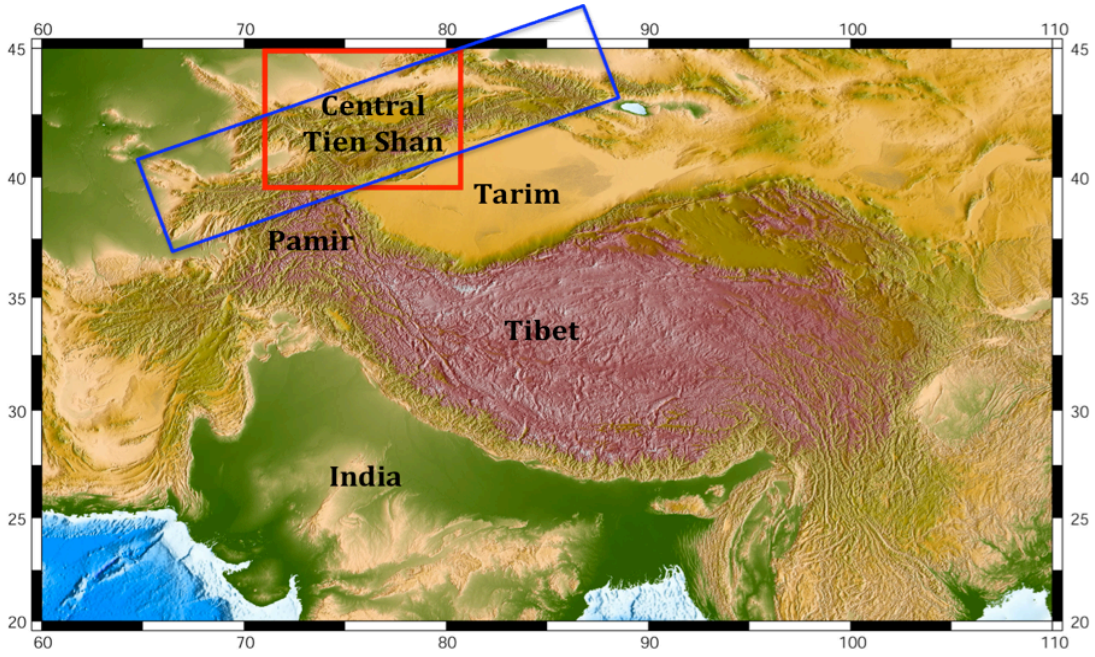

Figure 1.1 - Topographic map of central Asia. The blue box encloses the whole Tien Shan orogenic range, while the red box indicates the area of this study.

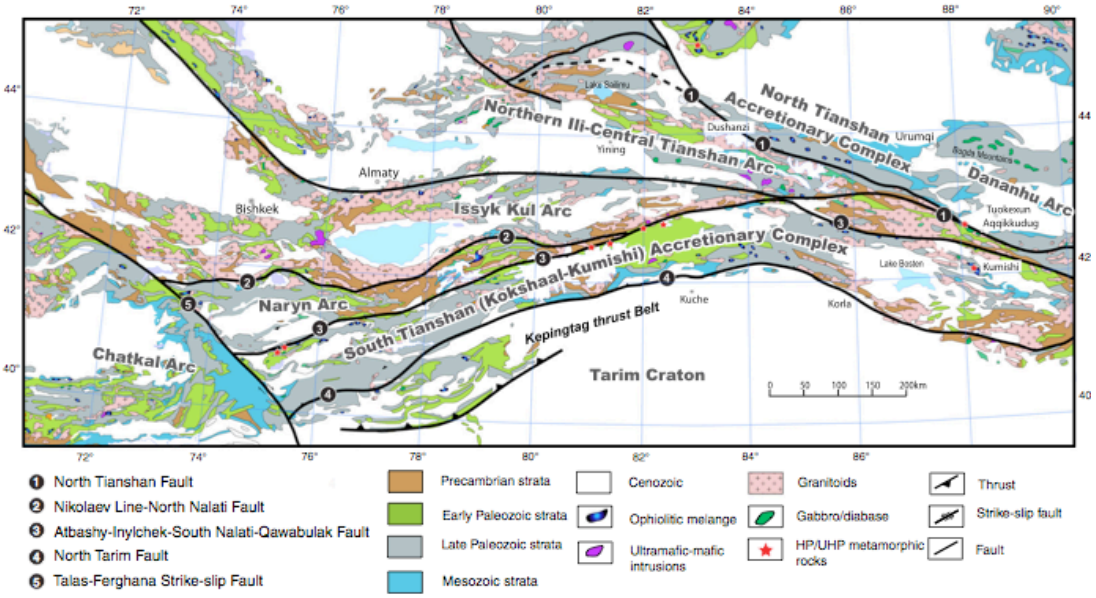

Figure 1.2 – Simplified geological map of the Tian Shan major Early Paleozoic tectonic assemblages and structures (From Xiao *et al.*, 2012).

Since the India-Asia collision started about 55 Ma ago (Searle *et al.*, 1987), the Indian plate has continued to converge with the stable interior of Asia at a rate of roughly 50 mm/yr (Patriat and Achache, 1984). This has required the accommodation of some 2000-2500 km of convergence (Dewey *et al.*, 1989). Only part of this shortening occurred in the Himalayas and Karakoram, adjacent to the actual India-Asia suture (Fig. 1.1). The much greater part has been achieved by a combination of thrusting and strike-slip faulting in central and southeast Asia (Tapponnier *et al.*, 1986; Burchfiel and Royden, 1991). The deformation is mainly in areas with a younger lithosphere assembled during Paleozoic convergent processes between the southern active margin of the Siberia Craton and the northern margins of Tarim and North China Cratons (Molnar and Tapponnier, 1981). The resulting accretionary orogenic systems formed the Central Asian Orogenic Belts, known also as the Altaids; the Tien Shan is a significant part of the belt.

Geochronology investigations in many parts of the Altaids indicated the orogeny was built from multiple subduction events with different polarities and ages (e.g., Charvet *et al.*, 2007, 2011; Kröner *et al.*, 2007; Windley *et al.*, 2007; Wang *et al.*, 2010; Xiao *et al.*, 2004a, 2009, 2010a,b; Heubeck, 2001). Subduction-related accretion in the Paleo-Asian Oceans (Junggar–Balkash and South Tian Shan) gave rise to the present Tian Shan orogenic belt. The northern part mainly developed in the middle Paleozoic by consuming the Junggar–Balkash Ocean and other island arcs. The southern orogenic collage was formed by the closure of the South Tian Shan Ocean, which separated the Central Tian Shan in the east and other Paleozoic volcanic oceanic arcs in the west from the cratons (Tarim and Karakum) to the south. Subduction-related magmatism is known in nearly all the geological zones of the Tian Shan in early-middle Carboniferous and continued in the

island arcs in late Carboniferous and early Permian (Chen; *et al.*, 1999; Xiao *et al.*, 2004b; Ren *et al.*, 2011).

The Tarim craton collided from south to the Tian Shan in the Late Carboniferous-Late Permian (Windley *et al.*, 1990). A western promontory of the craton may have hit the northern Ili–Issyk Kul–Chatkal composite arc, where deep subduction and ultrahigh-pressure metamorphism occurred in the Permian–Triassic (Xiao *et al.*, 2010a, b). Large nappes in ophiolites and passive margin sediments were thrust onto the Tarim Craton during the Early Permian when the Tian Shan orogen become largely subaerial (Carroll *et al.,* 1995, 2001). The Tarim Craton has a variably deformed and metamorphosed basement of Archaean–Proterozoic to early Paleozoic rocks (Huang *et al.*, 2005; Long *et al.*, 2010). Magmatic activities and mafic dykes within the craton have been interpreted as episodes of rifting (Zheng *et al.*, 2010; Shu *et al.*, 2011) from Neoproterozoic till 650–630 Ma. The northern Tarim craton was a stable marine platform with continental rifts developed in Precambrian continental basement (Carroll *et al.*, 1995). The western craton was mainly covered by passive margin sediments during the Paleozoic time (Biske and Seltmann, 2010) and the eastern part may have been an active margin in the Paleozoic (Xiao *et al.*, 2010a,b).

The current Tien Shan is bounded between the Kazakh shield in the north and the Tarim basin in the south, both of which have been stable since Precambrian. High mountain ranges in the northern and southern parts of the central Tien Shan are separated by the intervening Naryn Basin. Deformation in the Tien Shan became intense from Late Miocene-Pliocene-Early Quaternary (Allen *et al.*, 1995; Thompson *et al.*, 2002) and the strike of regional compression changed from NW-SE to N-S during this time period. The

active N-S crustal shortening is distributed throughout the entire mountain belt through roughly east-west trending thrust faults (Ghose *et al.*, 1998) (Fig. 1.3) with the present day shortening rates of 20 mm/y (Figs. 1.4 and 1.5) (Abdrakhmatov *et al.*, 1996; Molnar and Ghose, 2000; Reigber *et al.*, 2001, Gan *et al.*, 2007). Shallow earthquakes, those with focal depths less than 20 km, are distributed throughout the central Tien Shan and adjacent areas, except Lake Issyk Kul, the Naryn basin, and the At-bashy basin, which are believed to be aseismic areas (Fig. 1.6) (Xu *et al.*, 2006).

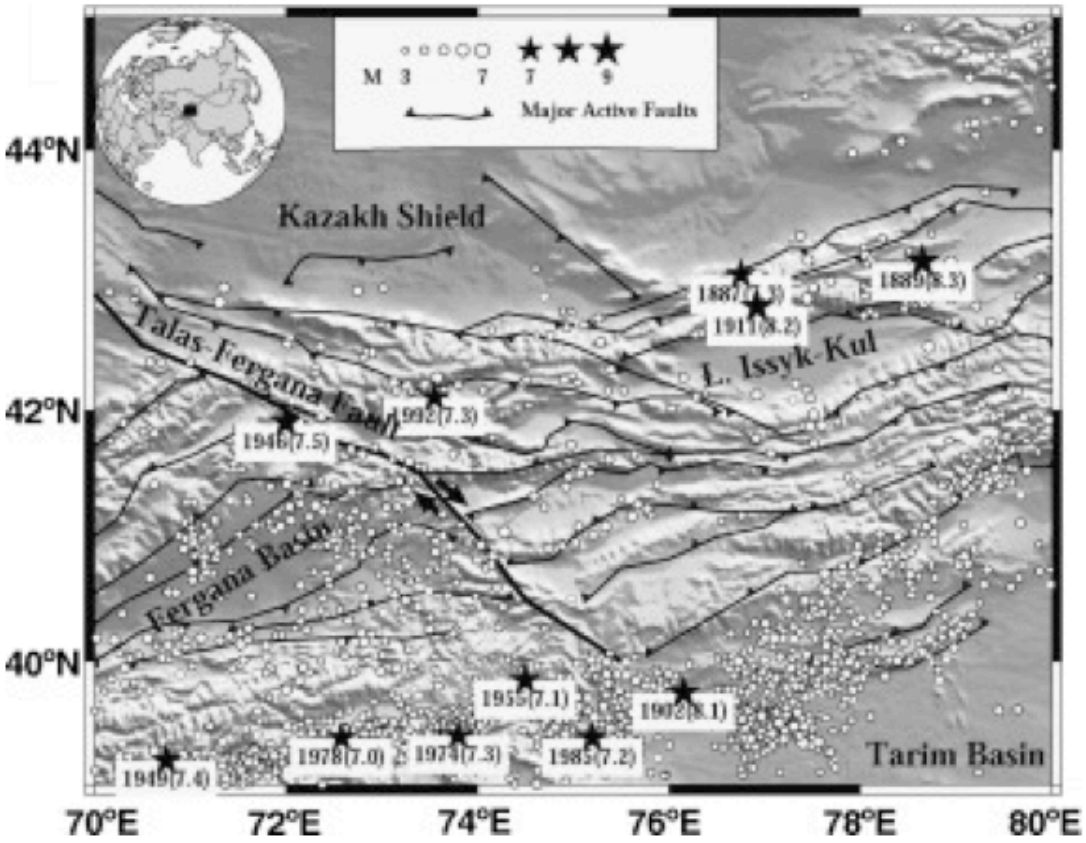

Figure 1.3 - Topographic map of the central Tien Shan showing the major regional tectonic features. Circles denote the hypocenters of earthquakes ($3 < M < 7.0$) reprocessed by Engdahl *et al.* (1998). The stars mark the epicenters of large historic earthquakes ($M \geq 7.0$) since the late nineteenth century, complied from Kondorskaya and Shebalin (1982). The traces of major active faults, scanned from Ghose *et al.* (1998), have been overlaid. Among them, the thicker trace denotes the Talas-Fergana Fault. The inserts show the geographic location and legend of the map (From Lei and Zhao, 2007).

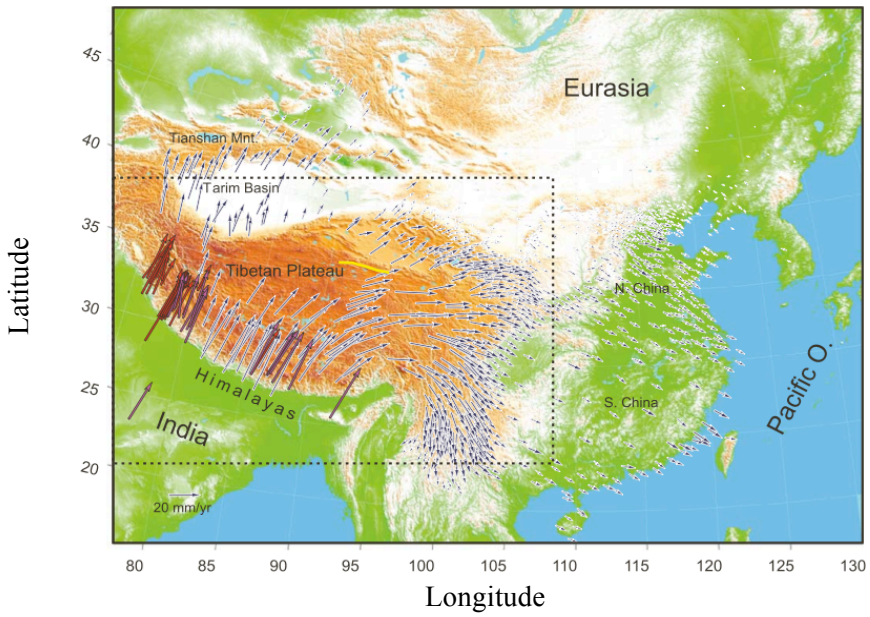

Figure 1.4 - GPS velocity field of crustal motion in central Asia relative to the stable Eurasia. The GPS velocities are from Niu *et al.* [2005] and Wang *et al.* [2001] (blue vectors), Paul *et al.* [2001], and Banerjee and Burgmann [2002] (red vectors) (From Gan *et al.*, 2007).

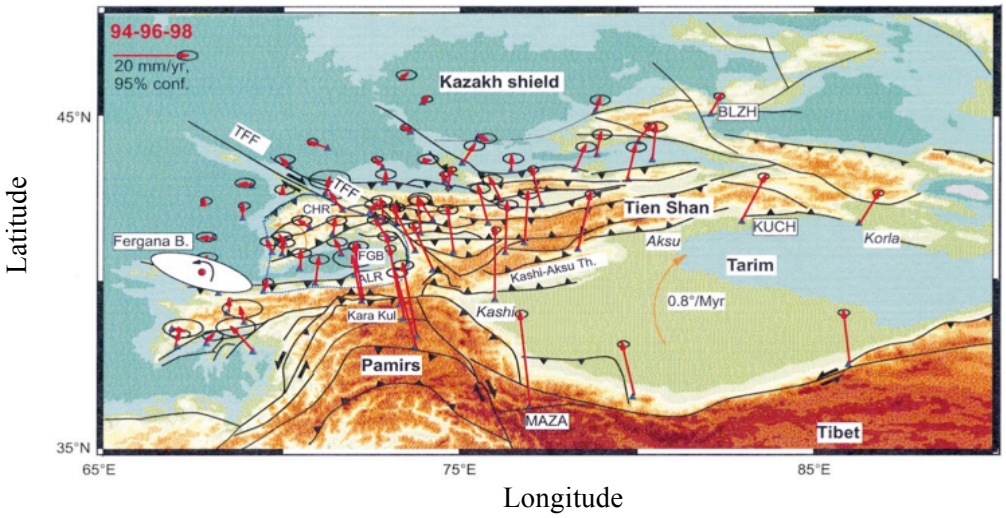

Figure 1.5 - GPS vectors with respect to `stable' Eurasia. The motion of `stable' Eurasia is defined using 34 IGS (Table 1) stations (ITRF97, http://lareg.ensg.ign.fr/ITRF/ITRF97.html). Fergana B.: Rotation pole of FGB, TFF: Talas Fergana Fault, CHR: Chatkal range, ALR: Alai range. (From Reigber, *et al.*, 2001)

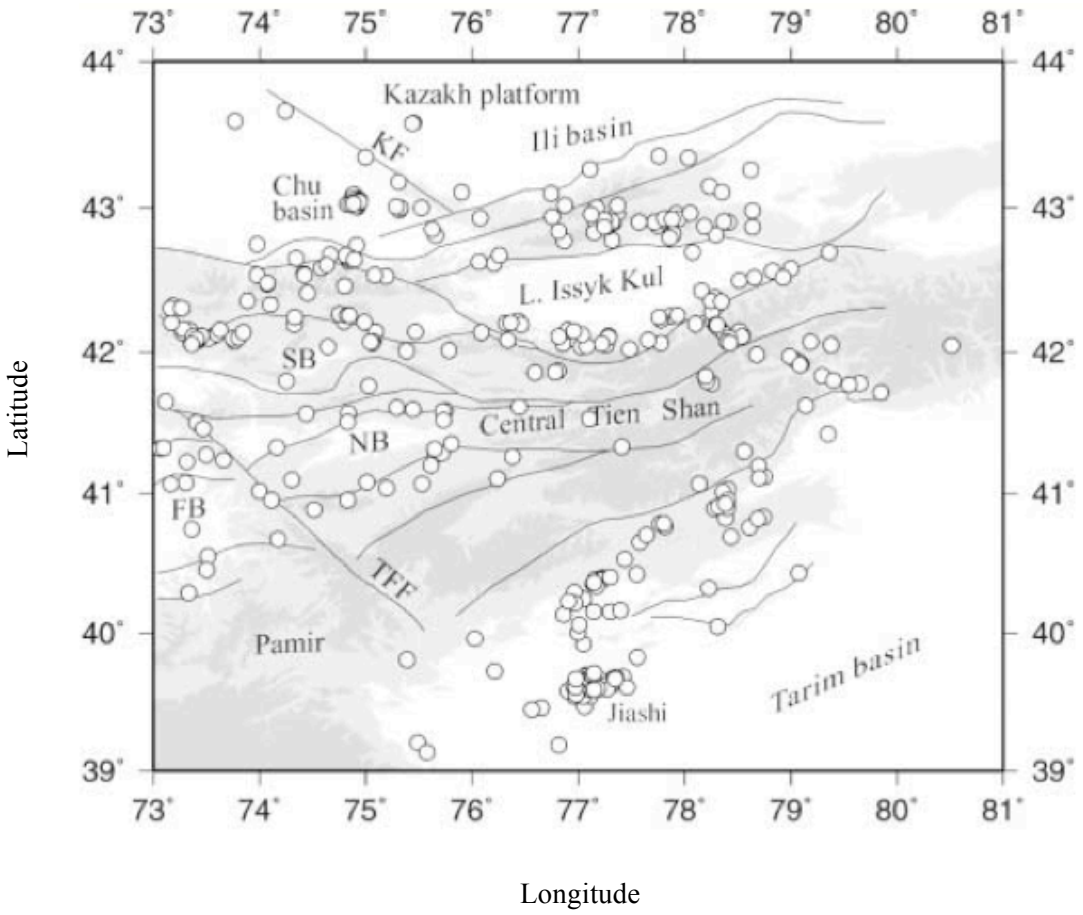

Figure 1.6 – Epicenter distribution of the relocated earthquakes with focal depths less that 20 km. Thin lines are simplified traces of major active faults. TFF, Talas-Fergana Fault, FB, Fergana Basin, NB, Naryn Basin (From Xu *et al.*, 2006).

The central and western parts of the Tien Shan are separated by an obliquely oriented right-lateral strike slip fault, the Talas-Fergana fault (TFF), which extends over a distance of some 500 km from the Tarim Basin in the south to the Kazakh Shield in the north (Figs. 1.3 and 1.6), defining a fundamental lithospheric boundary within the Tien Shan and separating two areas with different Cenozoic tectonic histories and different geological and geophysical properties. Furthermore, the TFF separates two opposite subduction vergences: on the west side the Tien Shan subducts at a high angle beneath the Pamirs, while on the east the Tarim basin underthrusts beneath the Tien Shan. The Talas-Fergana fault has been intermittently active since the Permian with a total right-lateral shear of 180-250 km. A stratigraphic correlation of Early Cretaceous sedimentary rocks on both sides of the fault indicates an offset of 60±10 km with motion commencing ca. 10 Ma. It is not clear if the Talas-Fergana fault reflects a contrast in the dynamics of mountain building between the east and west side, or has a active role in constraining the kinematics of neotectonic structures at the boundary of the Tien Shan with the Pamirs and Tarim, or acts as a transfer zone between zones of lithospheric-scale underthrusting or as a preferential channel for asthenosphere uprising (Lei, 2011).

1.2 Previous studies

The central Tien Shan is characterized differently from the western and eastern Tien Shan in terms of body wave velocities and lithospheric structure (Kosarev *et al.*, 1993; Roecker *et al.*, 1993 and 2000; Vinnik *et al.*, 2004), deformation style (Hendrix *et al.*, 1992; Bazhenov, 1993; Thomas *et al.*, 1994; Burtman *et al.*, 1996), and isostatic compensation model (Burov *et al.*, 1990; Burov and Molnar, 1998). The crust and mantle in the central Tien Shan have been relatively well studied. Crustal thickness varies from 50 to 75 km across the Tien Shan range according to studies of seismic tomography (Ghose *et al.*, 1998; Roecker, 2001), receiver functions (Fig. 1.7a) (Vinnik *et al.*, 2006), gravity data (Steffen *et al.*, 2011), reflection profiles (Makarov *et al.*, 2010), and petrology evaluations (Bagdassarov *et al.*, 2011).

The seismic profiling of the crust in the junction zone of the Tarim Plate and the Central Tien Shan evidenced a low angle underthrusting of the Tarim Platform beneath the Tien Shan for a distance of 50–100 km. These dislocations extend to at least the Naryn Basin and involve almost the entire crust and the uppermost lithospheric mantle (Makarov *et al.* 2010). Vinnik *et al.* (2004) analyzed P and S receiver functions in the central Tien Shan and found a relatively thin crust and a thin lid underlain by a low velocity anomaly beneath the high elevation in the center of the range, evidence for magma underplating. A low-velocity layer in the upper crust of the central Tien Shan was also proposed by Vinnik at al. (2002), while the study of Kosarev *et al.* (1993) suggested a low-velocity layer in the lower crust.

A magnetotelluric profile across the Kyrgyz Tien Shan (Fig. 1.7b) shows high resistivity beneath the shallow Moho of the Naryn basin, reflecting relict compositional heterogeneity (Bielinski *et al.*, 2003). The conductive zones bounding this block could then be the remnants of Paleozoic sutures. This high-resistivity block is probably mechanically strong, which protects the overlying crust from deformation but can transfer crustal stress to relatively weaker continental crust in the northern and southern parts of the range (Roecker, 2000). On the other hand, Xu *et al.* (2007) reported low velocity anomaly in the shallow upper mantle beneath the southern central Tien Shan from Pn tomography and associated it with a high temperature anomaly produced by mantle upwelling. Roecker (1993) performed body-wave tomography in the central Tien Shan and imaged a low velocity zone between 150 and 300 km depth, which he interpreted as a combination of thermal anomaly and partial melting. An S receiver function study by Oreshin *et al.*, (2002) also imaged a low-velocity mantle layer underlain a strong lid at a depth of 80 - 100 km. In addition, using xenoliths in basalts in the southern Tien Shan, Bagdassarov *et al.* (2011) calculated that the lithosphere strength beneath the Tien Shan was more than 1000 times weaker than that of the Tarim Basin at the beginning of the continental compression in the region. Further deep in the upper mantle, the underthrusting of the Kazak shield and the Tarim block beneath the Tien Shan range is reported in several seismic tomography and receiver function studies (Roecker *et al.*, 1993; Zhao *et al.*, 2003; and Lei and Zhao, 2007; Kumar *et al.*, 2005). In figure 1.8 the results from a receiver function studies (Kumar et al. 2005) is shown with a tomographic image (Friederich, 2003) along a NS section in central Asia passing through the western Tien Shan.

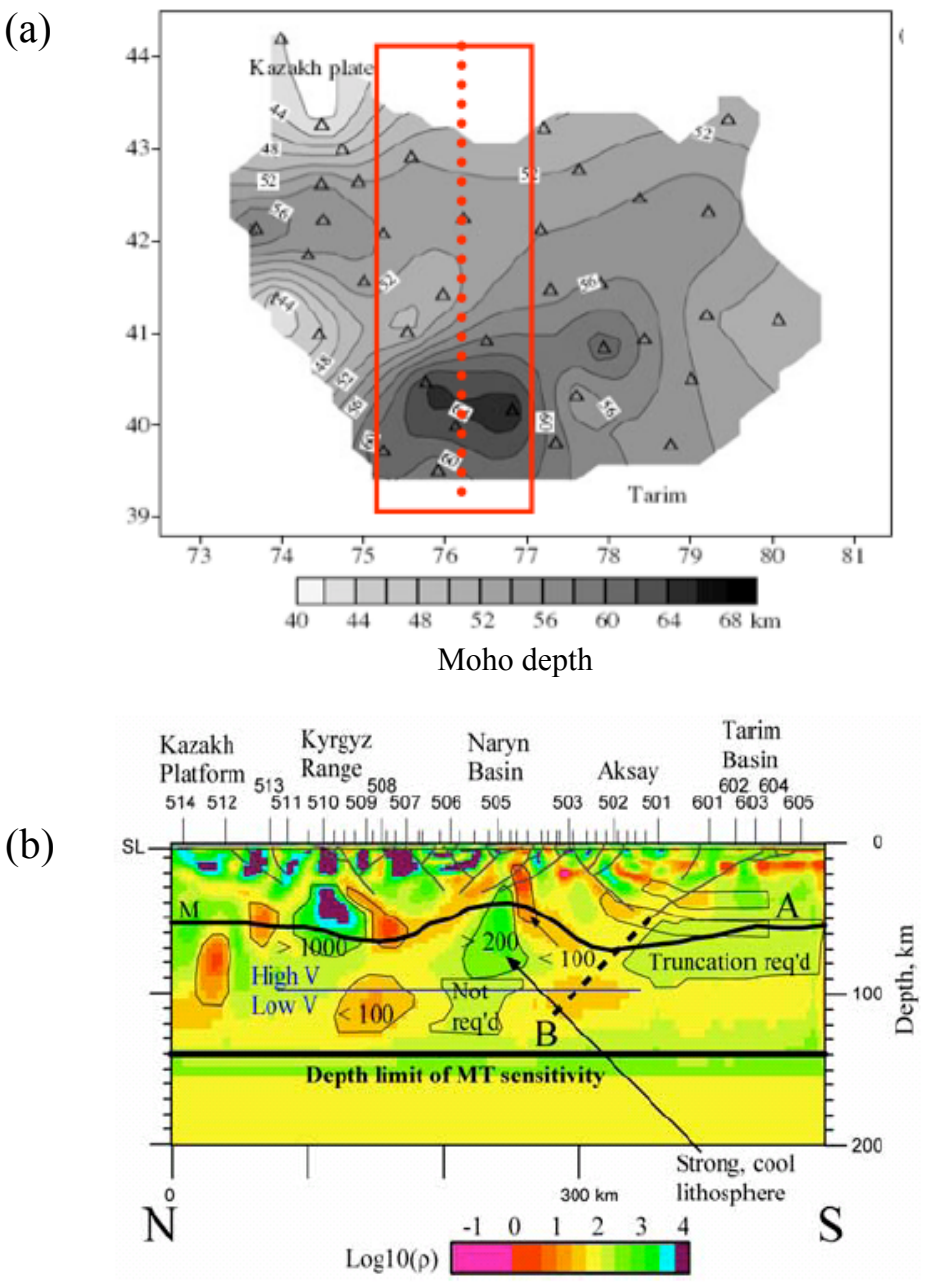

Figure 1.7 – (a) Map of crustal thickness from Vinnik et al, 2006. The red box indicates the location of MT profile across the Krygyz Tien Shan; (b) resistivity model along MT profile. Moho is from *Roecker* (2000). Velocity contrast at about 100 km does not extend north or south of the Tien Shan (*Oreshin et al.*, 2002). From *Bielinski et al.*, (2003).

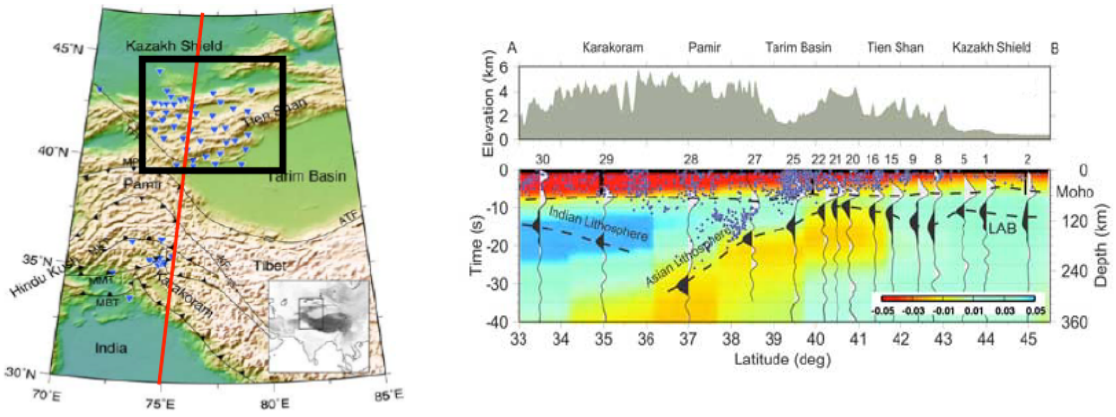

Figure 1.8 - On the left is indicated with the black box the study area and with the red line the location of the seismic section shown on the left with a tomographic image [Friederich, 2003] of the region. Blue dots are the earthquake hypocenters [Engdahl *et al.,* 1998] along a 100 km wide zone along the line. The top panel indicates the topography along the profile. (From Kumar *et al.*, 2005)

Seismic anisotropy in the central Tien Shan is mainly from shear wave splitting analyses (Makeyeva *et al.*, 1992; Wolfe and Vernon, 1998; Li and Chen, 2006). These studies agree on a dominant range-parallel fast direction. Variations from the main fast direction were explained by a model of a small plume beneath the northern central Tien Shan (Makeyeva *et al.* 1992; Wolfe and Vernon, 1998). However, Li and Chen (2006) found the NNE-SSW fast direction, which is coincident with the GPS result (Abdrakhmatov *et al.*, 1996; Reigber *et al.*, 2001), in several less-deformed areas and interpreted the fast direction as the shear between the northward moving lithosphere and the underlying asthenosphere. Anisotropy variation with depth has been studied by Vinnik *et al.* (2002). They conclude that anisotropy above 100 km is from previous

tectonic episodes and the mantle below 100 km is coherent with the superficial deformation.

Several hypotheses have been proposed to explain the tectonic reactivation in the Tien Shan. One explanation is that the Tarim lithosphere, showing very little internal deformation, is strong and able to transfer stress from the Tibet plateau to its northern edge (Molnar and Tapponier, 1975; England and Houseman, 1985). The second hypothesis is that mantle weakness in the Tien Shan existed before the India-Asia collision and made the Tien Shan lithosphere easy to deform (Roecker *et al.*, 1993). Neil and Houseman (1997) performed numerical modeling to study the development of the Tien Shan and concluded that a strong Tarim, a weak Tien Shan, or both can produce significant crust thickening in the Tien Shan.

Many geophysics and geodynamics studies have suggested different scenarios about the dynamic process of the Tien Shan. A lithospheric root formation is expected for a range like Tien Shan because the shortening in the crust should be accompanied by a similar style of shortening in the lithosphere as predicted from the strike-normal model (Fleitout and Froidevaux, 1982; England and Houseman, 1986). Such a root can detach due to gravitational instability and leave a space in the mantle, which is then filled by underlying asthenosphere (England and Houseman, 1989). Chen *et al.* (1997) observed an elevated 410 km discontinuity beneath the Tien Shan and interpreted it as cold temperature associated with the detached root. The lithosphere thickening and the consequent root delamination can also trigger small-scale convection along the mountain strike as suggested by several authors (Burov *et al.*, 1990; Makeyeva *et al.*, 1992; Burov

and Molnar, 1998). Asthenosphere upwelling is proposed by Vinnik *et al.* (2004) to explain the lithospheric thinning beneath the mountain belt.

The suggested hypotheses and dynamic scenarios beneath the Tien Shan can be tested using high-resolution seismic velocity models. In this dissertation research, I constructed a 3-D model of the shear wave velocity structure beneath the central Tien Shan and constrained the variations of seismic anisotropy with depth, using Rayleigh wave fundamental mode data recorded at the Tien Shan seismic network. First, I mapped Rayleigh wave phase velocities and azimuthal anisotropy beneath the central Tien Shan in a period range of 20-133 s applying a two-plane-wave inversion technique (Chapter 2). Rayleigh wave at shorter periods of 10-30 s have been determined by stacking ambient seismic noise at pairs of seismic stations of the Tien Shan network (Chapter 3). The longer the period, the deeper a Rayleigh wave penetrates into the earth. Therefore, given the period range of 10 to 133 s, it is possible to constrain shear wave velocity to the depth of the mid-upper mantle. Then, Rayleigh wave dispersions, obtained from both the techniques, have been combined to construct a 3-D shear-wave model beneath the central Tien Shan (Chapter 4). Strong lateral heterogeneity is observed in phase velocity maps, which reflect crustal thickness variation, sediments thickness variations, as well as shear wave velocity change in the crust and upper mantle. In chapter 5, I will discuss the main features in the model and their implications for the active dynamic process in the central Tien Shan.

2 PHASE VELOCITY MAPS FROM TELESEISMIC EVENTS

2.1 Seismic Networks in the Tien Shan

The seismic data I used in this study were recorded at 41 broadband seismic stations in the central Tien Shan, an area that is confined within latitudes 39°- 45° and longitudes 73°- 81° (Fig. 2.1). Most of these stations forming the Tien Shan network are from two regional networks: 11 from the permanent digital Kyrgyz Seismic Telemetry Network (KNET) and 28 from the GHENGIS temporary seismic array (Roecker, 2001). Data recorded at one GSN/IRIS station (TLG) and one GEOSCOPE station (WUS) are also used. The KNET is a digital telemetry network and utilizes Streckeisen STS-2 very broadband sensor (0.008 – 50 Hz.) and 24-bit digitizers (http://eqinfo.ucsd.edu/deployments/knet.php). Originally the continuous data were recorded at 20 sample per seconds (sps) and the sample rate was upgraded to 40 sps in 1994. The temporary stations were deployed from October 1997 to August 1998 and were operational until August 2000. Each station was equipped with a three-component broadband sensor, CMG-3ESP or STS-2 (Roecker, 2001).

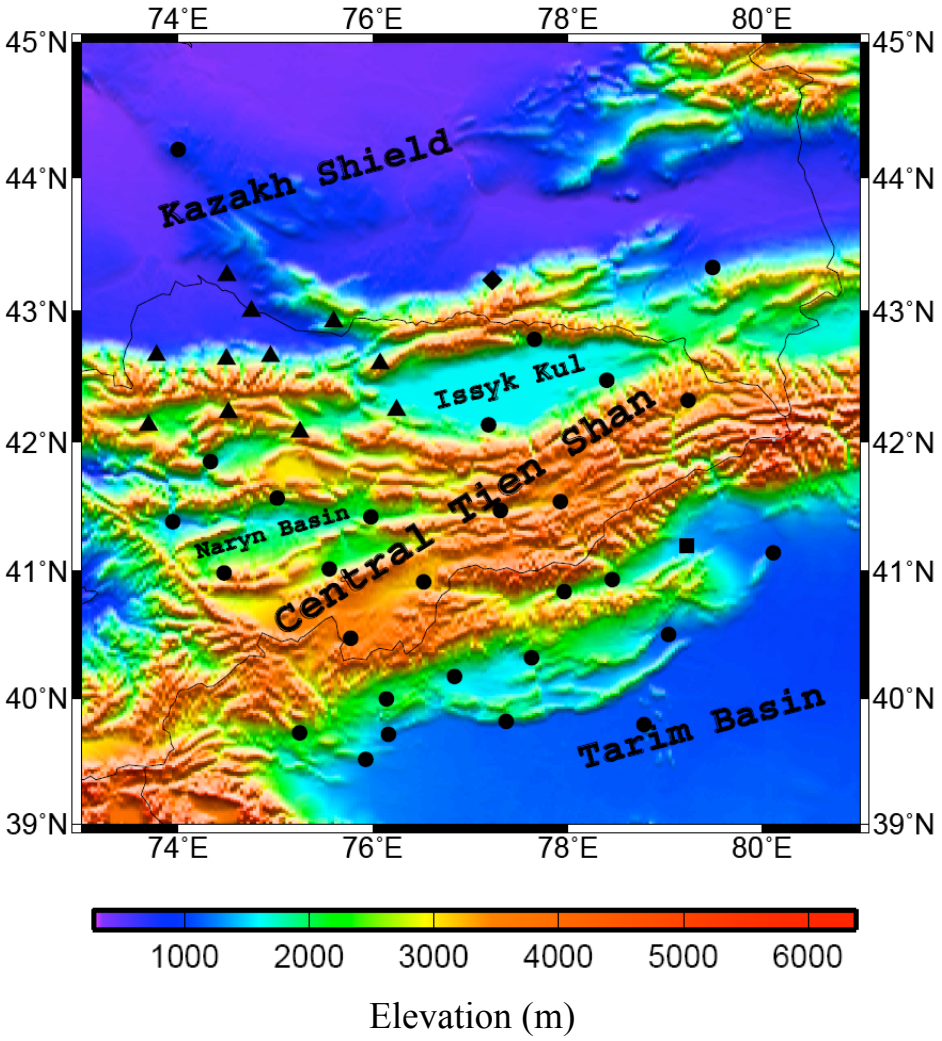

Figure 2.1 - Topographic map of the central Tien Shan. The black symbols indicate seismic stations from several networks. Triangles and circles indicate the KNET and GHENGIS networks, respectively. The square shows the GEOSCOPE station (WUS); and the diamond shows the KAZNET station (TLG).

2.2 Rayleigh waves

The Rayleigh waves are formed by the interference of P waves with the SV waves on the free surface or any interface in the inner of the earth (Lay and Wallace, 1995). Compared with body waves they are characterized by low frequency, low velocity and large amplitude (Fig. 2.2).

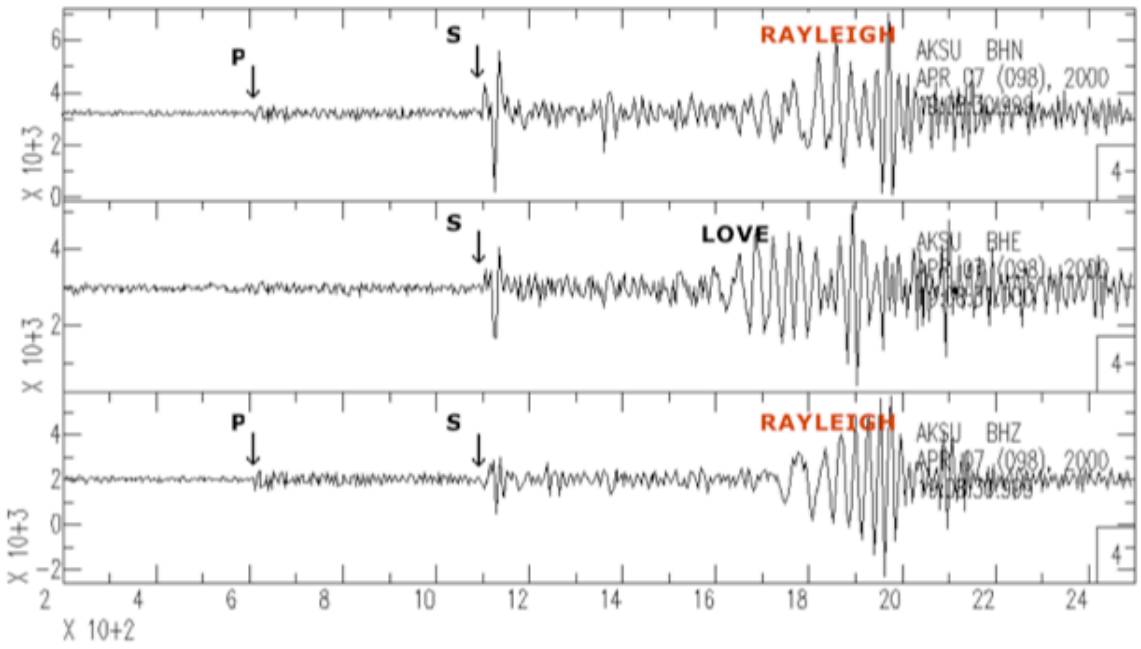

Figure 2.2 - 3 components seismograms, recording a teleseismic event at AKSU station, showing P waves, S waves and surface-waves, Rayleigh and Love. From the top to the bottom N-S radial, E-W transverse, and vertical component are shown. The Rayleigh waves are visible only in the radial and vertical because associated with SV and P waves, while the Love waves, associated with SH, are emergent on the transverse component .

Rayleigh waves propagate along the surface following the great-circle path from a source to a receiver for the 1D earth and their amplitude decays with depth (Fig. 2.3).

An important feature of Rayleigh wave is dispersion, a phenomenon that a wave velocity depends on its frequency. Rayleigh waves with longer period travel deeper and at higher velocities, while higher frequency waves travel at shallower depth and are slower (Fig. 2.4). Dispersion of Rayleigh waves reflects the nature of the velocity gradient at depth. In general a good approximation is that the fundamental mode Rayleigh waves have the peak sensitivity at the depths of one third of their wavelengths. The fact that the Rayleigh wave velocities depend on the depth range sampled by each period makes surface-wave dispersion valuable for studying earth structure and for constraining the distribution of anisotropy with depth.

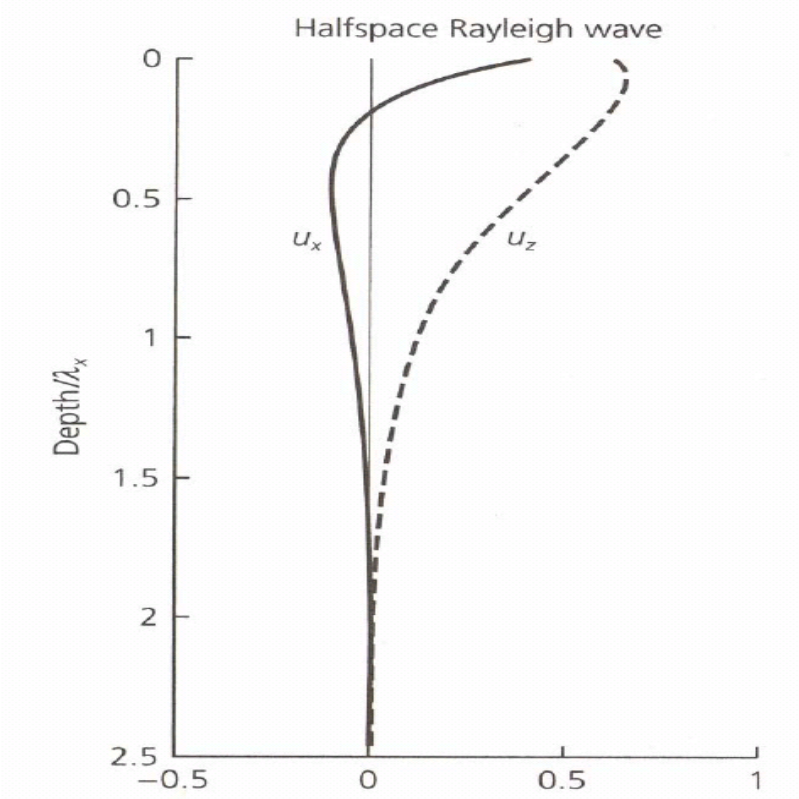

Figure 2.3 – Rayleigh wave displacement variations with depth in a halfspace composed of a Poisson solid. Ux and Uz are radial and vertical components, respectively. The displacement on both component decays with depth. The depth in this plot is normalized by the wavelength (λx). (from Lay and Wallace, 1995).

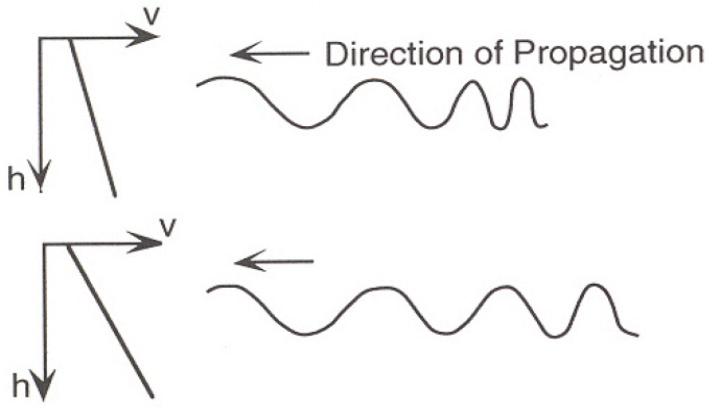

Figure 2.4 - Influence of vertical velocity gradient on the dispersion of Rayleigh waves. Stronger velocity gradients produce more pronounced dispersion (from Lay and Wallace, 1995).

2.3 Data and data processing

Seismic data used in this study are fundamental-mode Rayleigh waves from teleseismic events recorded at 41 stations in the central Tien Shan. I considered earthquakes occurring between September 1st, 1998 and August 31st, 2000, when all the 41 stations were operating .

In order to have good Rayleigh wave signal, I avoid using events too far where signals tend to be weak or complicated due to attenuation and along-path effects or too close where Rayleigh waves are not well separated from shear wave arrivals. The selected events occurred in a distant range between 20° and 110° from the center of the network with magnitude larger than 6. Among the 105 events with these characteristics, I choose 43 earthquakes showing high signal-to-noise ratio (38 with 6<M<7 and 5 with M>7). In order to have a better azimuthal coverage, 10 events were added to the original data set: 4

of the 10 events are in the same distance range with 5.5<M<6, and the other 6 events are at distance between 110° and 123° with M>6 (Fig. 2.5).

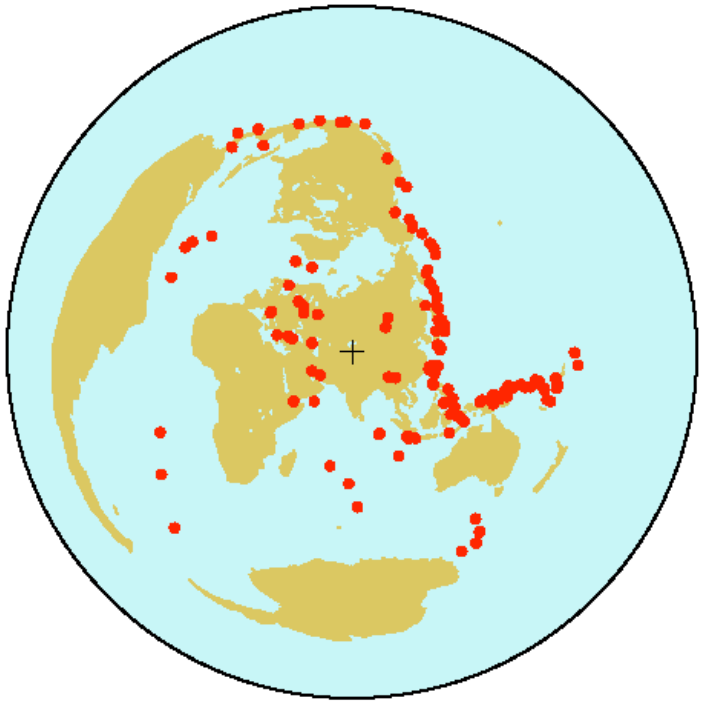

Figure 2.5 – Distribution of the teleseismic events used in the inversion of Rayleigh wave fundamental mode. The center of the Tien Shan network is indicated by the black cross.

All the seismic records for the analyzed earthquakes are obtained from the IRIS data management center (http://www.iris.edu). Crossing ray paths of the selected events are dense within the Tien Shan network (Fig. 2.6). The number of ray paths varies with frequency with the largest number at intermediate periods. The reduction of ray path coverage at short and long periods is due to multipathing and the decrease of signal-to-noise ratio, respectively.

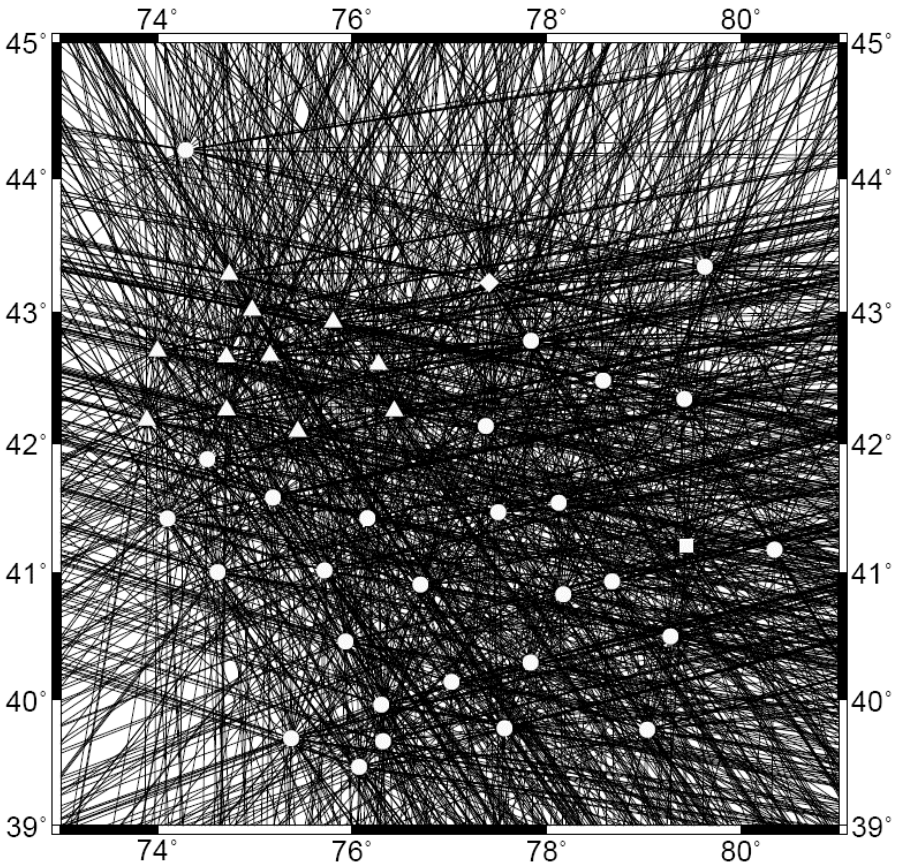

Figure 2.6 - Ray path coverage in the study area at period of 50 s. White symbols indicate seismic stations as shown in figure 2.1.

The goal of the data processing was to extract fundamental mode Rayleigh waves at different frequencies. Only vertical component seismogram was used in the analysis because generally they are less noisy than horizontal ones and also the vertical component of Rayleigh wave motion is stronger. To analyze the Rayleigh waves dispersion a bandpass filter was applied to separate different waveform at different frequencies. I used the Butterworth filter that has the most flat response without any ripples in the pass-band

and stop-band that other filters tend to have, which does not cause amplitude distortion. The cut off at the corner frequency for the Butterworth filter depends on the number of order, n. The higher the order is, the sharper the cutoff (Fig. 2.7).

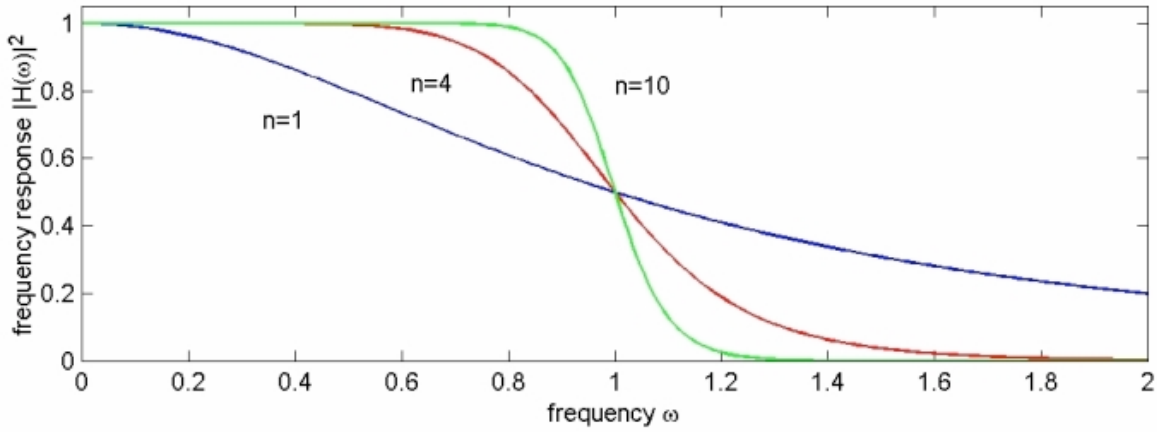

Figure 2.7 - Three different orders of lowpass Butterworth analog filters: n={1,4,10}. As n increases, the filter more closely approximates an ideal brickwall lowpass response.

The Butterworth filter has non-linear phase response that can result in some dispersion of filtered waveforms (Figs. 2.8 a–b). Because in the Rayleigh wave tomography it is important to not modify the amplitude as the phase of data, a zero-phase implementation of the filter has to be provided by running the filter forward and backward over the data (2 pass filter), instead of just forward over the data (1 pass filter). Figure 2.8 illustrates that applying the filter just one time causes a delay of 5 seconds in the P wave arrival time. If the same filter is applied twice, forward and backward over the data, the arrival

time on the filtered signal is coincident with that on the raw signal. This phase distortion and correction caused by applying 1 pass and 2 pass of the Butterworth filter is same for any time series including Rayleigh waves. A comparison between the 1 pass and 2 pass filtered Rayleigh waves data is shown in figure 2.9. The phase delay caused by applying a non-linear filter increases for lower frequencies. For the frequencies range typical of Rayleigh wave the phase delay is much higher than that for P wave that is characterized by higher frequency. *Saltzer* (2002) analyzed two tomographic studies that used the same array and a similar technique but have very different results and found out that the main difference between the two procedures was that phase shift delay due to the filtering was corrected in one study but not in the other one. It is therefore important in applying the Butterworth filter with double-pass to ensure no artificial phase delays in the filtered seismograms.

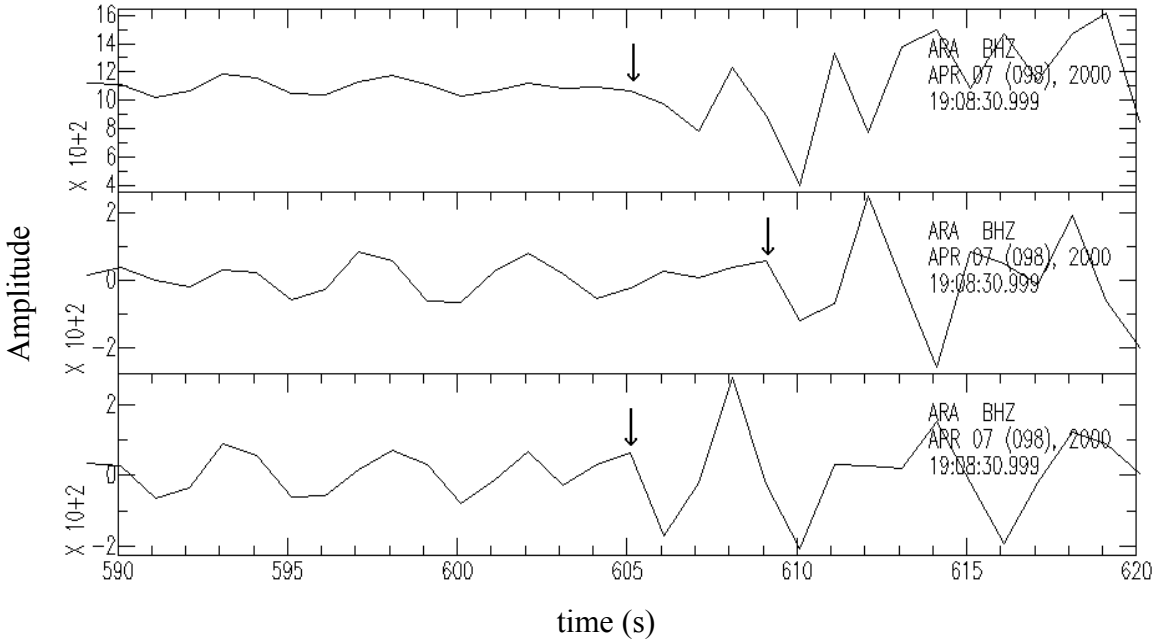

Figure 2.8 - Comparison of the original seismogram (a) with a 4th order Butterworth, 200 mHz wide band-pass, with center frequency 250 mHz. (b) one pass filter; (c) two passes filter. It is evident the phase shift in the arrival time of P wave when a 1 pass filter is applied.

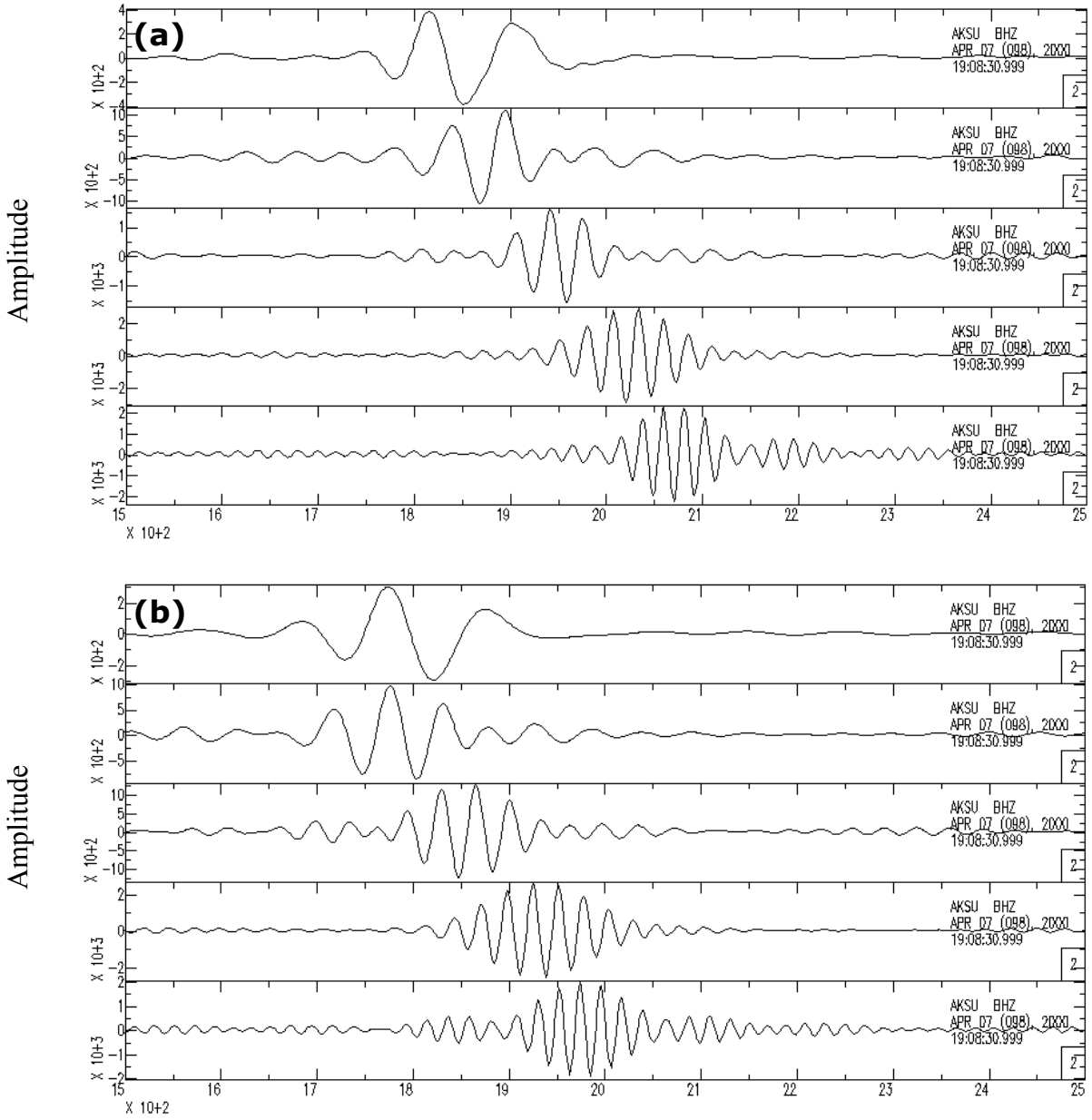

Figure 2.9 - Vertical component seismograms filtered with a 4th order Butterworth, 10 mHz wide band-pass, with center frequencies ranging from 7 to 47 mHz. (a) 1 pass filter; (b) 2 pass filter.

With a better understanding of the effects caused by filters, I choose to apply a 4^{th} order, double-pass Butterworth band-pass filter to each seismic trace after removing instrument response from the seismograms. The filter was centered at the frequency of interest with a 10 mHz frequency interval. At a given frequency, only those Rayleigh waves with good signal-to-noise ratio were retained and isolated from other phases by applying an appropriate time window, a boxcar window with a 50 s cosine taper at each end. The width of the window varies with frequency and epicentral distance. The quality of the filtered seismograms was manually checked, and noisy traces and incoherent signals at nearby stations were removed .

From the 53 selected seismograms showing high signal-to-noise ratio, Rayleigh wave fundamental mode was extracted at 17 frequency intervals with the central frequency ranging from 7.5 mHz to 50 mHz, which corresponds to a period range of 20 s - 133 s. An example of processed Rayleigh wave waveforms is presented in figure 2.10, where the fundamental-mode Rayleigh wave at AKSU station is shown for the broad frequency range. I computed Rayleigh wave phases and amplitudes from each extracted seismogram by applying a positive Fourier transform. These phase and amplitude data are then inverted for the incoming wavefield and Rayleigh wave phase velocities.

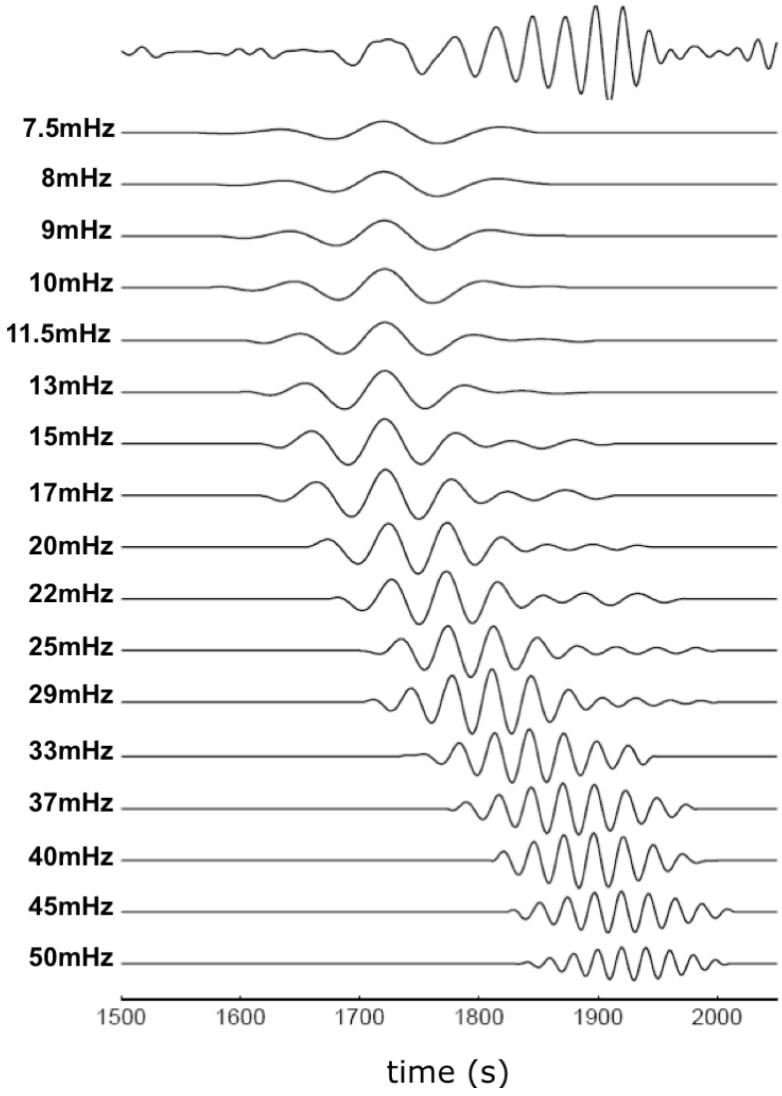

Figure 2.10 - Example of a windowed fundamental-mode Rayleigh wave trains in the frequency range of 7.5-50 mHz at station AKSU from an M=6 earthquake occurred in the Indian Ocean. The top trace is for Rayleigh wave with a broad-band filter. A 4th order, double-pass Butterworth band-pass filter with a width of 10 mHz has been applied for each frequency interval to all the seismic traces. Rayleigh wave phase and amplitude has been measaured by applying a positive Fourier transform to the filtered and windowed seismograms. Only for graphical purposes the traces have been scaled by different factors: 2 for the broad-band, 5 for 7.5-10 mHz, 4 for 11-22 mHz, 3.5 for 25-29 mHz, 2 for 33 mHz, and 1.5 for 37-50 mHz.

2.4 Two plane wave inversion method

I adopted the two-plane-wave inversion technique in solving for phase velocity variations and azimuthal anisotropy from Rayleigh wave phase and amplitude data (Li *et al.*, 2003; Li *et al.*, 2005; Forsyth and Li, 2005; Li, 2011). This inverse method has a great advantage to take account of the non-planar energy in the incoming wavefield that is caused by scattering or multipathing along a ray path, due to heterogeneity between a source and a receiver. It works well for seismic array analyses so that the structure beneath the array can be more accurately resolved.

In the inversion, the incoming wavefield of each event is represented by the interference between two plane waves with initially unknown amplitudes, phases, and propagation directions. The solution is reached through two sets of iterations, with two stages of inversion for each iteration, to minimize misfit to the phase and amplitude. To begin the inversion, the station with the largest amplitude is chosen as the reference station, because the two plane waves are most likely to be in phase at that station and the amplitude should be representative of the sum of the amplitude of the two waves. Observed amplitudes at the other stations are normalized by the reference station amplitude and phase.

In the first stage of each iteration, the six parameters of the two plane waves for each event are solved using a downhill simplex method of simulated annealing (p.444, Press *et al.*, 1992) while holding velocity fixed (starting values or current values found in the previous iteration). The inversion for plane wave parameters is done for each event independently. To find the global minimum the simulated annealing starts at each

iteration with several different wave-parameter models including the best model from the previous iteration.

In the second stage of each iteration, a generalized linear inversion technique (Tarantola and Valette, 1982) is applied to simultaneously solve for changes to the current phase velocity model and plane wave parameters for each event. The solution to the general non-linear inverse problem is:

$$\Delta\mathbf{m} = (\mathbf{G}^T\mathbf{C}^{-1}_{nn}\mathbf{G} + \mathbf{C}^{-1}_{mm})^{-1} (\mathbf{G}^T\mathbf{C}^{-1}_{nn}\Delta\mathbf{d} - \mathbf{C}^{-1}_{nm} [\mathbf{m}-\mathbf{m}_0]) \quad (1)$$

where $\mathbf{m}$ is the current model, $\mathbf{m}_0$ is the original starting model, $\Delta\mathbf{m}$ is the change to the model, $\Delta\mathbf{d}$ is the difference between the observed and predicted data for the current model, $\mathbf{G}$ is the partial derivative relating $\Delta\mathbf{d}$ to $\Delta\mathbf{m}$, $\mathbf{C}_{nn}$ is *a priori* data covariance matrix, $\mathbf{C}_{mm}$ is *a priori* model covariance matrix. The observed data are the real and imaginary components (or amplitude and phase) at the studied frequency for each filtered and windowed seismogram. The predicted data are functions of the wave parameters and velocity parameters at the grid points. The velocity and wave parameters together form **m.** This is a mixed determined problem (Menke, 1984): it is overdetermined because there are more observations than model parameters, but it is underdetermined because not all the model parameters are well resolved.

I parameterized phase velocity by a grid that has relative dense nodes in the station-covered region with 0.5° spacing in both longitude and latitude (Fig. 2.11). Node spacing of 1.0° is used at the edge of the grid considering that ray path coverage is less dense there. I choose the grid region larger than the station-covered region because the outer

region is also covered by crossing ray paths. More importantly these nodes can absorb some phase effects due to more complex wavefield that cannot be completely represented by the two-plane wave approximation, which is common at short periods.

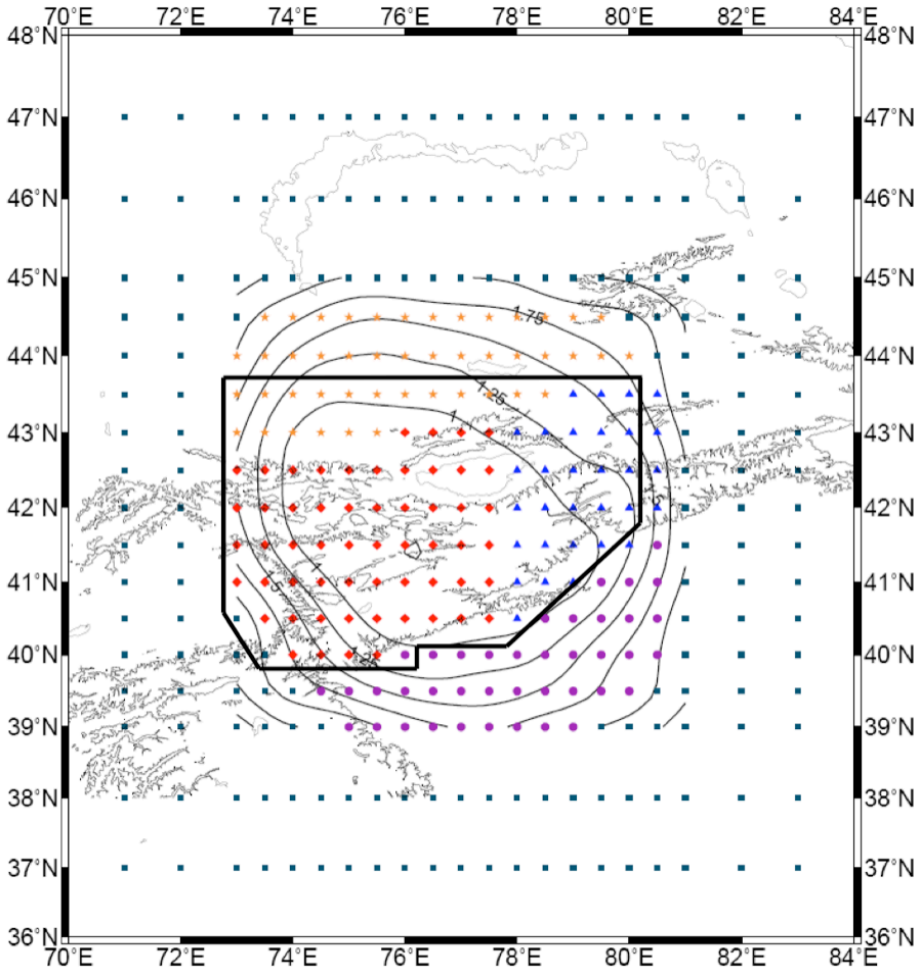

Figure 2.11 - Grid nodes used in Rayleigh wave phase velocity inversions. Different colours indicate the four sub-regions where dispersion curves are calculated and shown in figure 2.14. Orange stars are for the Kazakh shield, red diamonds for the Tien Shan range west of 78° meridian, blue triangles for Tien Shan range east of the 78° meridian, and purple dots for northern Tarim basin. The contours are from the resolution map of twice the standard errors of phase velocities at 50 s in figure 2.15 The black box defines the region where the average azimuthal anisotropy is calculated and displayed in figure 2.17.

After the initial inversions, the data are checked for any event with large residuals. In this way it is possible to correct errors or eliminate records with low signal-to-noise ratio that were not previously removed. If there is not a clear reason for the large residuals, the data are kept and analyzed.

To represent the finite width of the response of surface-waves to structure along the raypath, I adopted, in the 1-D inversion, a Gaussian sensitivity function for each plane wave (Forsyth and Li, 2005), while in the 2-D phase velocity inversion I used the 2-D Born sensitivity kernels (Yang and Forsyth, 2006). The authors modified the 2-D sensitivity kernels from Zhou et al. (2004) for an incident plane wave on the Earth's surface, and applied them in the TPW method for regional Rayleigh-wave tomography to better account for finite-frequency effects.

The 2-D sensitivity kernels expressing the sensitivities to the local phase velocity perturbation, δc/c, are defined as

$$\delta d = \iint_{\Omega} K^{c}_{d}(r,\omega)(\delta c/c)d\Omega \qquad (2)$$

where the integration is over the earth surface (Zhou *et al.* 2004). δd can be the phase delay,δϕ, or the relative amplitude variation, δlnA, with corresponding phase kernel $K^{c}_{\phi}(r,\omega)$ or amplitude kernel $K^{c}_{A}(r,\omega)$. This method, using the sensitivity kernels for both amplitude and phase, increases resolution compared with the method using Gaussian functions that considers phase sensitivity only. Therefore it can better account for finite-frequency effects and resolve small-scale structure. The rayleigh sensitivity kernels are

shown in figure 2.12 where the partial derivative of phase velocities with respect to shear wave velocities is plotted for three periods.

For each of the two plane waves, the 2-D sensitivity kernels at each period depend on the reference phase velocity and the length and the shape of the window used in real data processing (Yang and Forsyth, 2006). The kernels also have been smoothed with a 2-D Gaussian filter to interpolate between grid points and stabilize the inversion for lateral velocity variations. The smoothed kernels represent the weighted sum of sensitivity to velocity perturbation at any grid point. The smoothing has more effects on high-frequency kernels, where high-frequency oscillations far from ray path are smoothed out (Fig. 2.13).

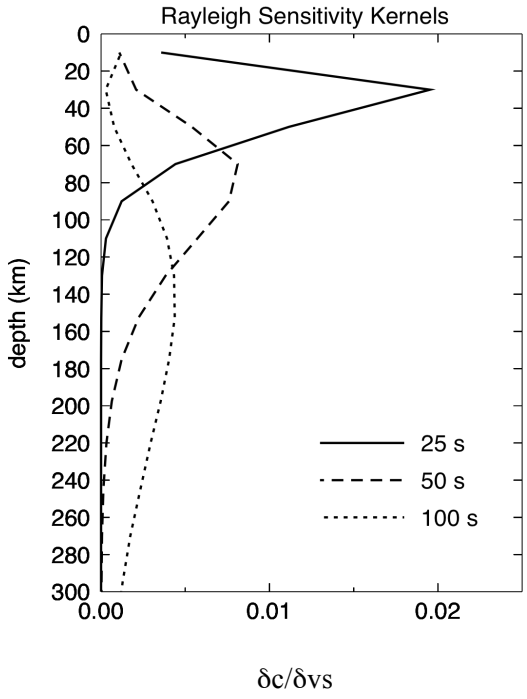

Figure 2.12 – Rayleigh wave sensitivity kernels at periods of 25 s (solid line), 50 s (long-dashed line), and 100 s (short-dased line). Partial derivatives of δc/δvs.

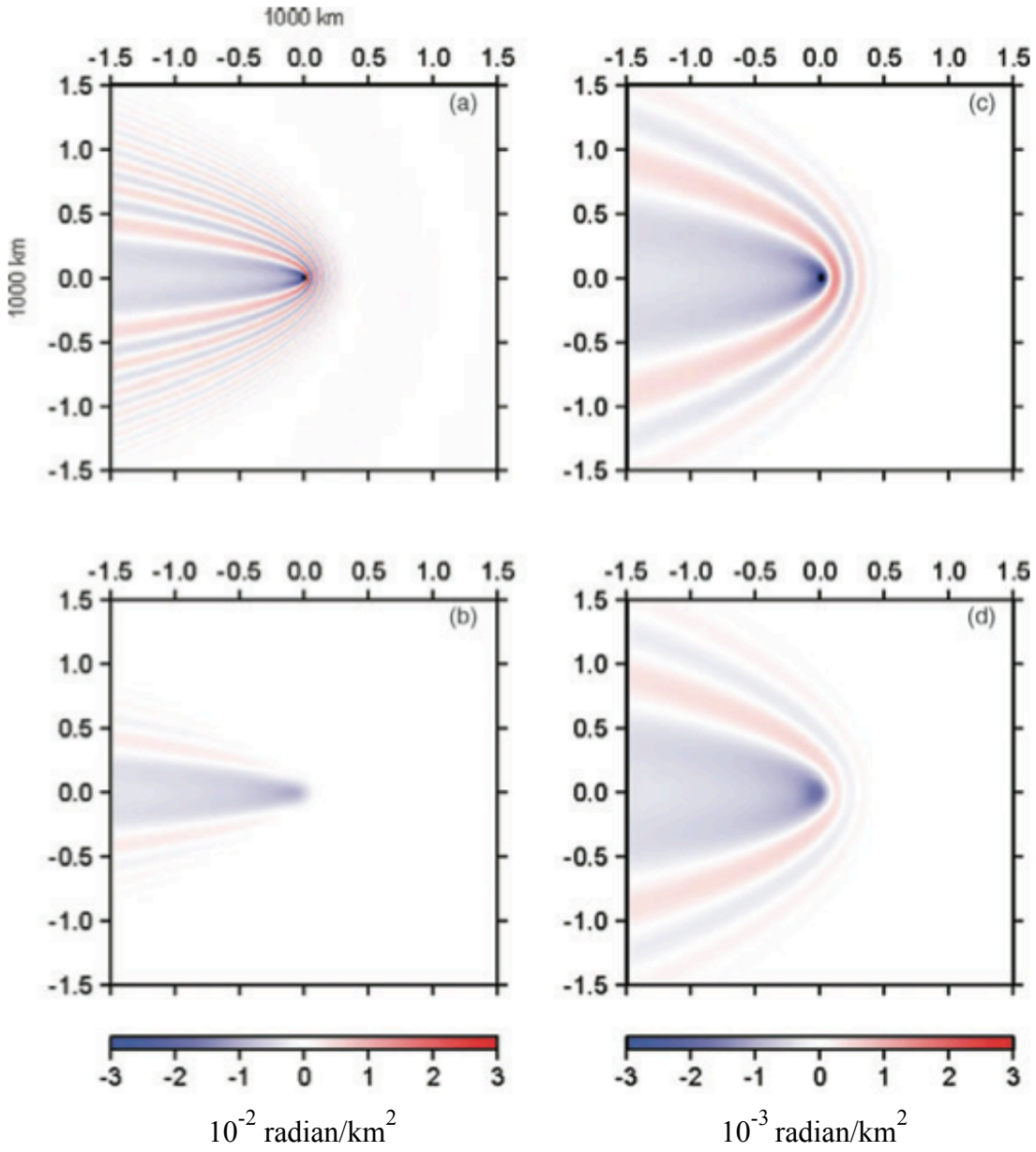

Figure 2.13 - 2-D phase sensitivity kernels at 25 s (a-b) and 100 s (c-d); (b) and (d) are smoothed kernels for (a) and (c) respectively. A characteristic length of 80 km is used in the Gaussian smoothing applied to the kernels. The smoothing has more effects on the sensitivity of shorts periods. (From Li, 2011).

Li (2011) computed Rayleigh-wave phase velocities in Southern Africa from the TPW inversion method using both the 2-D sensitivity kernels and the Gaussian sensitivity functions. The comparison reveals that finite-frequency effects are highly significant above 100 s in the TPW tomography using Gaussian functions. Furthermore, Li (2011) found that phase velocities from the 2-D kernel inversions show better correlations between adjacent frequencies and that the correlation improves with increasing period.

To solve for azimuthal anisotropy, Rayleigh wave phase velocity c at a given frequency ω is expressed as a function of azimuth ψ,

$$c(\omega,\psi) = A_0(\omega) + A_1(\omega)\cos(2\psi) + A_2(\omega)\sin(2\psi) + A_3(\omega)\cos(4\psi) + A_4(\omega)\sin(4\psi) \qquad (3)$$

where A_0 is azimuthal averaged phase velocity, and A_1-A_4 are azimuthal anisotropic coefficients (Smith and Dahlen, 1973). The 4ψ terms are ignored in my calculation because the coefficients for them are small (Smith and Dahlen, 1973). In the inversion for phase velocities, I simultaneously solve for isotropic term A_0 and azimuthal term A_1 and A_2 (Forsyth and Li, 2005). If anisotropy is allowed to vary at each grid node, the model parameters for phase velocities are 3 times of the isotropic case. To reduce the number of model parameters I only inverted for the average anisotropy in a region including the range and the area north of it (Fig. 2.12), and kept other areas as isotropic in the inversion. The amplitude of anisotropy is expressed as $(A_1^2 + A_2^2)^{1/2}$, and the fast propagation direction is represented as $1/2 \arctan(A_2/A_1)$. The fast direction is constant within the range but can vary for each period. Because surface-wave data at different periods sample velocity at different depth ranges, it is possible to constrain the distribution of anisotropy with depth.

2.5 Results

2.5.1 1-D phase velocities

We first inverted for average phase velocities of the central Tien Shan by assuming that velocity is uniform in the entire study area or in each sub-region at a given period. The sub-regions are chosen according to major tectonic provinces, the Kazakh shield, the Tarim basin, and the Tien Shan. I also divide the Tien Shan range as the western part (west of 78° meridian) and the eastern part (east of 78° meridian) based on the evidence that these two regions are characterized by differences in mantle seismic velocities (Vinnik *et al.*, 2004 and 2006, Xu *et al.*, 2007), gravity anomalies (Burov *et al.*, 1990), deformation rate (Reigber *et al.*, 2001), and the amount of shortening (Avouac *et al.*, 1993). Grid nodes for the sub-regions are shown in figure 2.11. The obtained average phase velocities as a function of period are shown in figure 2.14.

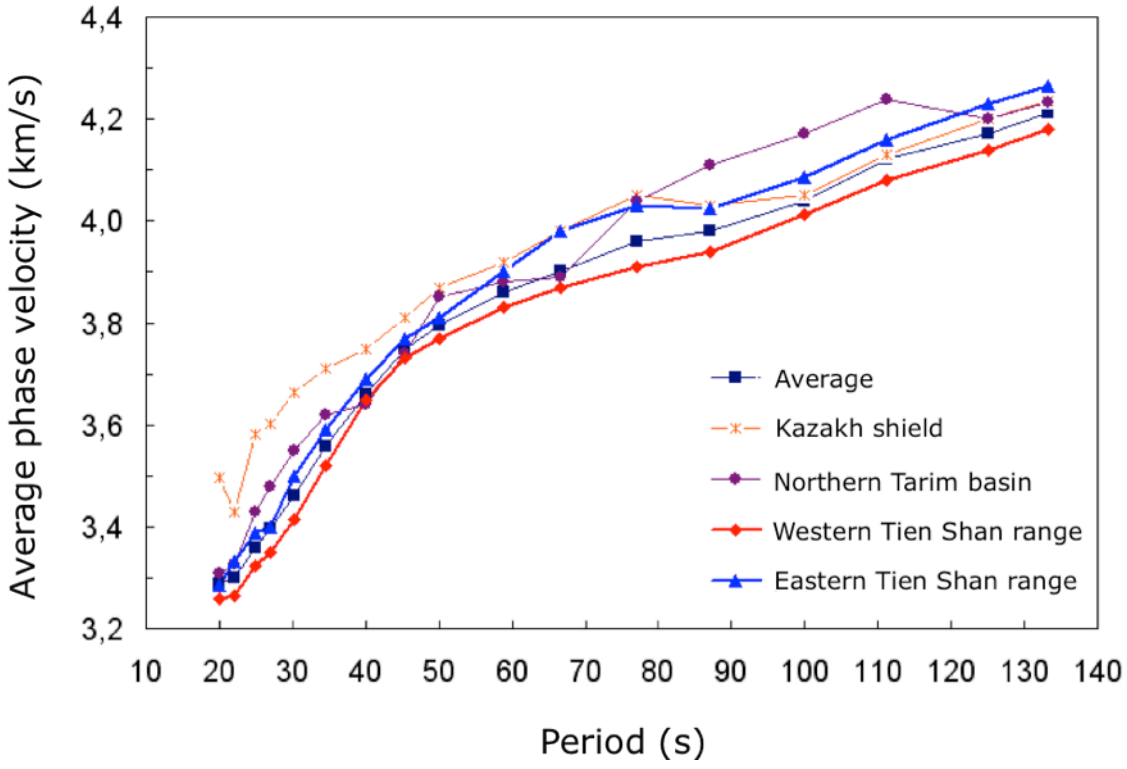

Figure 2.14 - Phase velocity dispersion curves obtained in 4 sub-regions: the Kazakh shield, the northern Tarim basin, the western Tien Shan and the eastern Tien Shan. The black curve is the average for the whole area. The colours of the curves correspond to the colours in the grid map in figure 2.11.

The average phase velocity of the study area increases from 3.29 km/s at 20 s to 4.21 km/s at 133 s. Small standard deviations of about 0.005 km/s are associated to these values. Dispersion curves show that the Tien Shan range is in general slower than the Tarim basin and the Kazakh shield, two Archean provinces that bound the Tien Shan to the south and north, respectively. Compared with the average dispersion, the southern

Kazakh shield is ~0.1 km/s faster at 20-80 s, indicating a fast lithospheric lid. The Tarim has a similar dispersion as in the Tien Shan at periods of 20-80 s but is ~0.15 km/s faster than the average at long periods, indicating a thicker and presumably cold lithosphere beneath it. This observation is consistent with the thick Tarim lithosphere imaged from P wave tomography (Xu *et al.*, 2002; Lei and Zhao, 2007) and from receiver functions (Kumar *et al.*, 2005). I also found that the western part of the central Tien Shan is constantly slower than the eastern part, and the difference is more significant between 50 s and 90 s.

Another interesting feature is the change in the slope of dispersion curves. The change is at about 45 s along the range while it occurs at slightly shorter period of 35 s in the southern Kazakh shield. This slope change is related to the velocity change from the crust to the mantle and the observation suggests that the crust beneath the Tien Shan is thicker than in the Kazakh shield. At the period range of 75-100 s, phase velocities decrease with period for the southern Kazakh shield and for the eastern central part of the Tien Shan, which probably reflects a strong velocity contrast from the lithosphere to the asthenosphere. A lithosphere-asthenosphere transition at 77 s is in good agreement with the ~100 km thick lithosphere beneath the central Tien Shan determined from S receiver functions (Oreshin *et al.*, 2002; Kumar *et al.*, 2005).

2.5.2 2-D isotropic phase velocity variations

I used the average phase velocity to generate the 2-D sensitivity kernels and also as starting values in 2-D phase velocity inversions. The 2D lateral variations of isotropic phase velocities at each period (Fig. 2.16) are obtained by allowing the phase velocity coefficient A_0 to vary at each node. The coefficients at these nodes are used to generate maps of lateral phase velocity variations on a finer, 0.1° spacing grid for plotting purposes by averaging the values at neighboring nodes using a Gaussian weighting function with a characteristic length of 75 km, the same value as used in smoothing the 2-D sensitivity kernels. Standard errors of phase velocities in these maps were estimated from the covariance matrix of the phase velocity coefficients by linear error propagation (Clifford, 1975) and given by

$$\sigma^2_v = \mathbf{q}\mathbf{C}_{MM}\mathbf{q}^T \quad (4)$$

where $\mathbf{q}$ is the vector of weights for all the grid points for a particular position and $\mathbf{C}_{MM}$ is the complete, *a posteriori*, model covariance matrix. The resolution maps of twice the standard errors of phase velocities for all the period are shown in figure 2.16. The lower the contour level is, the higher the resolution. The resolution is highest at the center of the study area, which is sampled by a large number of crossing ray paths, and gradually decreases toward the edge. The magnitude of errors generally increases at very short and long periods because of a smaller number of high-quality waveforms. Phase velocity lateral variations are shown in figure 2.16 at seventeen periods from 20 s to 133 s. The anomalies are calculated relative to the 1-D average phase velocity in the area as shown

in figure 2.12. Maps of velocity perturbations show only the area within the 1.25% error contour at 50 s.

In the periods between 20 s and 50 s, phase velocities are strongly influenced by crustal structure. Slow anomalies are imaged in the Tien Shan and fast anomalies are in the Tarim Basin and the Kazak shield. A low velocity zone parallel to the mountain range is observed in the western and central Tien Shan at periods of 20 s to 30 s. At the very short period of 20 s the slow anomaly is very broad and extends toward the Tarim basin, it can reflect the high sediments thickness in the basin. At periods of 25 s and 30 s a fast anomaly is present just beneath the Naryn basin. Between 25 s and 35 s the low velocity anomaly is located just along the Tien Shan – Tarim basin boundary, where a high velocity anomaly is imaged just next it to the south in the Tarim Basin. This strong and sharp phase velocity variation can be due to a sudden change in crustal thickness. At the periods of 45 and 50 s, the slow anomaly in the southwest extends northward and is in the whole western part of the Tien Shan range.

At longer period in the range of 59-125 s, the most consistent feature in the map is a low velocity zone characterized by a more circular shape localized in the northwestern part of the range although the strength of the anomaly decreases with period generally. This slow anomaly is not imaged on the longest period of 133s, which is probably be due to poor resolution at this frequency. Fast anomalies in the Kazakh shield and the Tarim basin reduce its strength from more than 3% at shorter periods to about 1% at periods of 59, 60 and 77 s and not significant at longer periods. A fast anomaly appears in the eastern part of the Tien Shan range from 50 to 67 s, consistent with the trend observed on

the 1-D dispersion curves, indicating a relative fast lithosphere. The fast anomaly at 87 to 100 s extends along the strike of central to eastern Tien Shan range, which might reflect the subducted Tarim lithosphere. I notice some inconsistence between the 2D phase velocities and the 1D inversion results in different sub regions. For example, the eastern Tien Shan is not fast in the 2D map as shown on the dispersion curves. At 77-111 s, disagreement between the maps and the 1D curves occurs for the northern Tarim Basin, which is imaged with high velocity in the 1D average but not that fast in the map. Such disagreement is probably caused by different techniques applied in the inversions because the 1D inversion used the Gaussian smoothing function while the 2D inversion used the Born, approximation sensitivity kernels. As pointed out by Li (2011), the difference between the two techniques is more noticeable at longer periods.

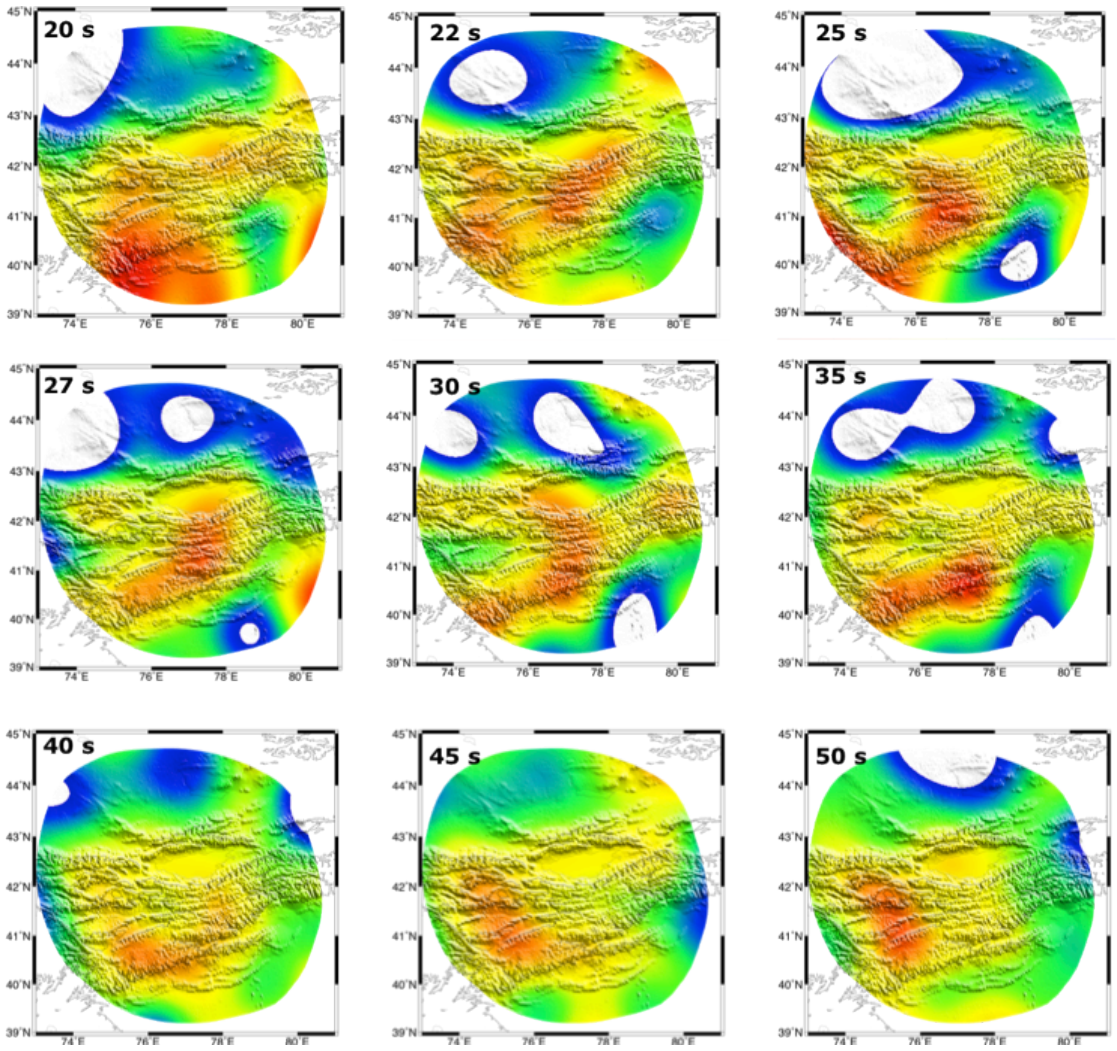
20 s
22 s
25 s
27 s
30 s
35 s
40 s
45 s
50 s
45°N
44°N
43°N
42°N
41°N
40°N
39°N
74°E
76°E
78°E
80°E

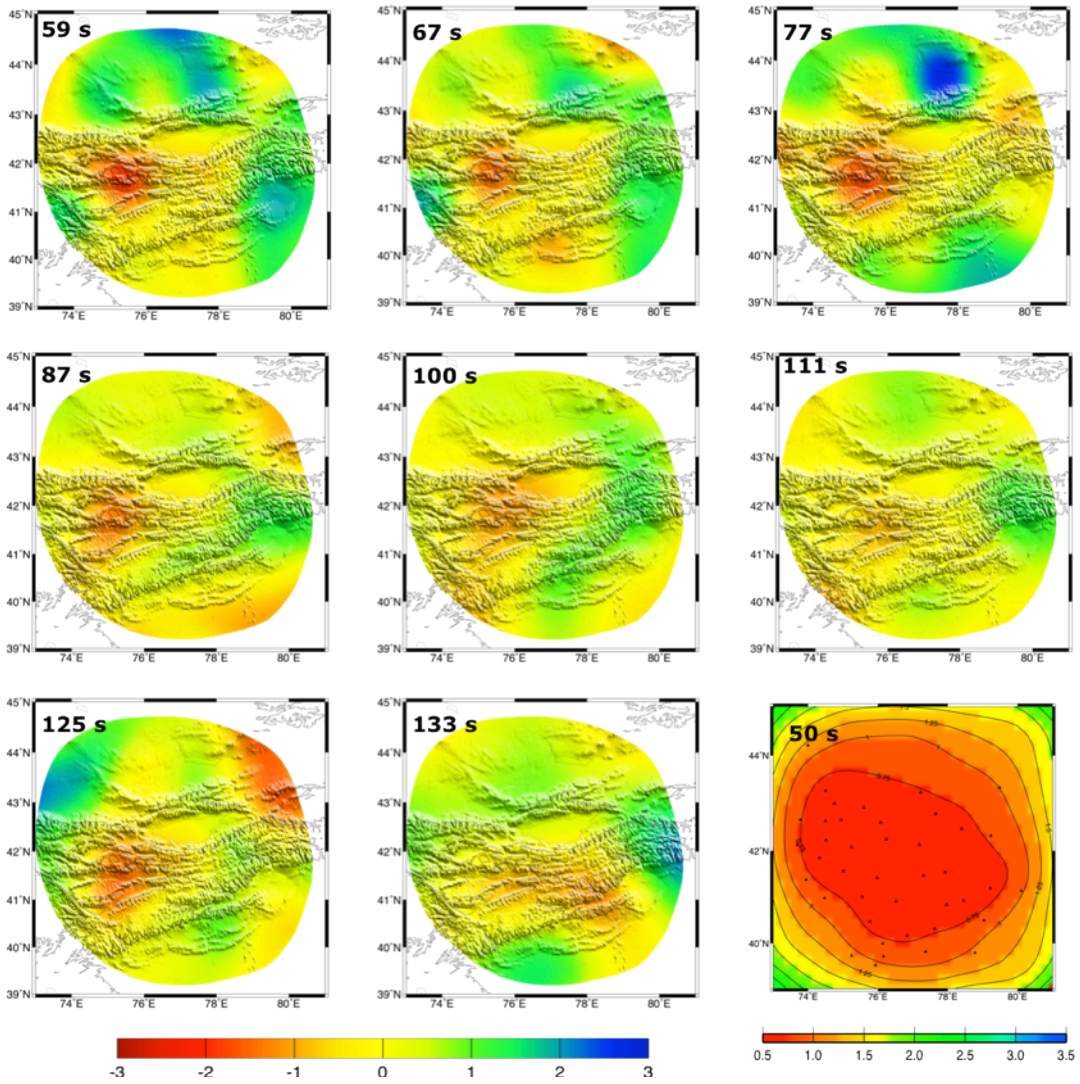

Figure 2.15 - Phase velocity variation maps in the period range of 20-133 s. The topographic contour is shown in light black. The velocity perturbations are shown only in the area within the 1.25% error contour at 50 s as shown at the low right figure in the bottom row.

2.5.3 Resolution test

The events used in this study show a good azimuthal coverage (Fig. 2.5), which is important for resolving both lateral heterogeneity and azimuthal anisotropy. The large number of stations and events ensures dense crossing ray paths through the study region (Fig. 2.6), The reduction of ray path coverage at short and long periods is due to multipathing and the decrease of signal-to-noise ratio, respectively.

Although the error contours (Fig. 2.15) reflects lateral resolution of phase velocity model in general, I conduct checkerboard tests here to investigate on what scale and at what frequency anomalies can be resolved. The checkerboard model consists of alternatively high and low velocity cells of 2° in longitude and 1.5° in latitude (Fig. 2.16). Each cell has a constant velocity 3% above or below an average velocity of 4.0 km/s. I calculate synthetic phase and amplitude data from the theoretical phase velocity model, which is discretized into a 0.5° x 0.5° grid as the real model. The input model in figure 2.16 has smooth transitions between high and low velocity regions because smoothing is applied in generating the map.

The synthetic Rayleigh wave data share the same event information, ray paths and two-plane waves as the real data. I compute synthetic data at every period. Random noise equal to 0.1 is added to the predicted amplitudes and phases based on the standard errors of real data. Then I use the synthetic data to reconstruct the velocity model by the same inversion method and smoothing factor as used for the real data. The resulting models for each period are shown in figure 2.16. The anomalies can be well recovered in the study region, some lateral smearing effect is observed to the northeast and southeast of the

study area. At the long period beyond 111 s, the resolution becomes poor. It can be seen that at 125 s, the slow anomalies are better resolved while at 133s fast anomalies are better resolved. Given the resolution test, only the most consistent features imaged at different frequencies are considered robust and discussed in later section.

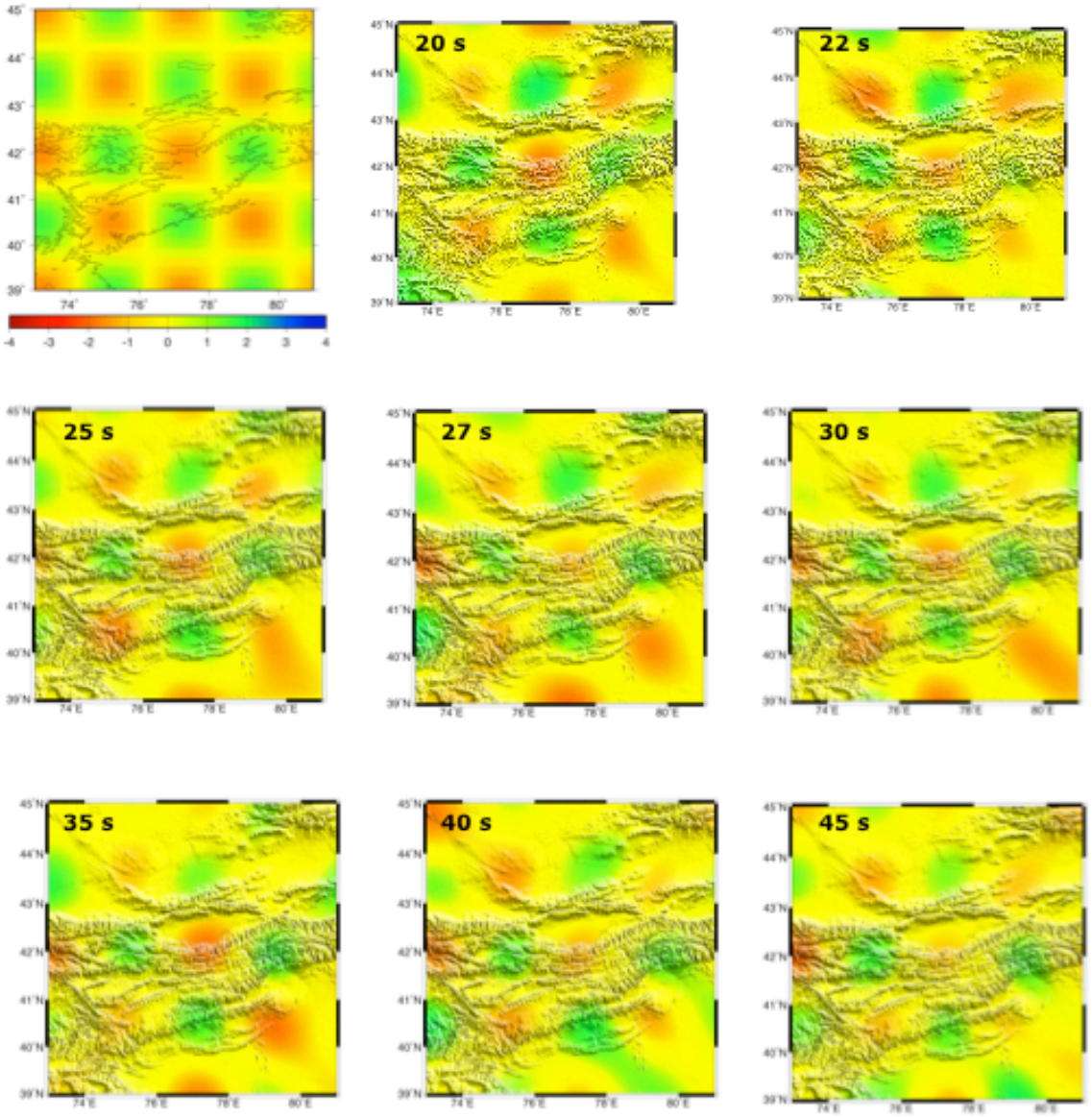

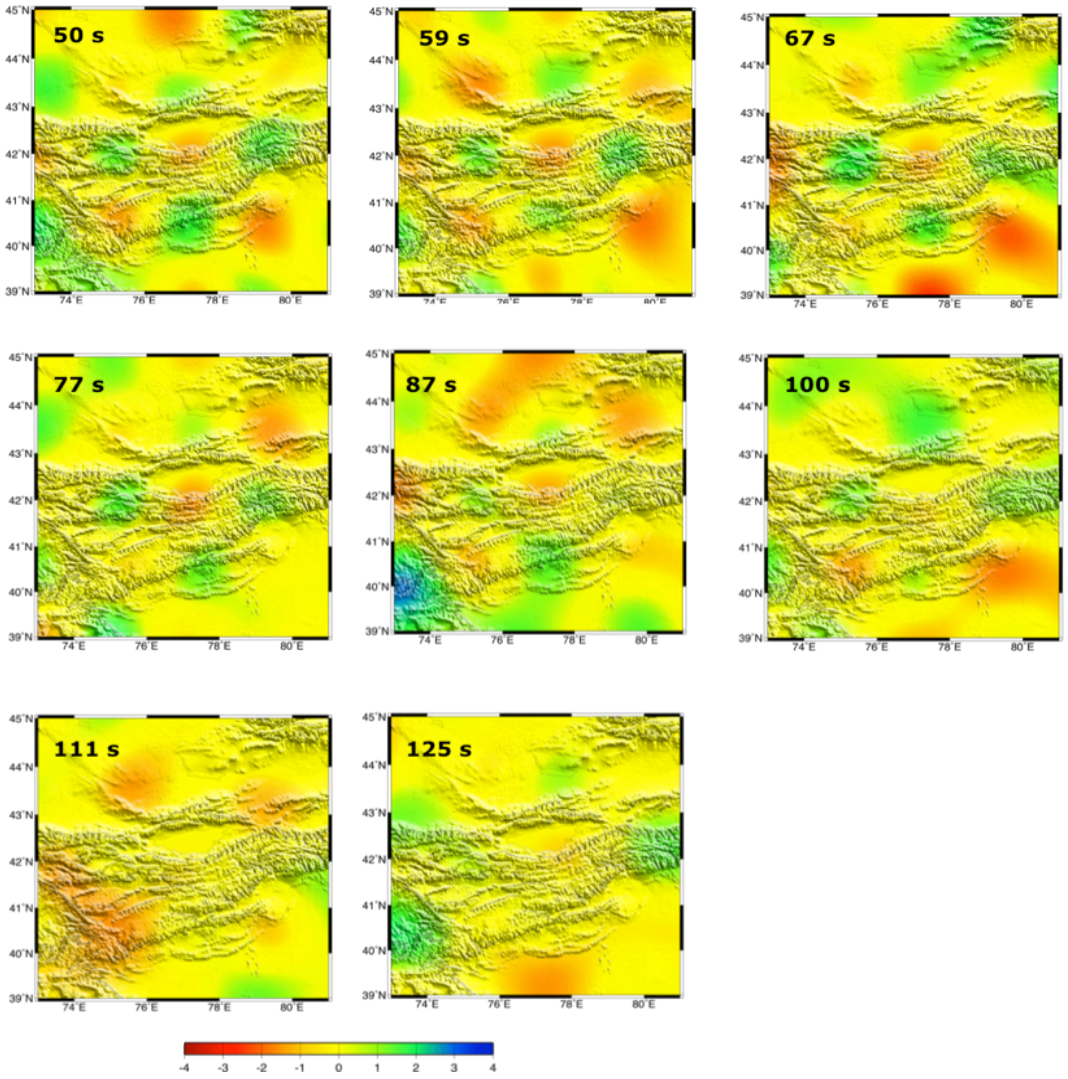

Figure 2.16 - Input and recovered models for the checkerboard test. Input model of 2° x 1.5° cells with ±3% velocity disturbance. On each map the analyzed period is reported.

2.5.4 Azimuthal anisotropy

Seismic azimuthal anisotropy means that the seismic velocity varies with the propagation direction or polarization of the waves. Seismic anisotropy in the Earth's upper mantle is generally attributed to crystallographic or lattice (CPO or LPO) preferred orientation of anisotropic crystals in minerals such as olivine and pyroxene (e.g. Nicolas and Christensen 1987). The elongate crystalline structure of these minerals tends to align with mantle flow. Olivine, the primary upper mantle mineral constituent, has an intrinsic single-crystal shear wave anisotropy of ~18% and olivine LPO makes the largest contribution to upper mantle anisotropy. Seismic anisotropy results from a combination of frozen-in lithospheric anisotropy from past deformation processes, shear coupling between the lithosphere and asthenosphere and current flow in the asthenosphere (Park and Levin, 2002). Because of this link between deformation and anisotropy, the characterization of anisotropic structure can yield some of the most direct constraints available on dynamic processes in the Earth's interior. The dependence of surface-wave velocities upon propagation direction contains information about azimuthal anisotropy. Fundamental mode surface-waves are sensitive to anisotropy in the uppermost few hundred kilometers of the mantle (e.g., Montagner and Nataf, 1986).

Azimuthal anisotropy beneath the central Tien Shan can also be solved simultaneously with phase velocity through the two-plane-wave inversion. In this inversion, the coefficients of 2ψ terms (A1 and A2 in equation 1) are added as additional model parameters. If anisotropy is allowed to vary laterally at each grid node, the number of model parameters for anisotropy will be two times of that for phase velocity (A_0). Given

that anisotropy is usually weak and A_1 and A_2 are expected to be small, the model parameters for 2D anisotropy variation cannot be well resolved. To reduce the model parameter for anisotropy, I only solve the average anisotropy in a region including the range and the area north to it, which is outlined by a thick black line in figure 2.11. Anisotropy is constrained to be uniform within the selected region and other areas are kept as isotropic in the inversion. With this treatment, only two model parameters for anisotropy are needed.

The fast direction and the amplitude of anisotropy are calculated as described in the previous section and the results are shown in Figure 2.17.

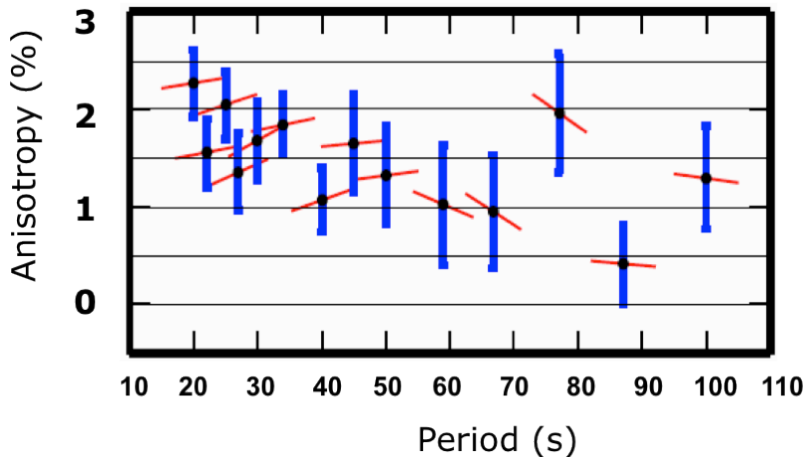

Figure 2.17 – Variations of azimuthal anisotropy with period beneath the Central Tien Shan range. Fast directions of azimuthal anisotropy are indicated by the orientations of red bars as if in a map view with north up on the diagram. Amplitudes represent contrast between fast and slow direction as percentage of average phase velocity. The blue vertical bars represent plus or minus one standard deviation of the amplitude.

Amplitudes represent phase velocity contrast between the fast and slow directions as percentage of the average phase velocity. Anisotropy at periods of 20-50 s is roughly constant with amplitude of 1-2% and a fast direction of ENE-WSW parallel to the strike of the central Tien Shan range. This averaged fast direction is in general agreement with the shear wave splitting measurements at most stations in the central Tien Shan (*Li and Chen, 2006*) (Fig. 2.18). The observation of strike-parallel fast direction indicates that the Tien Shan lithosphere deforms coherently with the N-S compression due to the active collision at the India-Asia plate boundary. The anisotropy from long periods (59-100 s) show a fast orientation of WNW-ESE with more variable amplitude, reflecting a change of anisotropy at depth. The WNW direction is consistent with the absolute plate motion of the Eurasia plate relative to hotspots (Gripp and Gordon, 2002) and the anisotropy can be simply explained as due to the large scale mantle flow. A more EW fast direction at periods of 45 s and 50 s reflects the transition between the two anisotropic layers.

There are two discrepancies between anisotropy results from surface-waves and from shear wave splitting data. First, the anisotropy associated with the absolute plate motion is not observed in shear wave splitting study. This discrepancy can be reconciled considering that the deep anisotropy is weak due to the small speed of the Eurasian plate and that anisotropy from shear wave splitting study is an integral result beneath the station from the core-mantle boundary to the surface. Secondly, Li and Chen (2006) found a NNE-SSW fast orientation at stations in the south of the Tien Shan and around the Issyk Kul based on SKS splitting analysis. The lack of this anisotropic component in

surface-wave results is probably due to the poor lateral resolution of surface-waves which constrain only the average anisotropy in the study area.

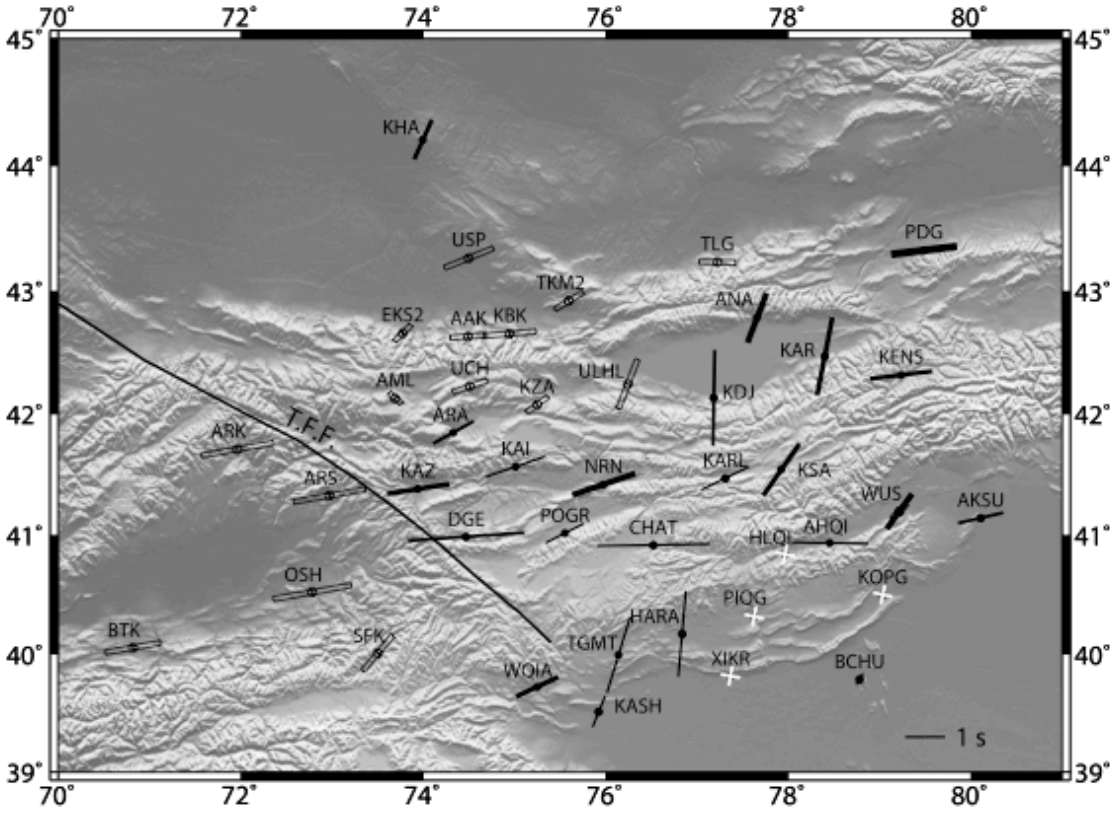

Figure 2.18 - Shear wave splitting measurements (Makeyeva *et al.,* 1992*;* Wolfe and Vernon, 1998; Li and Chen, 2006). The orientation of a bar indicates fast orientations and the bar length is proportional to delay times. The width of a solid bar is proportional to the number of individual measurements at a station. Null measurements are plotted as white crosses. The two lines of a cross are oriented parallel and orthogonal to the event back-azimuth direction, respectively.

3 RAYLEIGH WAVES PHASE VELOCITIES FROM AMBIENT NOISE TOMOGRAPHY

3.1 Introduction

For seismic surface-waves, teleseismic transmission results in the loss of the high frequency signals that are needed to infer the detailed structure of the Earth's crust. A recent innovation in seismic imaging based on using long time sequences of ambient seismic noise moves beyond some of the limitations imposed on earthquake-based methods to reveal higher resolution information about the crust and uppermost mantle. This method is called Ambient Noise Tomography (ANT), and has been applied predominantly to seismic surface-waves (*McGraw Hill Yearbook of Science and Technology ,2008*).

Any mechanism that produces waves that propagate coherently between a pair of seismometers can be used as a basis for seismic tomography. This idea, having a long history in seismology was considered again by *Lobkis and Weaver* (2001) who have shown in laboratory and theoretical studies that cross-correlations between recordings of diffuse waves at two receiver locations yield the "Green's function" between these positions. The Green's function contains all the information about wave propagation in the medium between two stations. Therefore, the estimated Green's function from the cross-correlations can be used to recover information about the medium between the 2 receivers.

Surface-waves appear strongly on cross-correlations of long-sequence ambient noise and their dispersion characteristics are readily identifiable (Fig. 3.1) (Shapiro and

Campillo, 2004), because they dominate the Green function between receivers located at the surface and also because ambient seismic noise is excited preferentially by superficial sources, such as oceanic microseisms and atmospheric forcing (Friedrich *et al.*, 1998; Rhie and Romanowicz, 2004). In fact, the primary frequency content of the estimated waves lies in the microseismic and 'earth hum' bands from about 6 s to 100 s period with the highest amplitude in the microseismic band (5-20 s). The source of ambient noise at periods below 20 sec is probably due to primary (12-18 sec) and secondary microseisms (6-9 sec) occurring in oceanic shallow waters. The microseisms are seismic waves that are produced by ocean waves and can propagate deep into continental interiors. The primary microseism results from the direct interaction between the oceanic surface gravity wave and the shallow seafloor through the exponential decay of pressure with depth. Microseismic amplitudes peak near 8 s and 16 s period, and extend to long periods merging in "earth hum" at periods above 20 s.

The fact that surface-waves can be easily identified on cross-correlations of long-sequence ambient noise suggests a possibility to measure broadband Rayleigh waves dispersion curves between any desired pair of seismic stations. Their dispersion characteristic can be measured in a broad range of periods. By correlating vertical components of ambient noise records at stations separated by distances ranging from about 100 km to more than 2000 km Shapiro and Campillo (2005) demonstrated that it is possible to extract fundamental mode Rayleigh waves at period from about 7 sec to more than 100 sec. Yao *et al.* (2006) showed that noise correlations for different months give consistent results, and that the estimated Green Functions are not biased by individual earthquakes. Bensen *et al.* (2007) have shown that good signals are obtained from one-

year ambient noise cross-correlation (Fig. 3.2) and gave a detail description on data processing procedures for ambient noise data.

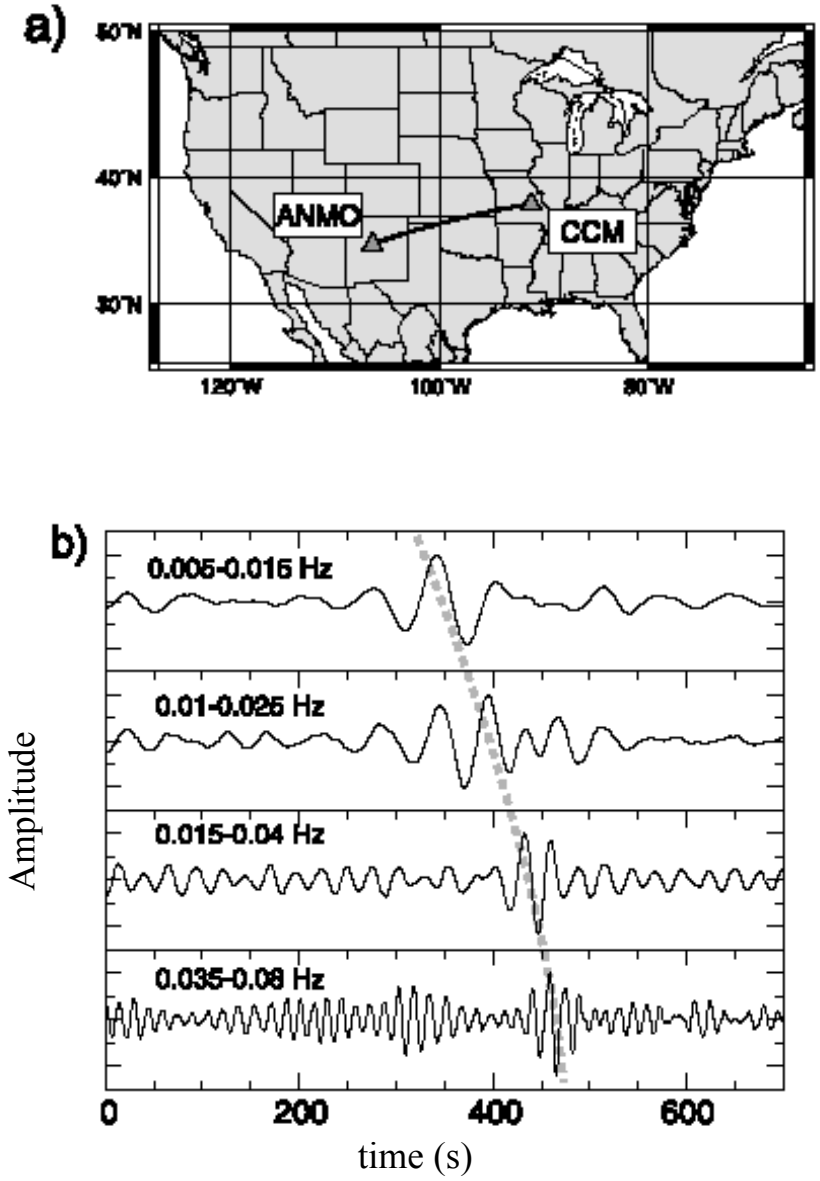

Figure 3.1 – **(a)** Map showing the station location. **(b)** Cross-correlations of vertical-component records bandpassed with different filters as indicated in top left corners of each frame. Gray dotted line emphasizes the dispersion of the emerging signal. From *Shapiro and Campillo* (2004).

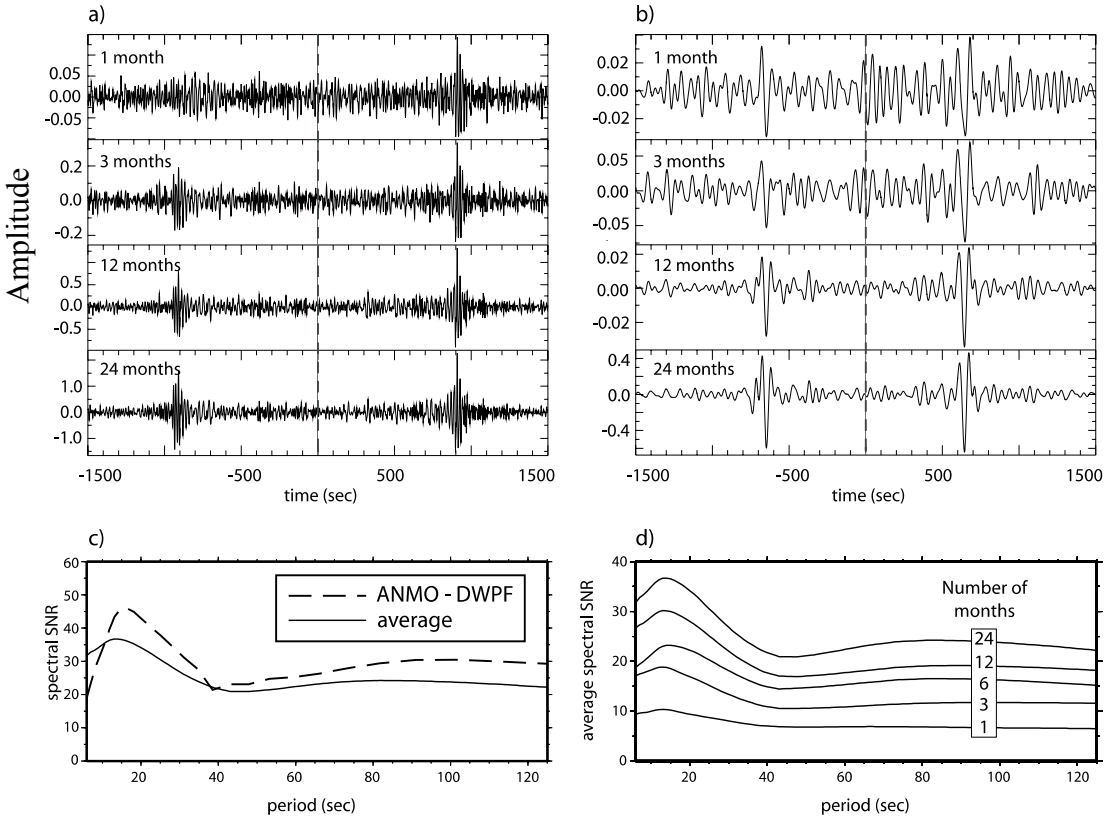

Figure 3.2 - Example of the emergence of the Rayleigh waves for increasingly long time-series. (a) Cross-correlations at the specified time-series lengths for the station pair AMO-DWPF bandpassed between 5 and 40 s period. (b) Same as (a), but for a passband between 40 and 100 s period. (c) Spectral SNR (signal to noise ratio) for the 24-month ANMO-DWPF cross-correlations and the spectral SNR averaged over all cross correlations. (d) Spectral SNR averaged over all cross-correlations for different series lengths. (From *Bensen et al., 2007*).

There are four obvious advantages of this new technique (Shapiro and Campillo, 2005).

1) Group and phase velocity measurements can be obtained in any direction of propagation and do not depend on the source location and phase, while measurements from earthquake data often sample preferential directions.

2) The sensitivity zone of the measurements is located in a narrow region connecting two stations while teleseismic surface-waves provide average values over extended areas. Therefore this new method has a potential to increase the model resolution of the structure by increasing the density of stations.

3) The measurements extend to a short periods for a dense array while short-period measurements from teleseismic surface-waves are less constrained because of intrinsic attenuation and scattering.

4) The noise does not depend on the earthquake occurrence and can be recorded in any location almost continuously.

Therefore, in a region with good station coverage the short period dispersion maps produced by this method can provide homogeneously distributed information about shear wave velocity in the crust and upper mantle with improving lateral resolution over traditional surface-wave methods (Shapiro and Campillo, 2005). Moreover, the broad frequency content, which extends to periods below 10 s, gives the vertical resolution needed to resolve crustal from mantle structure clearly.

The ability to constrain surface wave speeds at periods from 6 to 20 s, which are sensitive to crustal depths but difficult to measure from teleseismic earthquakes, provided much of the early interest in the method. In the last decade, the ANT has been widely

applied on both continental and regional scale with great success (Sabra *et al.*, 2005a and 2005b; Yao *et al.*, 2006; Yang *et al.*, 2007; Yao and Van der Hilst, 2009; Stehly *et al.*, 2009).

3.2 Data and data processing

I used two-year ambient noise records at all the 41 stations in the Tien Shan (Fig. 2.1) from September 1998 to August 2000. Only vertical component data were analyzed in order to obtain Rayleigh wave signals on the resulting cross-correlations.

The procedure of analyzing ambient noise recordings is the same as described by Bensen *et al.* (2007), which was designed for a broad range of periods, interstation distances and geographical scales.

The data processing is divided in four main phases: (1) single station data preparation, (2) cross-correlation and temporal stacking, (3) measurements of velocity dispersion, (4) quality control, including error analysis, and data selection. A schematic representation of this procedure is shown in figure 3.3.

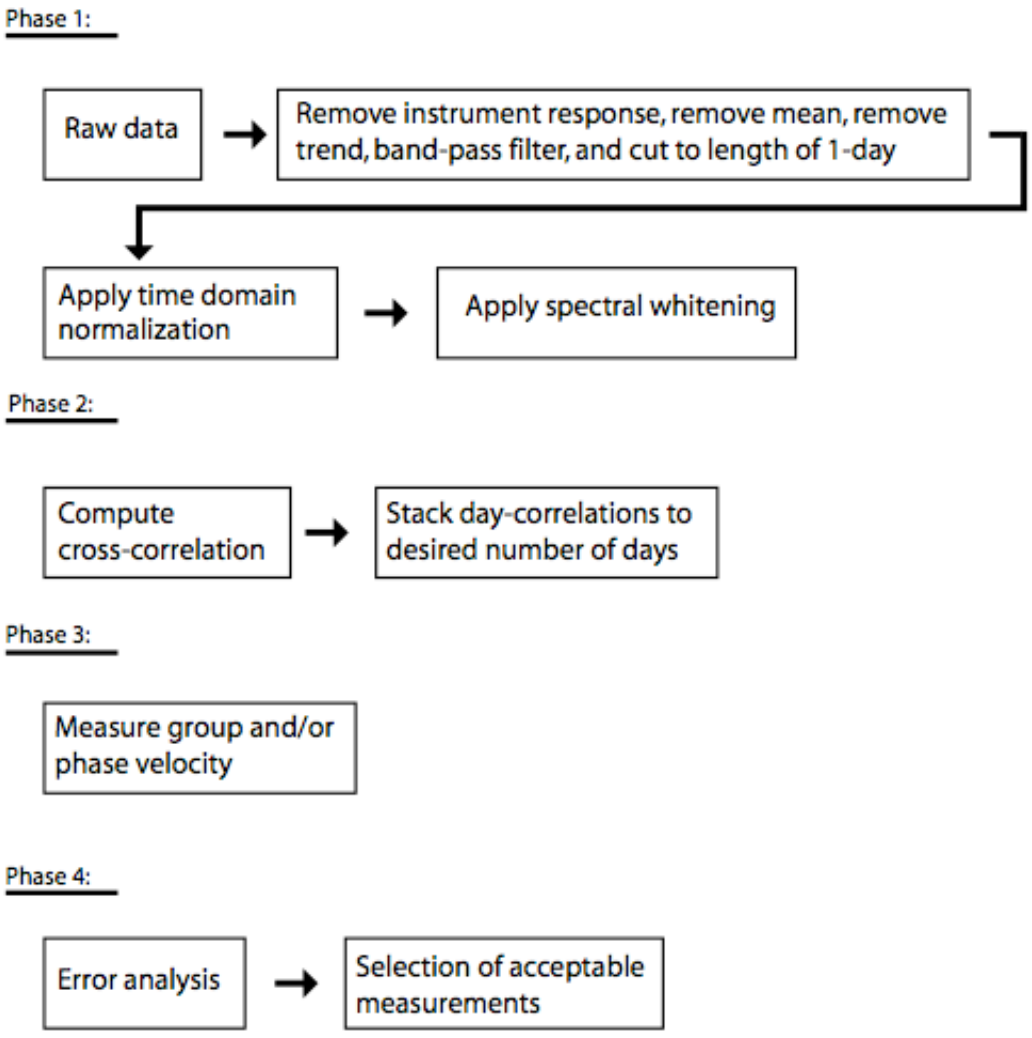

Figure 3.3 - Data processing scheme from *Bensen et al. (2007)*.

The aim of the first phase is to enhance broad-band seismic noise. Data are processed one day at a time for each station, based on several steps. First, the instrument response, the mean and the daily trend were removed from the data. The seismograms were filtered in the period range form 5 to 150 s and decimated to 1 sample per second. Then, with a

time-domain normalization procedure, I removed earthquake signals and instrumental irregularities from the time-series in order to reduce their contributions to the cross-correlations. For example, at about 20 s earthquakes signals are stronger than seismic noise and therefore it is of fundamental importance to remove them. I applied a weighted running average on the envelope of each seismogram in the time domain, which effectively removed earthquake signals while keeping much of the information on the amplitude of the ambient noise (Yang *et al.*, 2007). This procedure computes the average of the envelope of the seismogram over a normalization time interval, and weights the seismogram by the inverse of this average at the center of the window. The width of the normalization window determines how much amplitude information is retained. Yang *et al.* (2007), found that a time window with width equal to half the maximum period of band-pass filter works well. I used a temporal window of about 75 s for this study. Then I applied the spectral whitening to the data in order to broaden the band of ambient noise signal in cross-correlations and also to combat degradation due to persistent monochromatic sources.

In the second phase I cross-correlated waveforms at all possible station pairs and performed data selection later. The number of possible station pairs is 820 (41(41-1)/2) for all 41 stations. Cross-correlation is performed daily in the frequency domain and is returned to the time domain for stacking. The cross-correlations were stacked into a set of 3 months, 1 and 2 years time-series. The stacking simply adds the daily cross-correlations if the time-series cover more than 80% of the day, otherwise the data for that day are discarded. Stacking over increasingly long time-series generally improved the signal to

noise ratio (SNR). In figure 3.4 three examples of 3 months stacking are shown together with longer periods stacking of 6 months, 12 months and 24 months. The resulting cross-correlations contain clearly emergent surface wave signals coming from opposite directions along the path linking the two stations as shown in two examples in figure 3.5. These two signals appear at positive and negative correlation lag and are also called the 'causal' and 'acausal' signals. The causal and acausal part are often not identical because the source of ambient noise is not distributed homogeneously in azimuth.

To simplify data analysis and enhance the SNR, I separated each cross-correlation into positive and negative lag components and then averaged these two components to form a final cross-correlation called the 'symmetric component' (Figs. 3.6 a-b). The following analysis was performed on the symmetric components exclusively. Each symmetric component was filtered to isolate the fundamental mode Rayleigh wave at the following periods of 6 s, 8 s, 10 s, 12 s, 14 s, 16 s, 18 s, 20 s, 25 s, 30 s, 35 s, 40 s. Figure 3.6c shows an example of six narrow bandpass filtered time series with the central period indicated in each panel. Rayleigh wave signals emerge clearly in each of these period bands.

After the daily cross-correlations have been computed and stacked, the resulting waveform is an estimated Green function. Using the estimated Green function, the group and phase speeds as a function of period can be measured by using traditional frequency-time analysis (FTAN) (e.g. Dziewonski *et al.*, 1969; Levshin and Ritzwoller, 2001), and phase slowness can be derived from group velocity from a vertical component ambient noise cross-correlation (Bensen *et al*., 2007):

$$S_c = S_u + (\omega\Delta)\text{-}1\ (\phi(t_u) + 2N - \pi/4\ ) \quad (5)$$

where N=0, ±1, ±2, S_c and S_u are phase and group slowness, ω is frequency, Δ is interstation distance, $\phi(t_u)$ is the observed phase at the observed group arrival time, t_u = Δ/U, U is group speed.

Rayleigh wave phase velocity variations in this study were obtained at periods of 6 s to 40 s. Compared to group velocity, the uncertainty of phase velocity measurements is smaller and phase velocity also has a greater sensitivity for deeper structures.

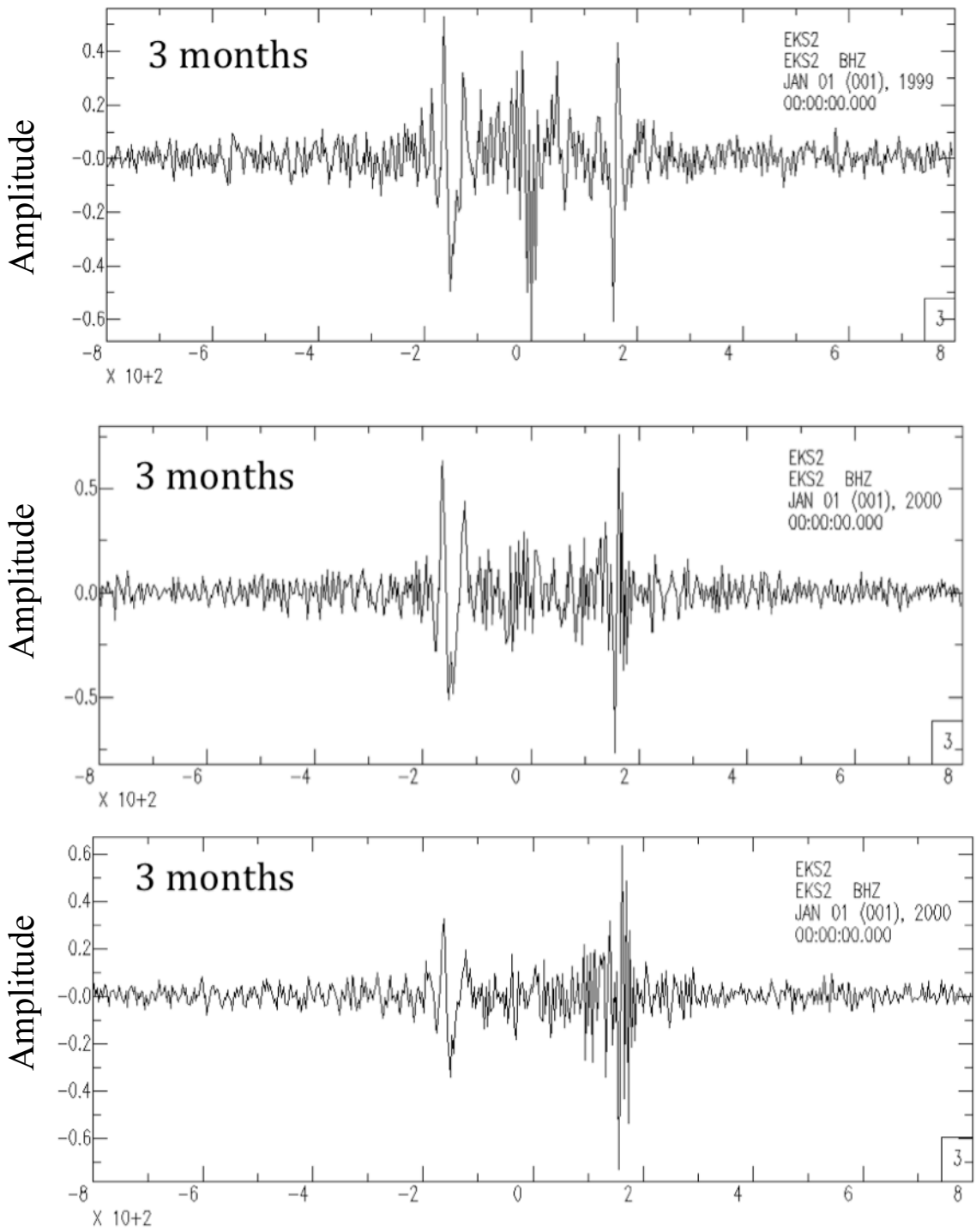
3 months
EKS2
EKS2 BHZ
JAN 01 (001), 1999
00:00:00.000
Amplitude
X 10+2
3 months
EKS2
EKS2 BHZ
JAN 01 (001), 2000
00:00:00.000
Amplitude
X 10+2
3 months
EKS2
EKS2 BHZ
JAN 01 (001), 2000
00:00:00.000
Amplitude
X 10+2
lag time (s)

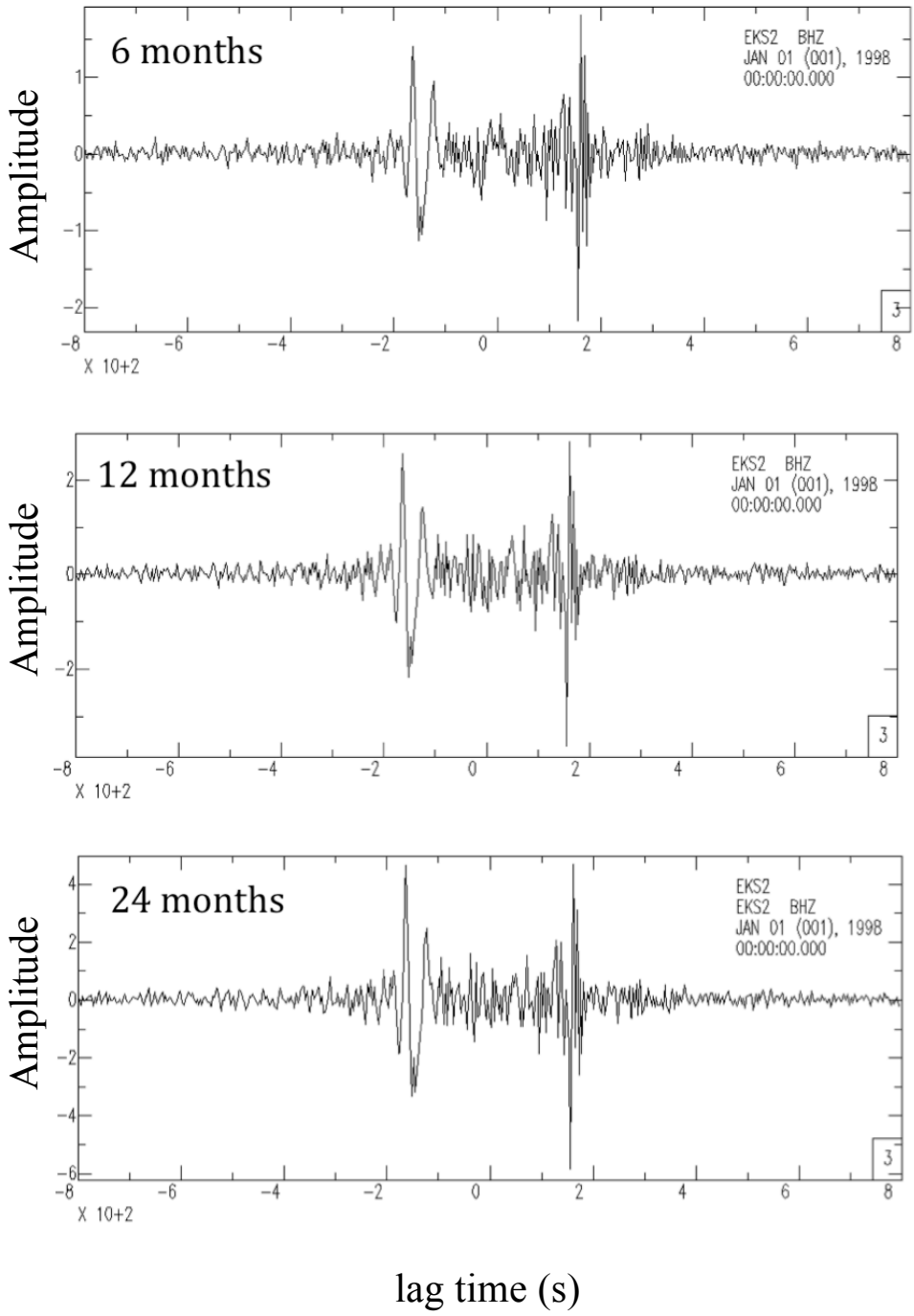

Figure 3.4 - Examples of stacking cross-correlations. In the panel there are written the number of months stacked together. **(a)** the three months stacked signals show a similar SNR. **(b)** The increasing long time series cross-corelations are characterized by an increase of SNR.

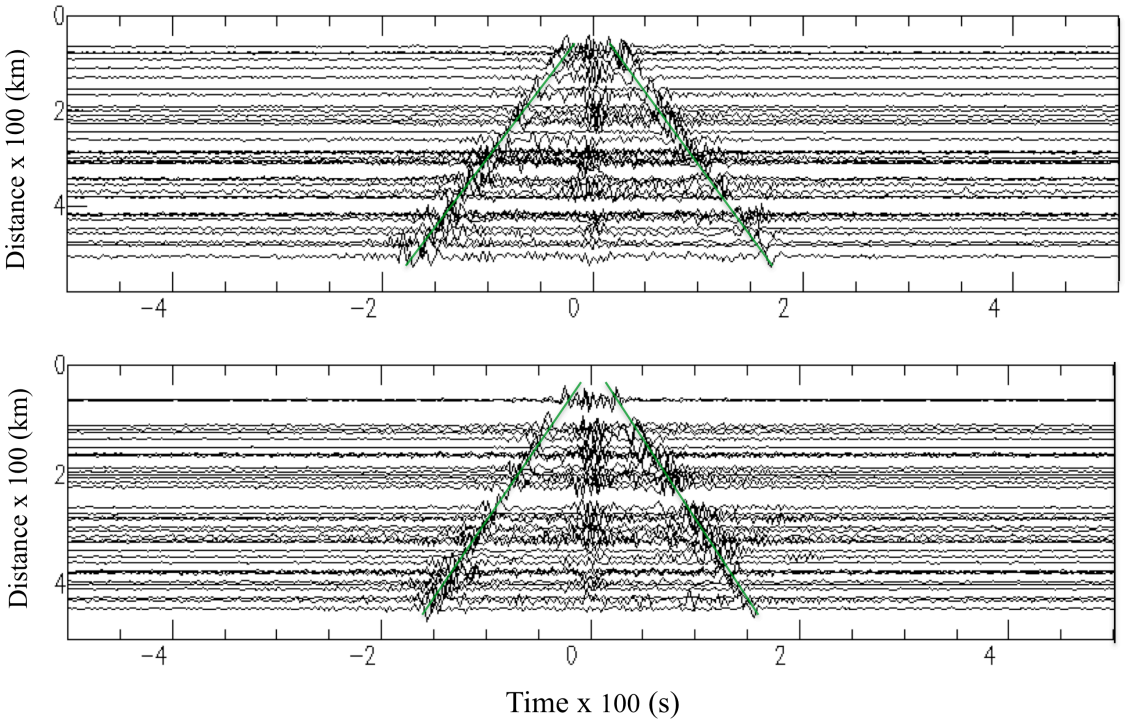

Figure 3.5 - Broad band (5-50 s) section of cross-correlations with the station KOPG (at the top) and XIKR (at the bottom). Both positive and negative lag times are shown. The green lines mark a moveout of about 3 km/s.

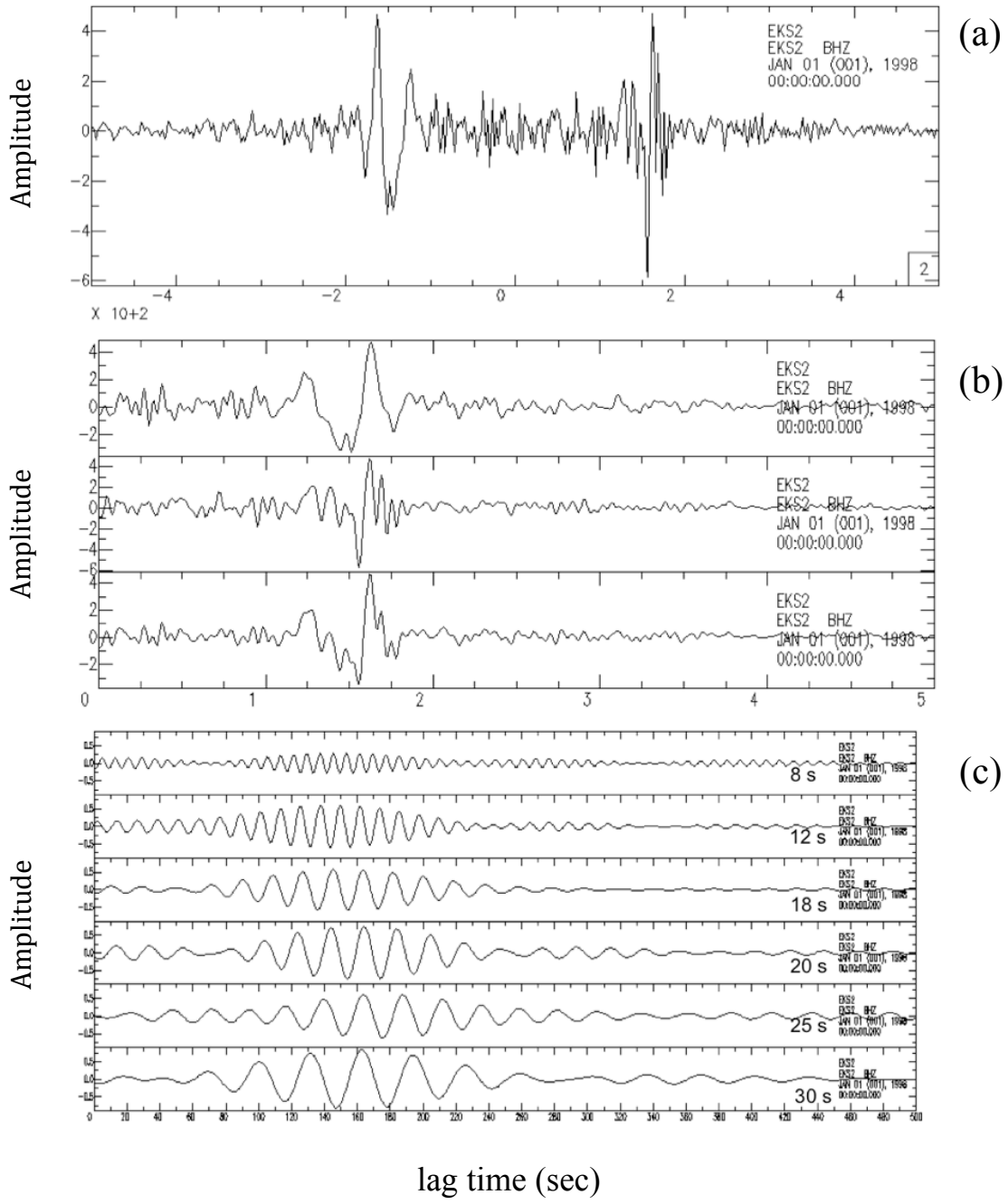

Figure 3.6 - (a) Example of broad band cross-correlation using 24 months data for stations EKS2 and WUS; **(b)** from the top to the bottom: positive lag time, negative lag time and averaged lag time are shown; **(c)** the averaged cross-correlation filtered at the various narrow bandpass with the central period indicated in the panel.

The last phase is to evaluate the quality of the dispersion measurements quantitatively. I calculated the period-dependent signal to noise ratio (SNR) for each interstation cross-correlation. The SNR is defined as the ratio of the peak amplitude within a time window containing the surface wave signals to the root-mean-square of the noise trailing the signal arrival window. The signal window is determined using the arrival times of Rayleigh waves at the minimum and maximum periods of the chosen frequency band.

3.3 Results

3.3.1 1-D Phase velocity dispersion curve

Based on the quality analysis of cross-correlations signals, I selected acceptable waveforms when the SNR of the signals is larger than 20. In table 3.1 the number of cross-correlation with SNR larger than 20 are reported for each period. The associated ray paths for periods of 10s, 14s, 16s, 18s, 20s, 30s are plotted in figure 3.7. The dispersion curves I show below have been calculated using signals with the SNR larger than 20.

Periods (s)	Cross-correlations with SNR>20
8	382
10	559
12	627
14	667
16	679
18	679
20	663
25	593
30	490
35	162

Table 1 – Number of selected cross-correlations with SNR larger than 20, for each filtered period.

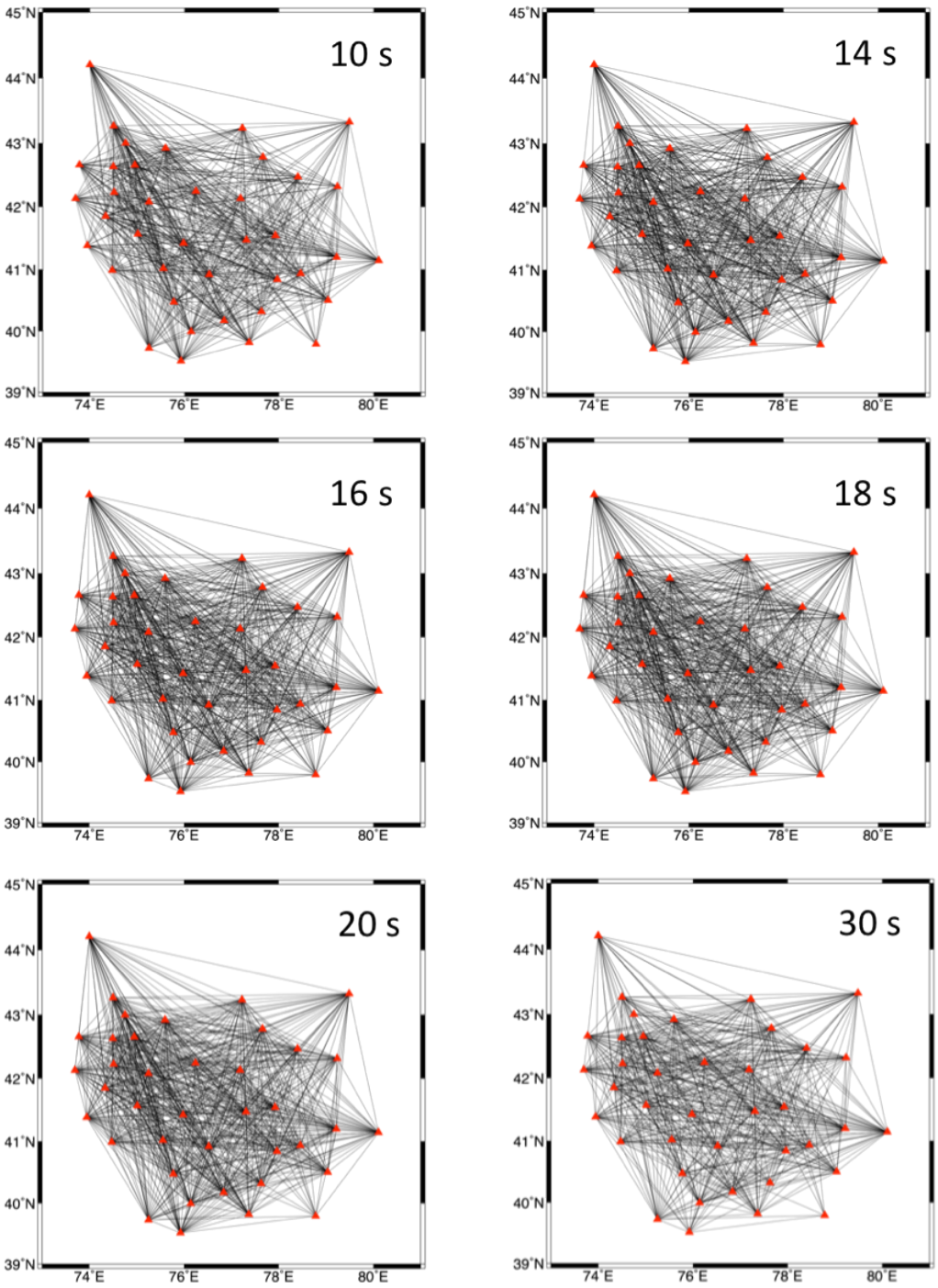

Figure 3.7 - Ray path distribution for several periods related to the cross correlation with SNR larger than 20.

All the phase velocities obtained from the cross-correlations at all station pairs have been averaged. Figure 3.8a displays the average phase velocities from ambient noise data (8 to 35 s) as red line and the average phase velocities calculated using teleseismic data from 20 s to 133 s as black line. The two curves agree well for the common periods from 20 s to 35 s with the most consistent value at 20 s. Figure 3.8b shows the average phase velocity for the all periods that I choose as starting values for the 1-D inversion to get the shear velocity (chapter 4).

Figure 3.9 shows five examples of phase velocity dispersion curves along paths located in different regions of the central Tien Shan. Phase velocities in the Kazakh Shield and Tarim basin are higher than phase velocities in the mountain range. Furthermore, in the Tien Shan mountain range, phase velocities along different paths also show pronounced variations. The path along the strike of the range in the west and central part is characterized by higher velocities at periods above 15 s than the path oriented orthogonally to the range to the south of the Issyk-Kul. The path showing the lowest velocities at the very short periods (8-15 s) is the one sub-parallel to the strike of the range but across the Issky-Kul basin, reflecting the effects of sediments.

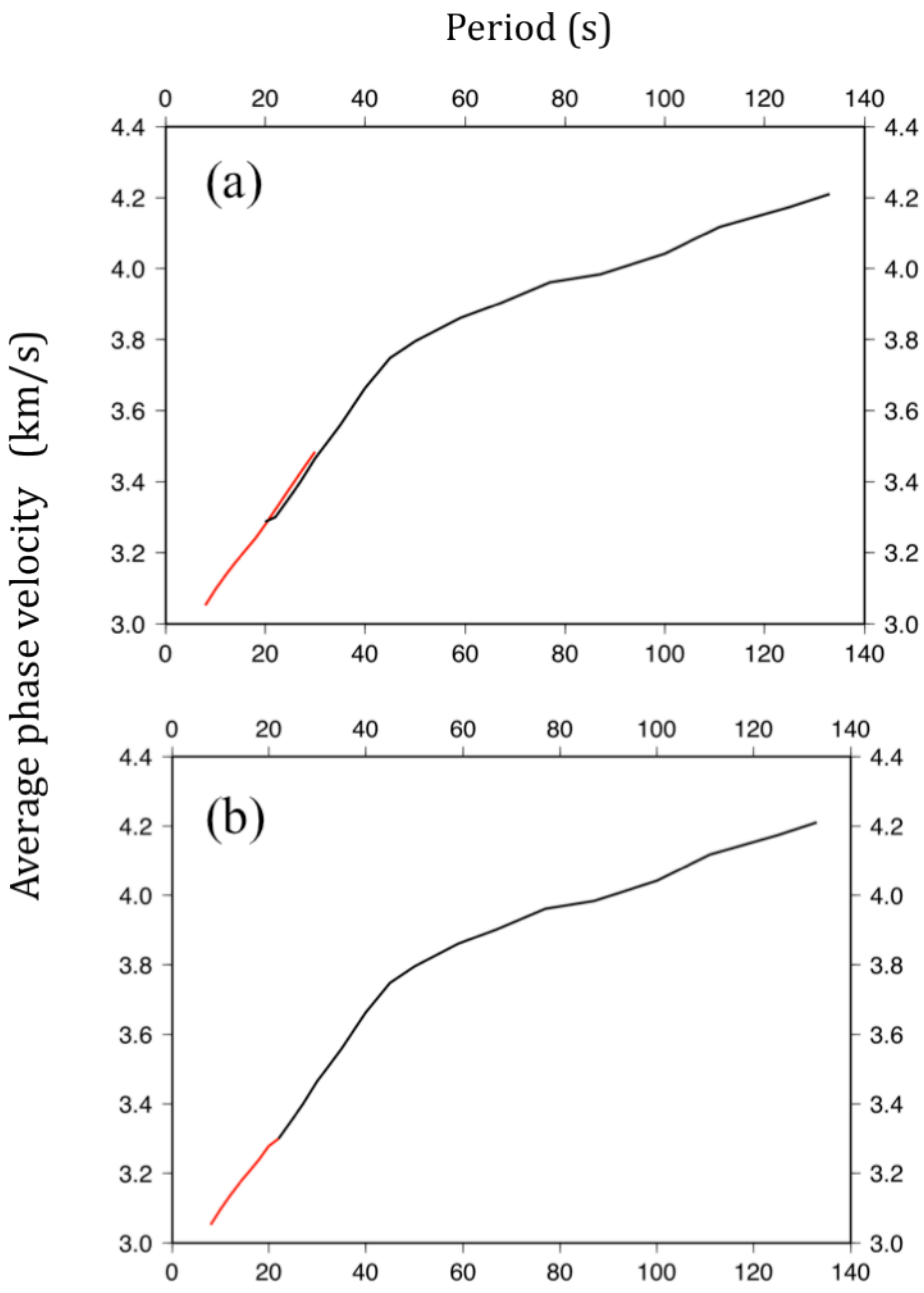

Figure 3.8 - (a) Average phase velocity curve calculated from ambient noise cross-correlations in red and from teleseimic earthquakes in black. **(b)** Average phase velocity curve chosen as initial value for the inversion for the 1D shear velocity model.

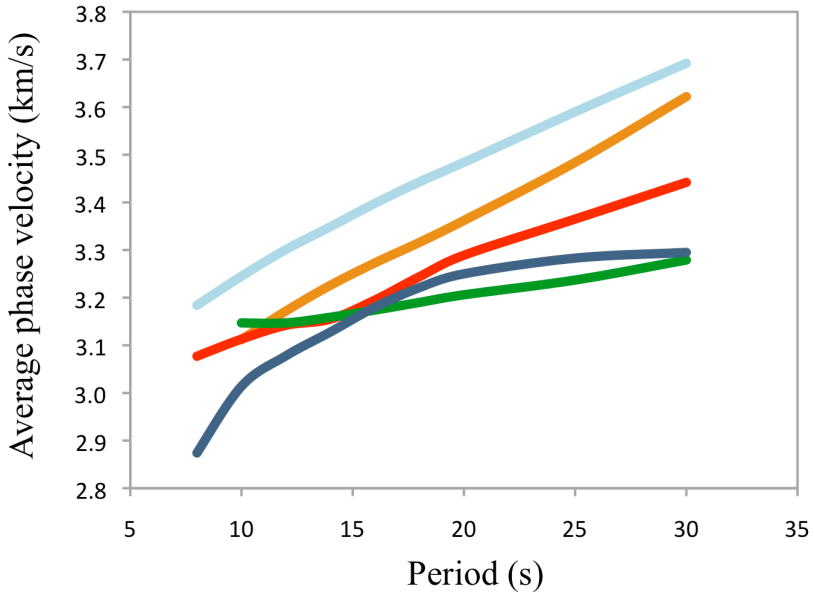

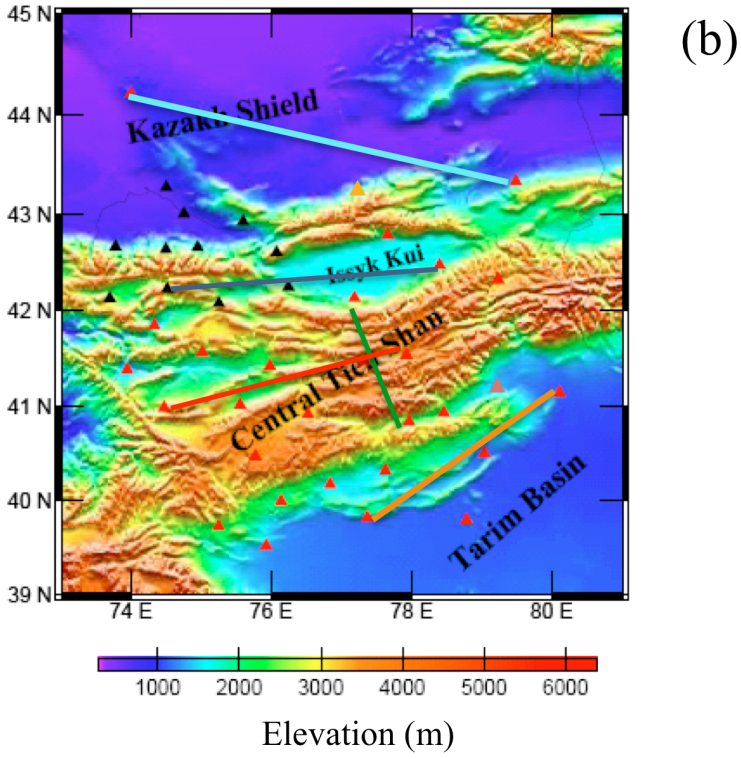

Figure 3.9 - (a) Phase velocity dispersion curves along five paths in different regions of study area. **(b)** A map of central Tien Shan showing the location of the path along which the dispersion measurements plotted in (a) have been measured.

3.3.2 Phase velocity maps

The Rayleigh wave phase velocity measurements obtained from 2 year cross-correlations are mapped on a 1° x 1° spatial grid across the central Tien Shan using the ray theoretic tomographic method of Barmin *et al.* (2001). This method is based on minimizing a penalty functional composed of a linear combination of data misfit, model smoothness and the perturbation to a reference model for isotropic wave speed. After applying the SNR criterion in selecting the data, the number of initial 820 cross-correlations is reduced and the number of chosen signals changes with periods. The final available paths used in the tomography are summarized in table 3.1.

Phase velocity tomography is performed in two steps. The first, preliminary step generates overly smoothed maps at each period in order to identify and reject measurements that present a large travel time residuals. After a further selection based on travel time residual, and also on the three-wavelength criterion, which discards any measurements whose wavelength is greater than 1/3 of the distance between the two stations, final velocity maps can be generated on the second step inversion. The reduction of the number of ray paths after the rejection of bad measurements at every period is shown in figure 3.10. The decrease of the number of ray paths results significant for periods above 20 s and it is not only due to weaker signals at longer period but also due to the three-wavelength criterion.

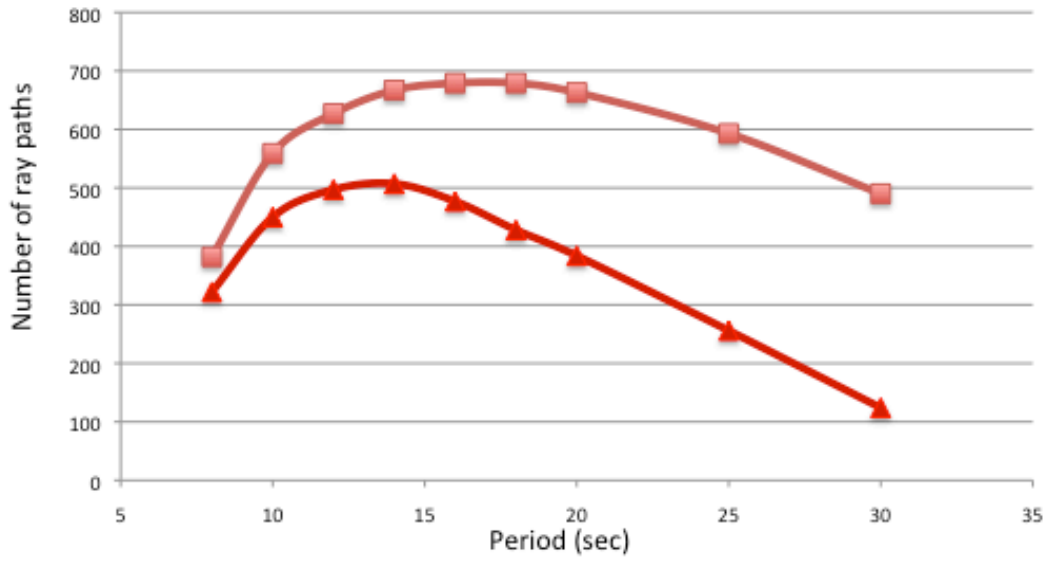

Figure 3.10 – Numbers of ray paths related to cross-correlations with SNR > 20 (orange line) for each analyzed period. In red it is shown the number of ray paths that satisfy also the three wavelength criterion and that show low residuals after the first tomography run.

The results of phase velocity tomography are shown in figure 3.11 where the phase velocity perturbations are defined relatively to the average velocities obtained for the whole region and shown in figure 3.8a as red line. The map contour roughly follows the contour of seismic station distribution as shown in the map at 8 s. Inside this contour the resolution can be considered good, mainly in the more inner part.

The resolution of surface wave tomography depends mainly on the density and azimuthal distribution of paths. Figure 3.12 show that the path density is higher at the center and degrades toward the edge of seismic network and also decreases with increasing period due to the reduction in SNR and for the three-wavelength criterion. The

azimuthal distribution of paths is good in the center of study region at every period until at least 20 s. Above the 20 s the resolution become very poor, due mainly to the three-wavelength criterion.

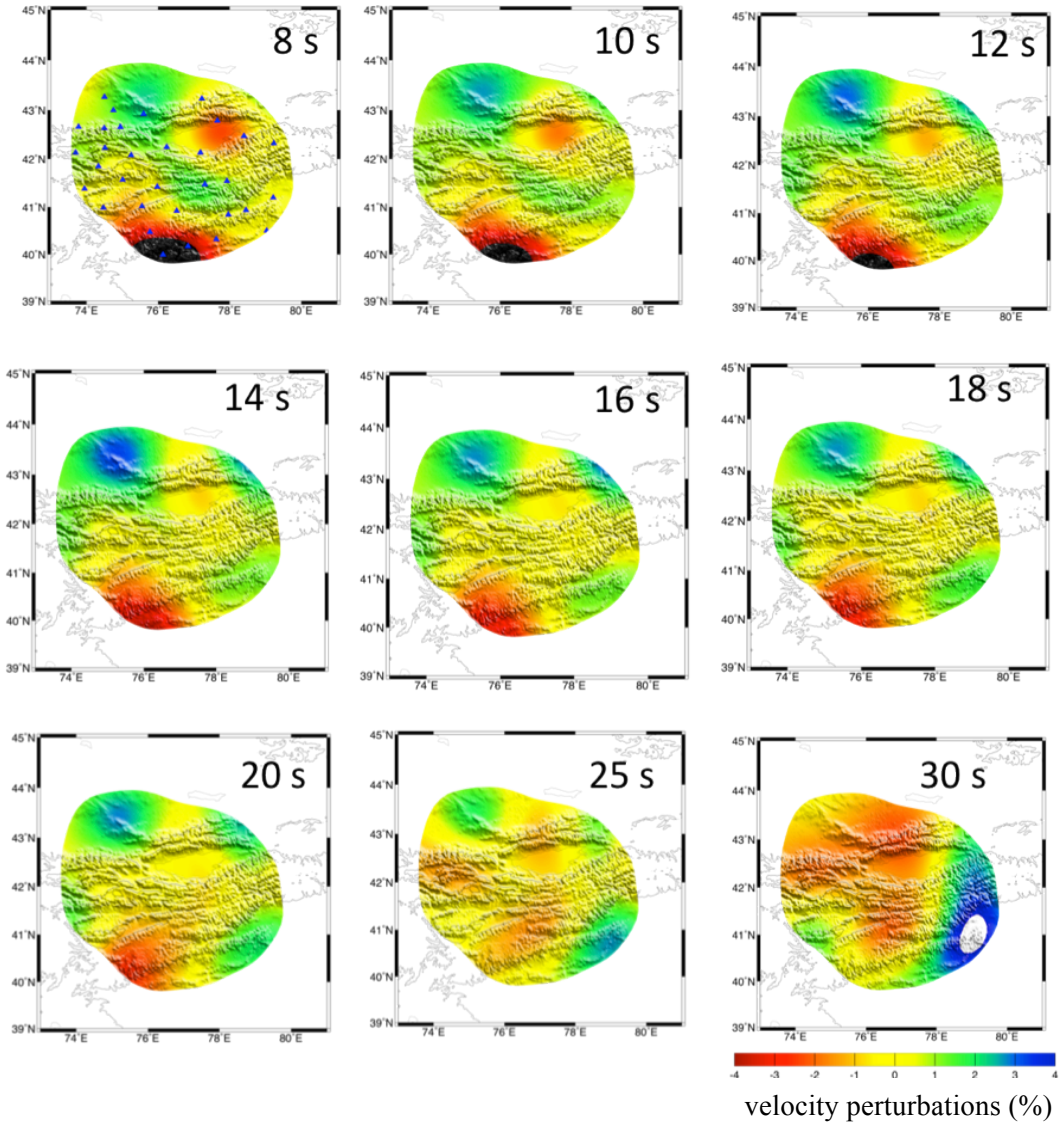

Figure 3.11 - Maps of phase velocity perturbations relative to the average phase velocities in the area.

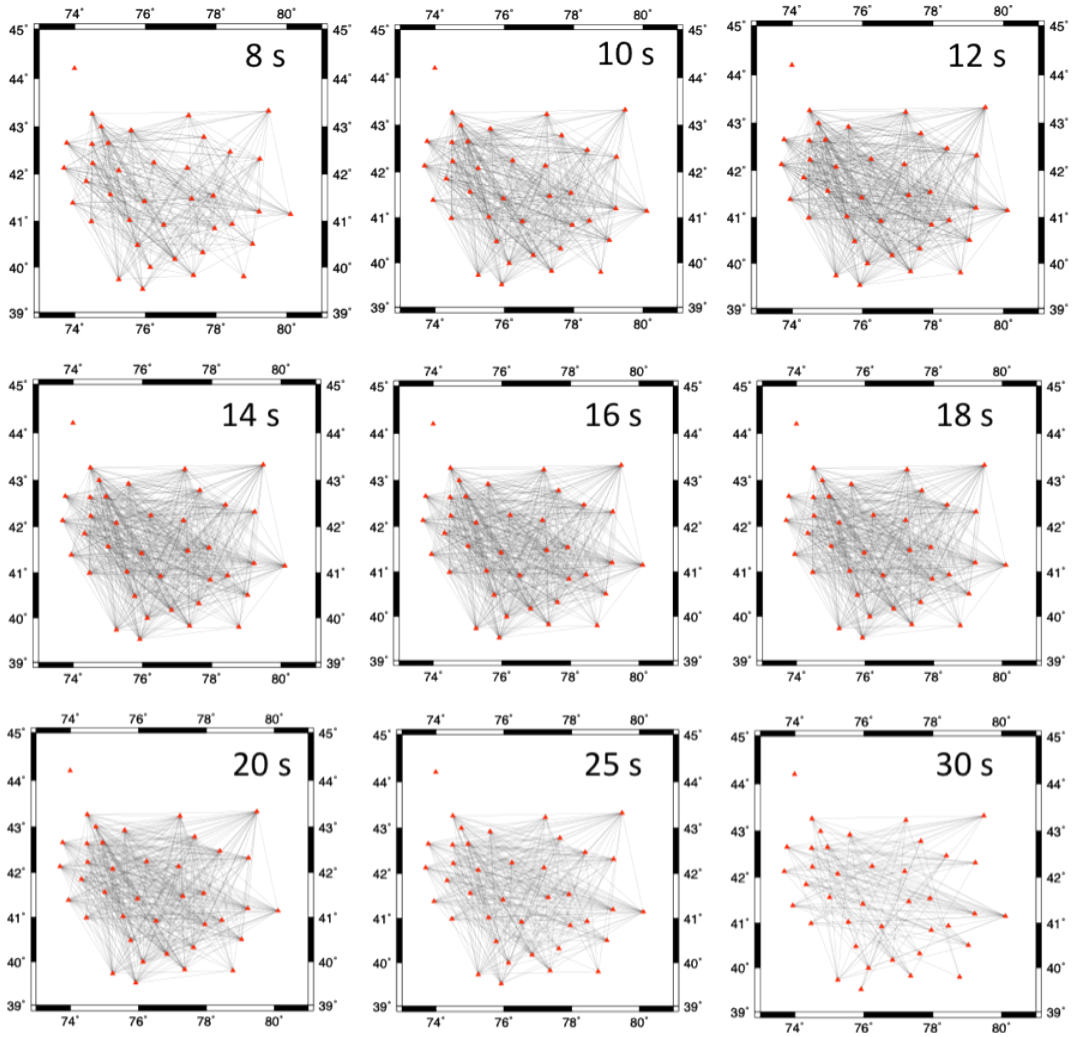

Figure 3.12 - Distribution of ray paths for several periods used for generating the phase velocity maps shown in figure 3.11

The features of the maps vary gradually with period due to the overlap of the depths sampled from Raleigh waves at close frequencies.

One common feature at all the periods between 8 s to 20 s is a low velocity zone located in the southwestern part of the central Tien Shan. The slow anomaly is stronger at the very short period. This zone is coincident with the western boundary between the Tien Shan and the Tarim basin. There can be two possible reasons for the slow anomaly. At the very short periods of 8 to 12 s, the strength of the anomaly is extremely large, which could reflect the thick sediments deposited in the Tarim basin close to the border of Tien Shan. From 14 to 20 s, the slow anomaly might be caused by a relatively thick crust in the area that was mapped from receiver function studies (Vinnik *et al.*, 2004 and 2006). Another low velocity anomaly evident at very short periods from 8 to 12 s is located beneath the Issyk Kul. Since the Issyk Kul area is an intermountain basin, the slow anomaly here is also caused by relatively thick sediment beneath the basin. The central part of the range appears fast at short periods (8-12 s), because of the lack of thick sediments in this segment of range.

Another emerging feature very consistent from 12 s to 25 s is the high velocity zone in the Tarim basin east of 78° longitude indicating a relative cold and strong crust here. A fast anomaly is also found in the southern Kazakh shield to the north of the Tien Shan. Despite relative poor resolution in this area, the large size of the anomaly suggests it is well resolved on average. One reason for this fast zone can be that the old Kazakh crust is typical continental type of crust and is relatively cold compared with the Tien Shan crust

formed by accretion of island continental arcs. Here the resolution is not very good but between 12 s and 18 s there are several ray paths crossing the region.

To check the robustness of the imaged anomalies, I compared Rayleigh phase velocity maps at 20 s, 25 s and 30 s obtained from both cross-correlations of seismic noise and teleseismic earthquakes (Fig. 3.13). From the comparison it is noticeable a general good correlation at 20 s between the two results. At 25 s the correlation between the two methods is still good in the central and southern part of the study area, where the path coverage is still acceptable also if not so good as for 20 s. At 30 s the resolution for ANT is poor, but the slow anomaly in the central part and the fast velocity zone in the southeastern part are almost overlapping. Since the ANT has better resolution at short periods below 20 s, the final phase velocities used to compute 3D shear-wave structure consist of 8-20 s phase velocities from the ANT and 22-135 s from the two-plane-wave inversion.

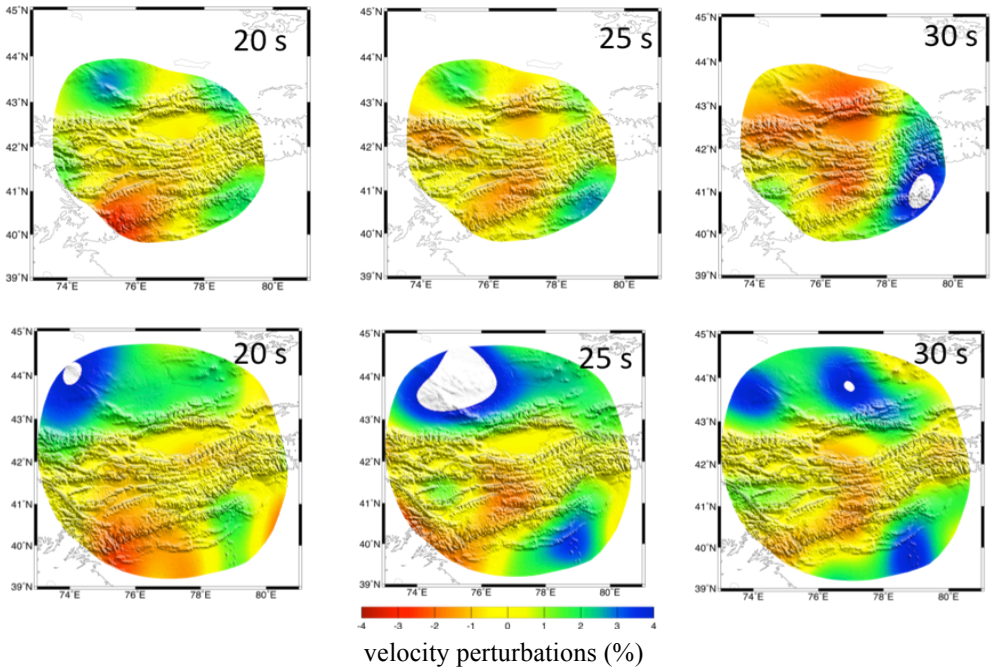

Figure 3.13 - Comparison of phase velocity perturbation maps calculated using ANT tomography (the three maps above) and teleseismic earthquakes (the maps below) at the same periods. Each period is reported on top of the maps.

4 SHEAR-WAVE VELOCITY STRUCTURE

4.1 1-D shear-wave model

Average Rayleigh wave phase dispersions from 6 to 20 s calculated from cross-correlations of ambient noise and from 22 to 125 s from teleseismic earthquakes were inverted to get the 1-D shear-wave structure beneath the central Tien Shan. The model parameters are shear wave velocities in 18 layers and the crustal thickness. This nonlinear inverse problem is linearized and the partial derivatives of phase velocity relative to model parameters are calculated for the initial model using the method of Saito (1988). I modified the global model AK135 (Kennet *et al.*, 1995) with reasonable crustal thickness in the Tien Shan and used the modified model as the starting model. The crust consists of three layers and the initial crustal thickness is 52 km according to the Moho depth variation determined from receiver functions (Vinnik *et al.*, 2006). The velocity model has 15 layers in the mantle from the Moho to 410 km depth. The velocity model beneath 410 km is fixed as the model AK135.

Letting $\mathbf{m_0}$ be a starting model, synthetic data are $\mathbf{d_0} = g(\mathbf{m_0})$. The solution to the general, nonlinear, least squares inversion is given by

$$\Delta m = (G^T C_{nn}^{-1} G + C_{mm}^{-1})^{-1} [G^T C_{nn}^{-1} \Delta d - C_{mm}^{-1} (m - m_0)] \quad (6)$$

where $\mathbf{m}$ is the current model, $\Delta\mathbf{m}$ is the change to the current model, $\Delta\mathbf{d}$ is the difference between the predicted and observed data, $\mathbf{G}$ is the Frechet derivative of the operator g, $\mathbf{C}_{nn}$ is the a *priori* data covariance matrix, and $\mathbf{C}_{mm}$ is the a *priori* model covariance

matrix. Off-diagonal terms are introduced into $\mathbf{C}_{mm}$ to smooth the solution. $\mathbf{C}_{nn}$ is assumed to have only diagonal terms, which are standard errors from the inversions for phase velocities. The inversion also applies penalty for deviation from the initial model $\mathbf{m}_0$. Model parameters that are not well constrained by the data will be close to the starting values.

The 1-D shear-wave model in the central Tien Shan is shown in figure 4.1 along with phase velocities that are used in constraining the 1-D model and the predicted phase velocities from the 1-D model. The upper and lower crust of the Tien Shan is significantly slower than the global reference model. The upper mantle above 200 km is also generally slower than the global model with a low velocity zone imaged from 100 km to 200 km depth. To asses how well shear wave velocities are resolved in the inversion, I plotted five rows of the model resolution matrix that are associated with shear wave velocity at five layers with the median depth at 5, 42, 100, 140, 200 km (Fig. 4.2). A value of 1 indicates the corresponding model parameter is perfectly resolved. In general, the larger the peak value is, the higher resolution of the model parameter. The resolution decreases with depth as indicated from the lower peak values at greater depths. The model resolution matrix shows that shear wave velocity can be well resolved from the surface to a depth of about 200 km.

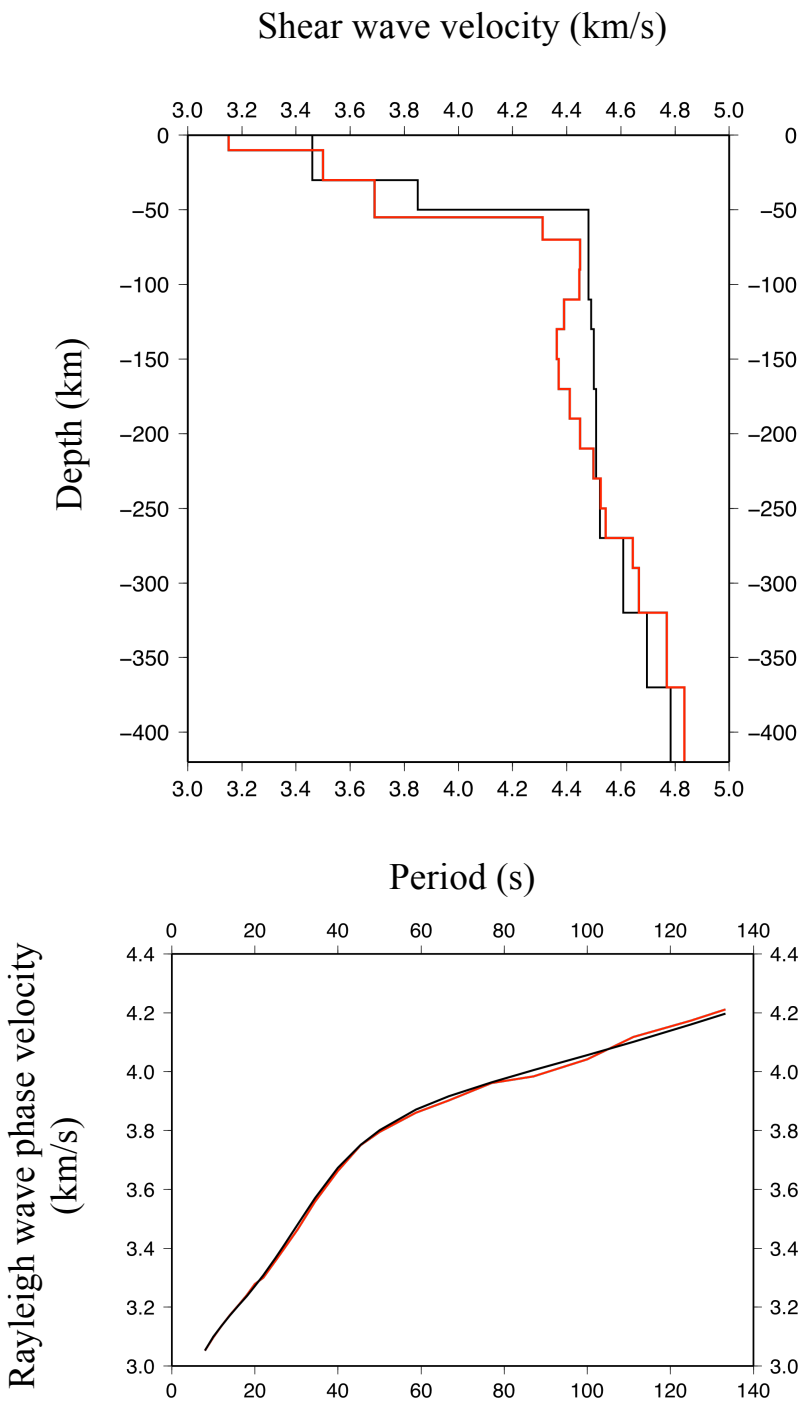

Figure 4.1 – (**a**) 1-D shear-wave models. The red line indicates the best fitting average model for the study area. The black line represents the modified AK135 global model. (**b**) Observed (red line) and predicted (black line) Rayleigh wave phase velocities.

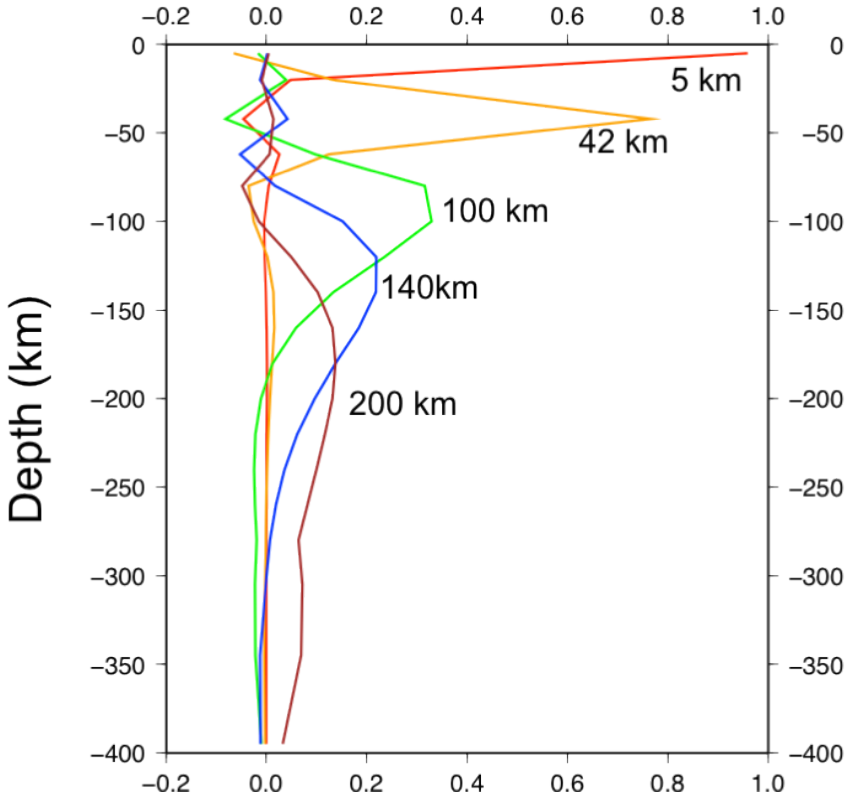

Figure 4.2 – Resolution kernels of shear velocity for the average model in figure 4.1 (a) at 5 layers with median depths at 5, 42, 100, 140, and 200 km.

As shown in equation (1), the *a priori* model covariance matrix plays an important role in smoothing the model and constraining the model towards the initial values. I therefore tried the inversion with several *a priori* standard errors for shear wave velocity (σ=0.03, 0.05, and 0.1 km/s), and the three resulting 1-D models are shown in figure 4.3. Among the three models the one with σ=0.03 km/s shows less fluctuation but has the lowest

resolution (a total rank of 4.97), while the model with σ=0.1 km/s has the highest resolution (a total rank of 6.33) but presents the strongest fluctuation. To compromise model smoothing and resolution, I choose σ=0.05 km/s (a total rank of 5.59) as *a priori* constraint to shear wave velocity in the 1-D and following 3-D inversions.

The Tien Shan range is characterized by a thick crust up to 60 km, but the 1-D phase velocities were calculated for the entire study area where many regions have a thinner crust. I therefore tried inversions using different initial values of 45, 50, 52, 55, and 58 km for crustal thickness. The comparison among the resulting models (Fig. 4.4) reveals that the initial value of crustal thickness affects the velocity in lowest crust (layer 3) and the top part of the mantle (layer 4 and 5) that are immediately above and below the Moho. A thicker crust leads to higher velocity in these layers and a thinner crust to lower velocity. This is because Rayleigh wave at a given frequency is sensitive to velocity in a depth range not at a particular depth. The average velocity in the layers cross the Moho is constrained to more or less a constant by observed phase velocities. These experiments demonstrate a trade off between crustal thickness and velocity near the Moho. The velocity profiles from the initial crustal thickness of 50, 52, and 55km are very similar, indicating that the value of 52 km, which is an average crustal thickness constrained by receiver functions, is a good average for the whole area.

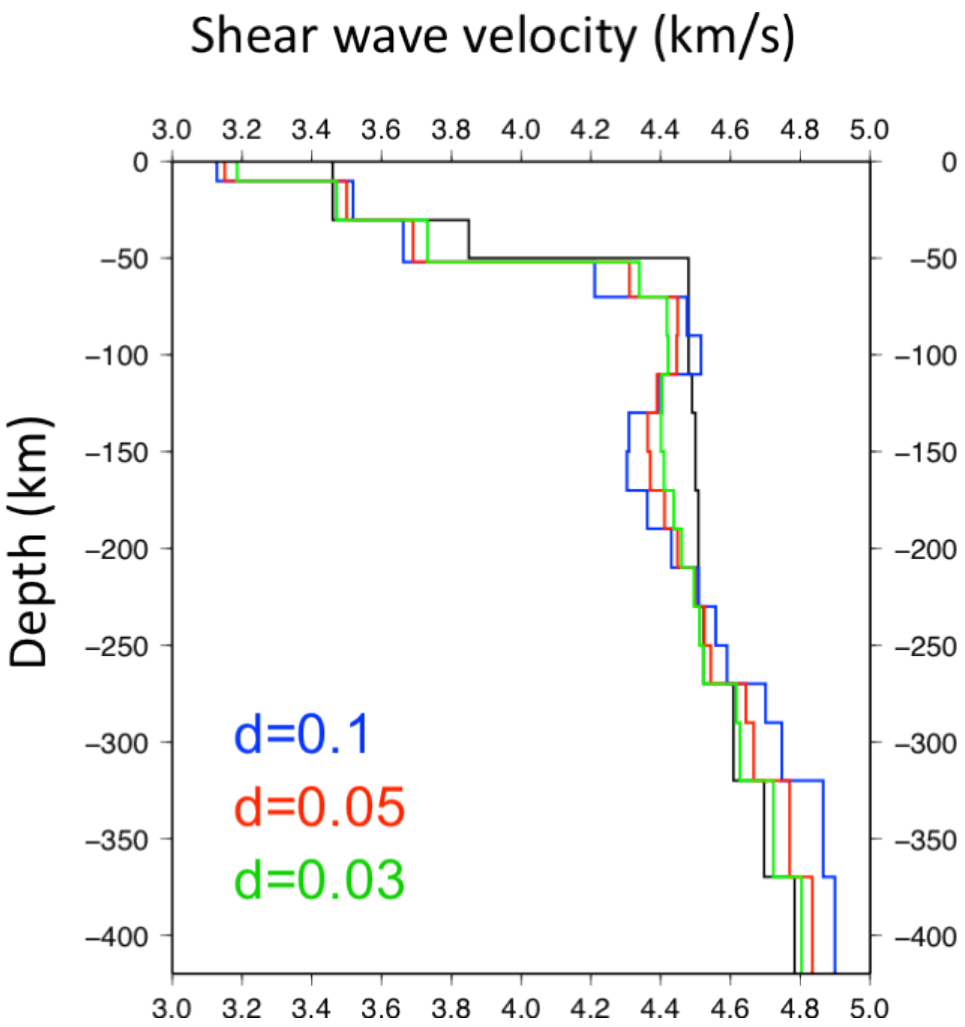

Figure 4.3 - Comparison of three 1-D models calculated using different *a priori* σ for shear wave velocity. The values of σ are reported in the figure and are written in the same colours of the related 1-D model. The black line shows the modified 1-D AK135 model.

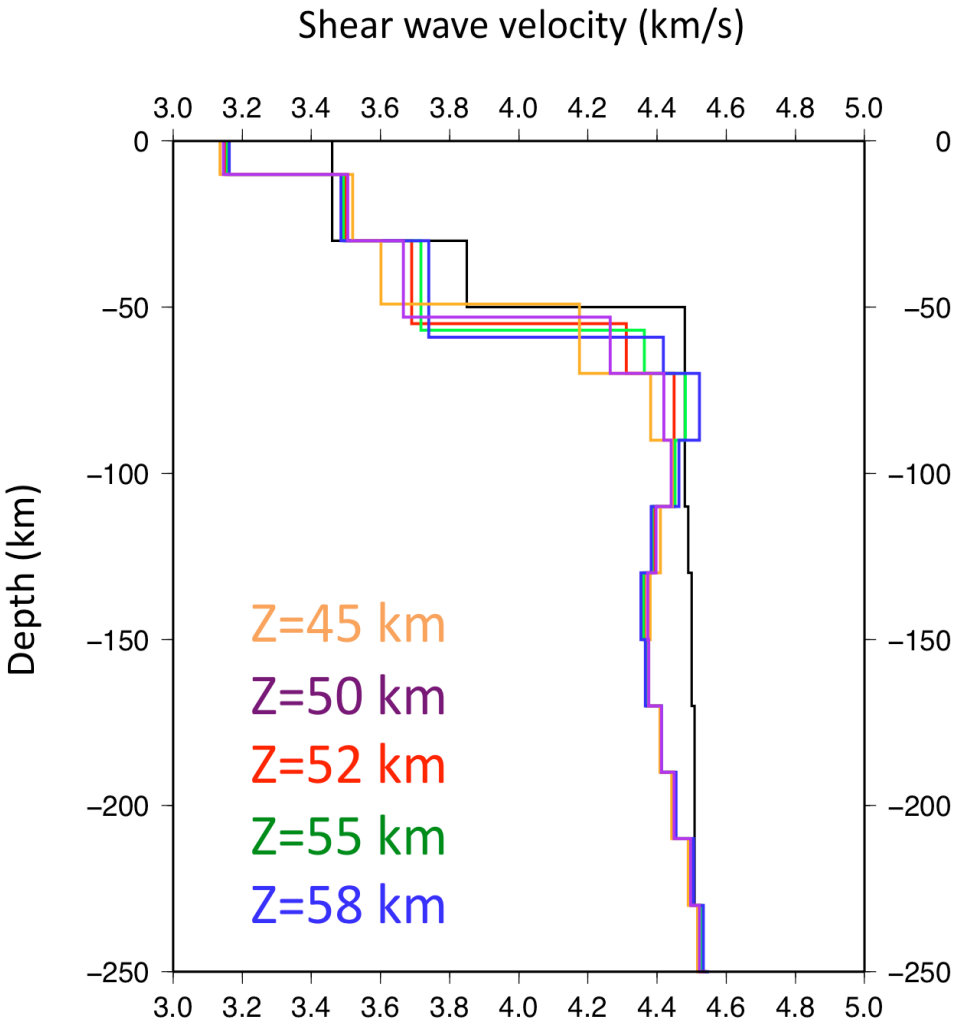

Figure 4.4 – Comparison of three 1-D models calculated using different starting crustal thickness values. The values of the crustal thickness are reported in the figure and are written in the same colours of the related 1-D model. The damping parameter for shear wave velocity is 0.05 km/s for each model. The black line shows the modified 1-D AK135 model.

I also inverted for 1-D shear-wave models in four sub-regions characterized by different tectonic settings including the Kazakh shield, Tarim basin, western Tien Shan range, and eastern Tien Shan range (Fig. 4.5). These models are constrained from average Rayleigh wave phase velocities in each subarea based on the 2-D phase velocity maps. Initial crustal thickness used in the inversions is 45 km for the Kazakh Shield, 50 km for the western Tien Shan, 55 km for the eastern Tien Shan and 58 km for the Tarim basin. The observed and predicted phase velocities agree well in general (Fig. 4.6). However, large variations on the dispersion curves for the eastern Tien Shan and the Tarim basin cannot be well predicted from the smoothing models. The large variations of phase velocities in these two regions could reflect lateral variations that might be due to artifacts at the edge nodes that form the large portion of the areas. The most evident feature is the low velocity in the mantle beneath each region. The upper mantle of the Tarim Basin and the east range are relatively faster than the Kazakh shield and the west range. Another common feature is the low velocity in the upper crust. In addition, the lower crust is slower than the global model except for the Tarim basin. These models indicate lateral variations in the crust and mantle of the central Tien Shan area that can be better viewed from the 3D model below.

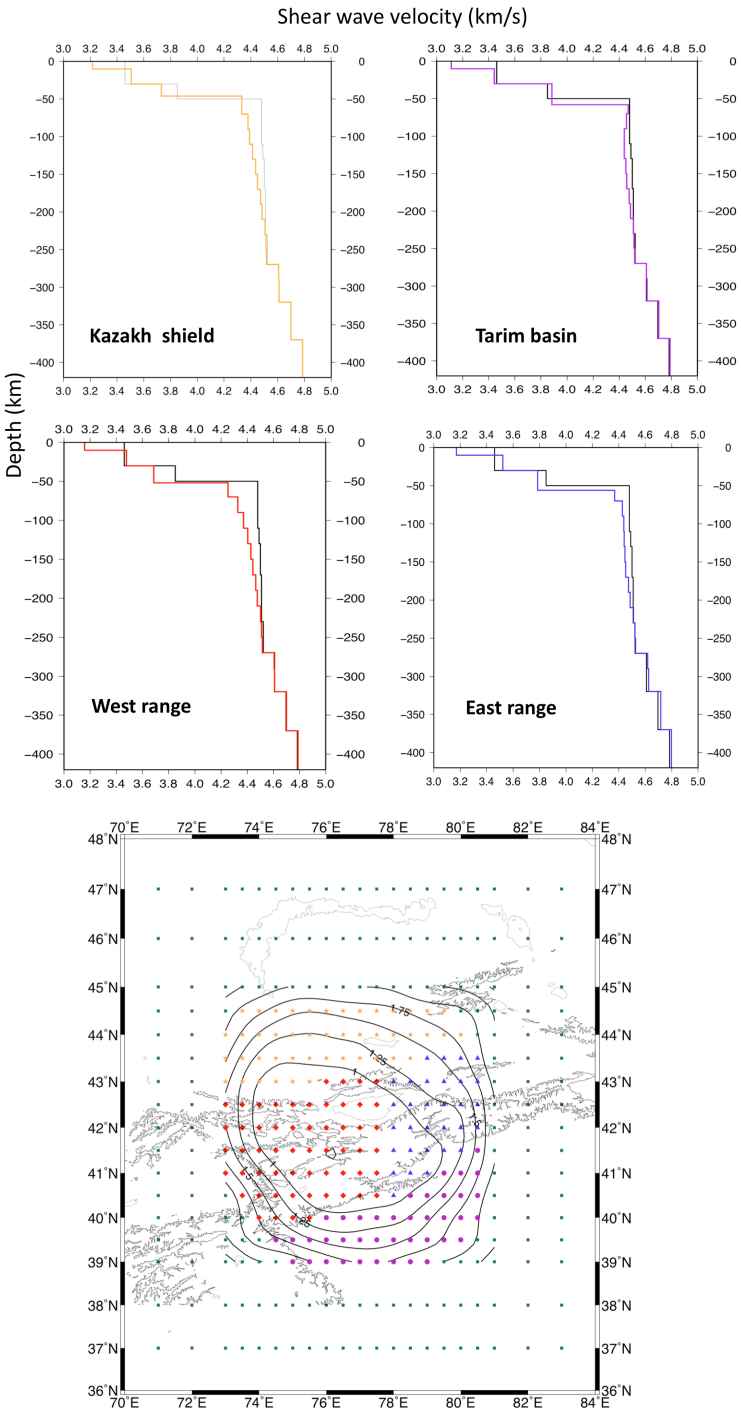

Figure 4.5 – 1-D shear-wave models obtained for the four sub-regions. In the inset map the different coloured grid nodes show the four sub-regions. The black line represents the modified AK135 global model.

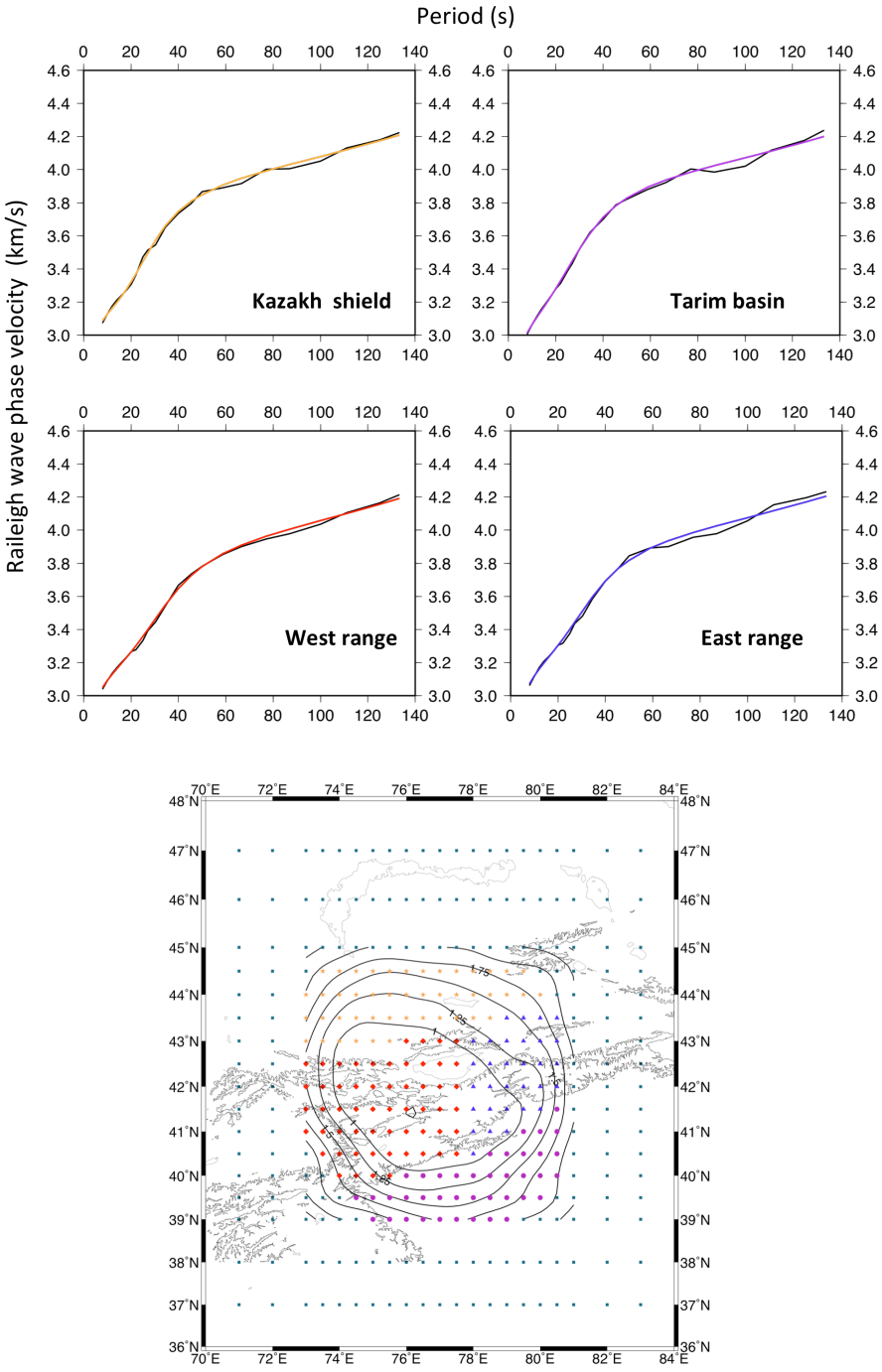

Figure 4.6 – Observed (black lines) and predicted (coloured lines) Rayleigh wave velocities for the four sub-regions. The coloured lines are the predictions from the model plotted in figure 4.5.

4.2 3-D crustal and mantle structure

A 3-D shear-wave model is constructed from the 1-D models obtained at each map point using the same inversion technique. The AK135 global model is used as the starting model instead of the averaged 1-D model because the study area consists of geologically different zones while the average 1-D model is dominantly affected by the central part of the study area, the Tien Shan range. The crustal thickness is solved simultaneously with shear wave velocity in the inversions and its initial value is estimated from the crustal thickness map based on receiver functions (Vinnik *et al.*, 2006). In the inversion I applied a tight constraint to the crustal thickness with σ=1 Km because the starting map from receiver functions was already well determined. Figure 4.7 shows the initial and final crustal thickness map from the inversion. The two maps are very similar as expected. I also tried the inversion with a lower constraint and the resulted map is still close to the initial values, suggesting the Moho values are reasonable in the study area. The thickest crust up to 65 km is beneath the southwest at the boundary between the Tarim basin and the Tien Shan. The Kazakh shield in the north is characterized by relatively thin crust about 40 to 46 km. The crust beneath the majority of the mountain range is about 50 to 60 km thick while the thinnest crust beneath the range is at the Naryn basin in the west.

The velocities perturbations are relative to the average shear wave velocity calculated for each layer within the map area from the 3D model (Fig. 4.8). I choose to use this average instead of the one obtained from the 1-D inversion to emphasize the contrast between the low and high velocity zones. Compared with the 1-D model for the entire area, this 1-D average is smoother and less affected by edge nodes. If I use the 1-D model

as reference velocity the map is overall faster at shallow depths and slower at deeper layers although the anomalies are still in the same positions and are of the same size. 2-D variations of shear wave velocity and perturbations are illustrated in maps (Fig. 4.9) and cross sections (Figs. 4.10, 4.11, and 4.12).

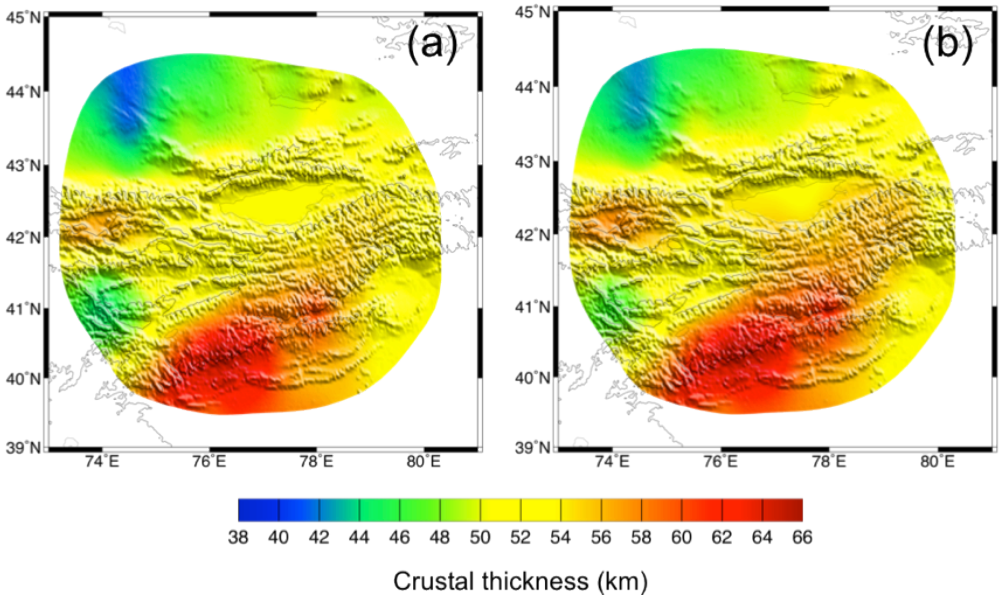

Figure 4.7 - (a) The initial crustal thickness map used in the inversion, extrapolated from (Vinnik *et al.*, 2006). (b) The final map of crustal thickness variation after the 3-D inversion.

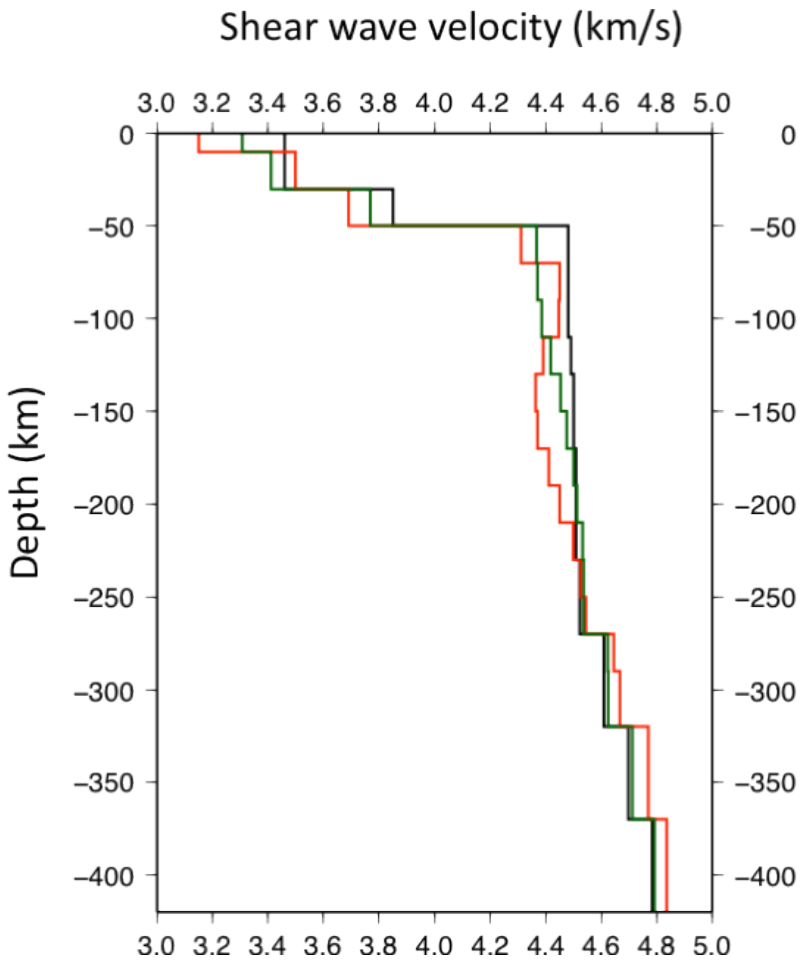

Figure 4.8 – Comparison of the average shear wave velocity obtained after the 3-D inversion (green line) with the 1-D inversion (red line). The 1-D inversion is for the entire study area while the average from the 3D model is for the map area. The black line shows the modified AK135 model as reference.

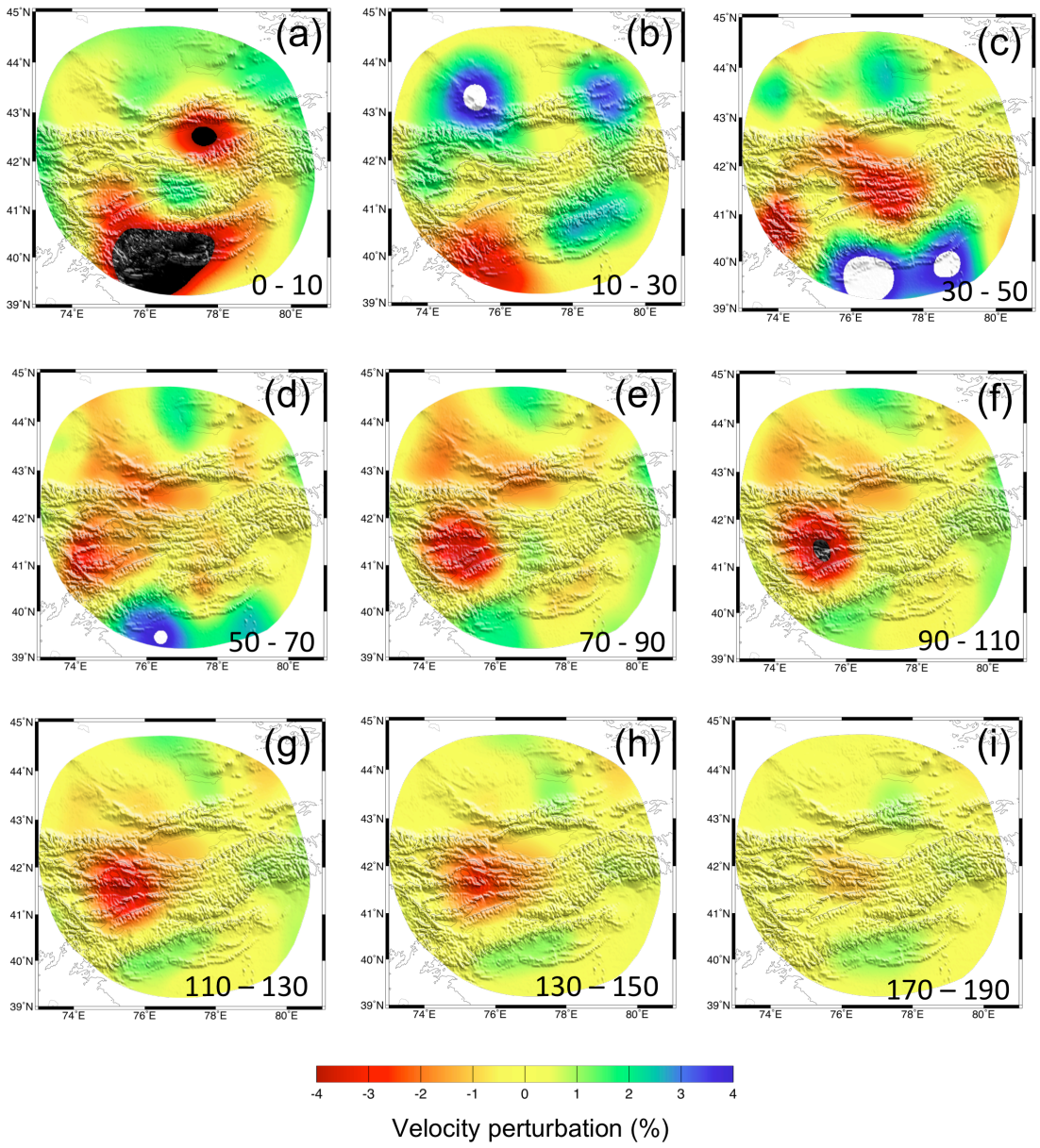

Figure 4.9 – Shear wave velocity variations maps at 9 layers (a to i). The depth interval for each layer is reported on the map with a unit of km. The anomalies are calculated relative to the average shear wave velocity (green line) shown in figure 4.8.

In the shallow crust, two pronounced slow anomalies appear beneath the Issyk Kul the Naryn basin and the southwestern border of the Tien Shan and the Tarim basin (Figs. 4.9, 4.10, and 4.11). These anomalies correlate with the areas characterized by intense sedimentation. The lowest velocity in southwest corresponds to the thickest sediments of 14 km in the area (Steffen, 2011).

In the intermediate crust, high velocity anomalies are imaged along the central southern border of Tien Shan and in the northern part beneath the Kazakh shield. The pattern that a relative slow Tien Shan range sandwiched between higher-velocity lithosphere beneath the Tarim basin in the south and Kazakh shield in the north extends from mid crust to the shallow upper mantle. Such a unique setting of lithosphere contrast is probably the main mechanism for the Tien Shan orogeny.

A strong slow anomaly in the lower crust is imaged in the central part of the Tien Shan across the southern range and the western part of Issyk Kul (Fig. 4.9c). Interestingly, this slow anomaly is underlain by a normal and slightly fast upper mantle (Figs. 4.9, 4.10c, and 4.12c). In the upper mantle, the most remarkable feature is a circular-shape slow anomaly beneath the Naryn basin in the west part. The anomaly extends to at least 150 km with the lowest value at 100 km depth (Figs. 4.9, 4.10 a-b, and 4.12 a-b). Furthermore, slow anomalies are also observed beneath the mountain range in the Kazakh shield from 50 to 130 km and a slow anomaly zone on vertical profiles (Figs. 4.10c and 4.12c) dips southward from the Kazakh shield towards the central Tien Shan range.

Fast anomalies are chiefly imaged beneath the Tarim basin and the Kazakh shield in the mid and lower crust (Figs. 4.9 and 4.10). The fast anomaly at the southern Tien Shan

border extends northward to the boundary of Naryn basin, evident the underthrusting of the Tarim crust. The fast anomaly beneath the Tarim continues to upper mantle to 200 km (Figs 4.10b and 4.10c) but does not penetrate northward under the Tien Shan range, where slow anomalies were observed. It is possible that the subducted Tarim lithosphere was delaminated and the space left was filled by warm asthenosphere that lead to more partial melt revealed as the strong slow anomaly. This can explain the sharp boundary between the fast and slow anomaly under the southwest Tien Shan range (Fig 4.10). The broken Tarim lithosphere is probably better imaged on profile EF (Fig 4.10) where a relative low velocity gap from the Moho to 120 km is between the fast anomaly above and below it. In addition, the mantle beneath the eastern Tien Shan range is relatively fast and the profile across it shows a northward dipping anomaly, which could be the subducted Tarim lithosphere.

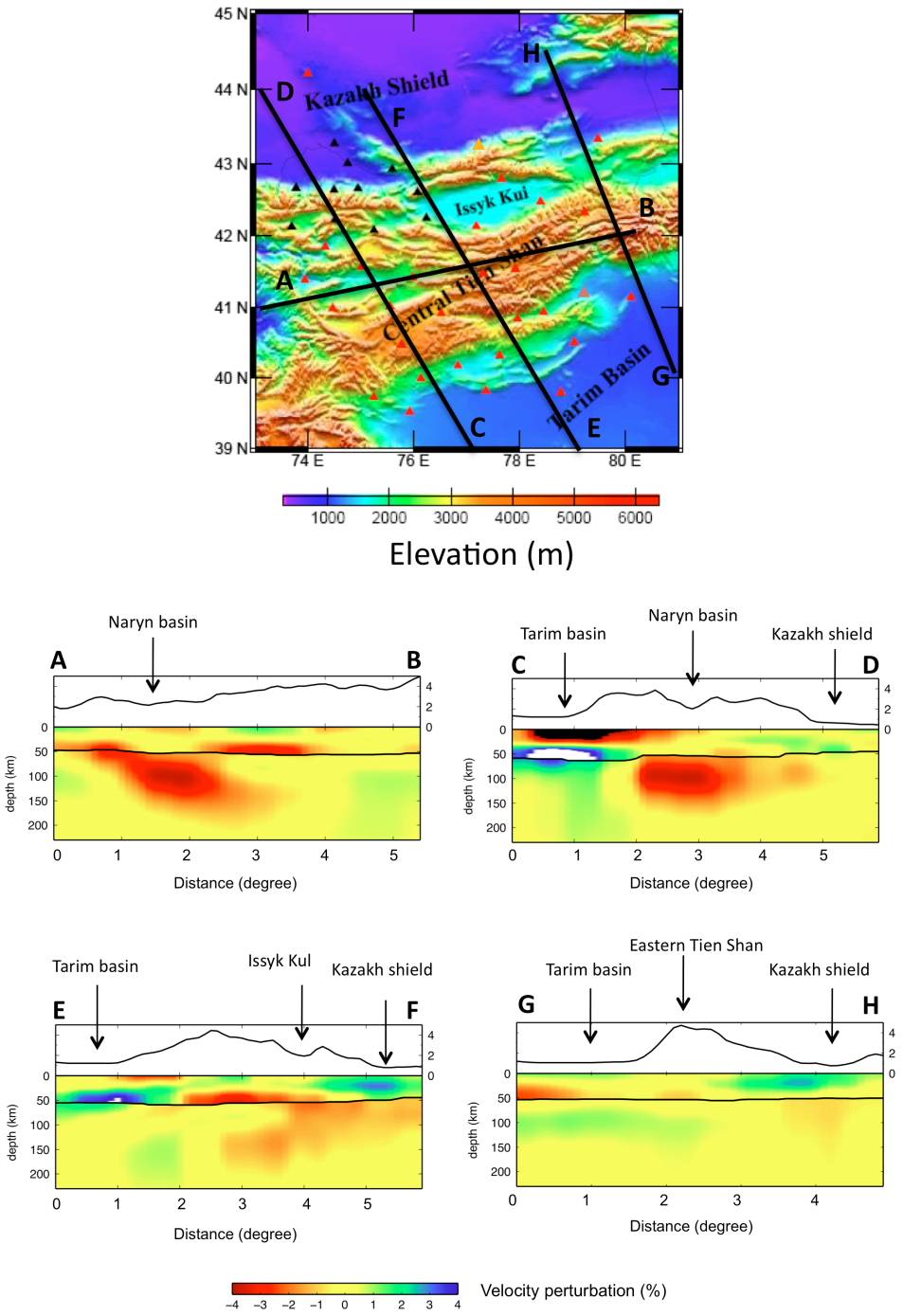

Figure 4.10 - Vertical profiles of shear wave perturbation in the crust and upper mantle. The locations of the four profiles are shown on topography map of the study area at the top. The velocity anomalies are relative to the average shear velocity (green line) shown in figure 4.8. Topography variations along the profiles are superimposed on the velocity sections. The black line in the profile shows the crustal thickness variation.

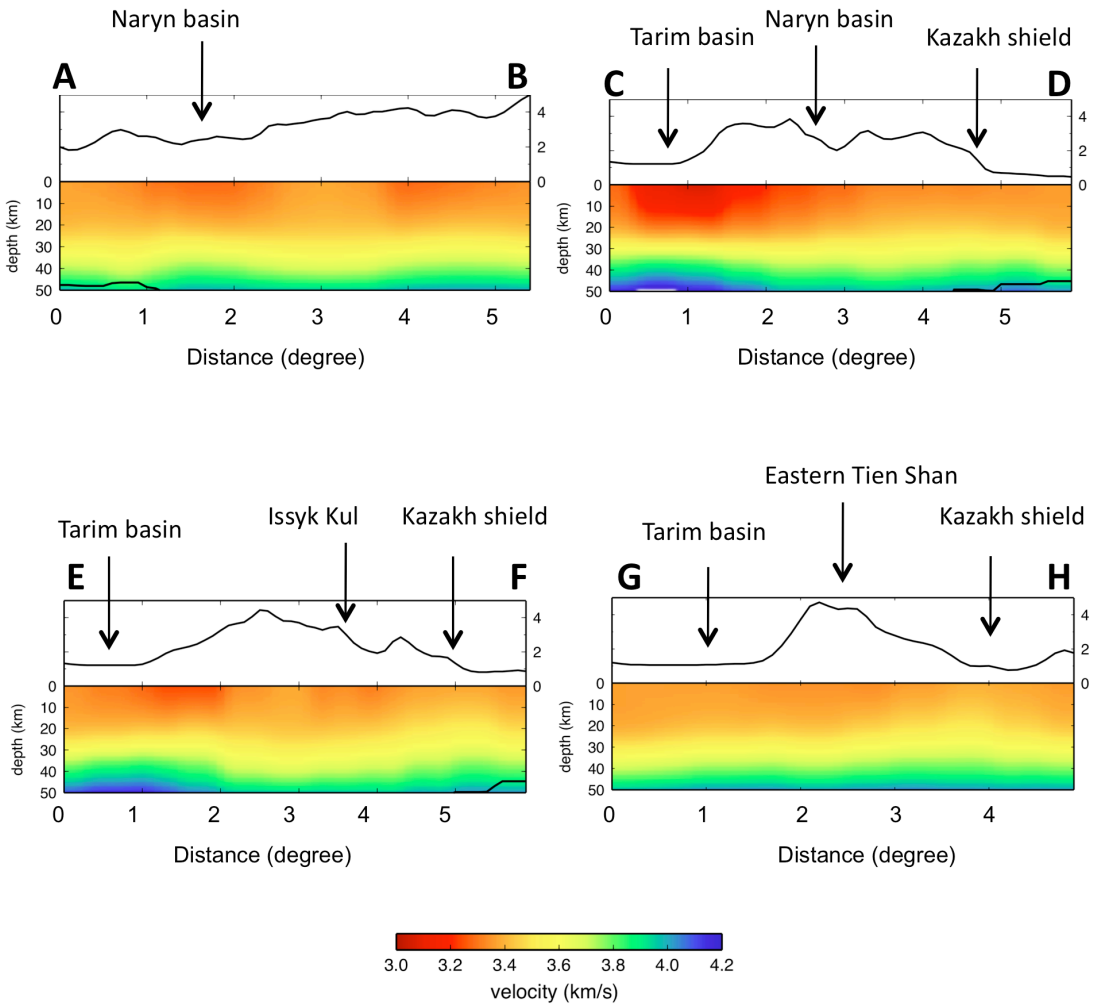

Figure 4.11 - Absolute shear wave velocity in the crust for the four profiles as in figure 10.

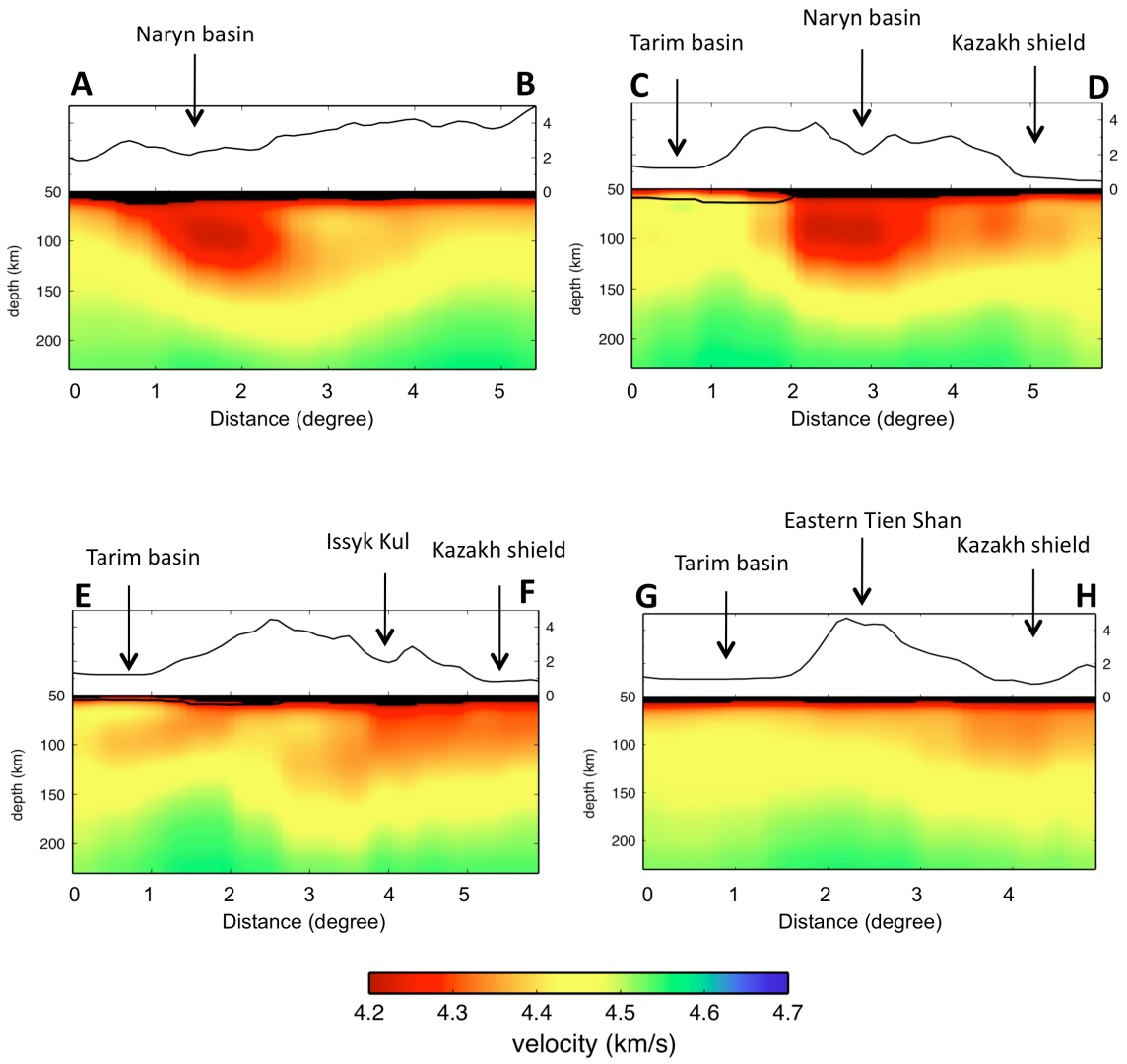

Figure 4.12 - Absolute shear wave velocity in the mantle of the four profiles as in figure 10.

5 DISCUSSION

5.1 Crust

The velocity anomaly distributions in the central Tien Shan show different patterns from the upper to lower crust. The most evident feature imaged on the maps and the cross sections is the strong velocity contrast between the lowest velocity in the first 20 km and the highest velocity in the same region from about 30 km to at least 70 km beneath the southwestern border of the Tien Shan with the Tarim basin. This area is also characterized by the greatest thickness of sedimentary rocks that seems to reach 14 km (Steffen *et al.*, 2011), the highest deformation rate (Reigber, 2001), the highest occurrence of earthquakes (Lei and Zhao, 2007), and the highest crustal thickness (Vinnik *et al.*, 2006).

The very slow anomaly in the shallow crust in southwestern Tien Shan reflects the effects of the thick sediments, while the fast anomaly beneath it indicates the underthrusting of the Tarim basement beneath the Tien Shan. The northern Tarim basement has been stable since Precambrian (Graham *et al.*, 1993; Carroll *et al.*, 1995), and is cold, dry, and fast compared with the Tien Shan lithosphere accreted by continental and island arcs. The underthrusting can also explain the high crustal thickness in this area, which is similar to the observation beneath the Alps where crustal underthrusting is also associated with very high crustal thickness (Schreiber *et al*., 2010). Tarim underthrusting has been proposed by several authors on the basis of both geologic and geophysics

observations (Roecker *et al.*, 1993; Allen *et al.*, 1999; Zhao *et al.*, 2003; and Lei and Zhao, 2007; Kumar *et al.*, 2005; Lei, 2011).

The northern limit of both the slow and fast anomalies, as also of the highest crustal thickness, in the southwestern Tien Shan, is well related to a crustal backstop fault on surface along the southern border of the Naryn basin (Fig. 5.1). The backstop fault has been hypothesized based on geologic evidences and separates the accretionary complex forming the southwestern Tien Shan from the basement of Kazakh continent beneath the Naryn basin (Xiao *et al.*, 2012). Several high-pressure methamorphic rocks have been found along this backstop fault and associated to the paleozoic ocean-arc subduction (Cai *et al.*, 1995). Therefore, this fault could be the trace of the limit of an old subduction zone.

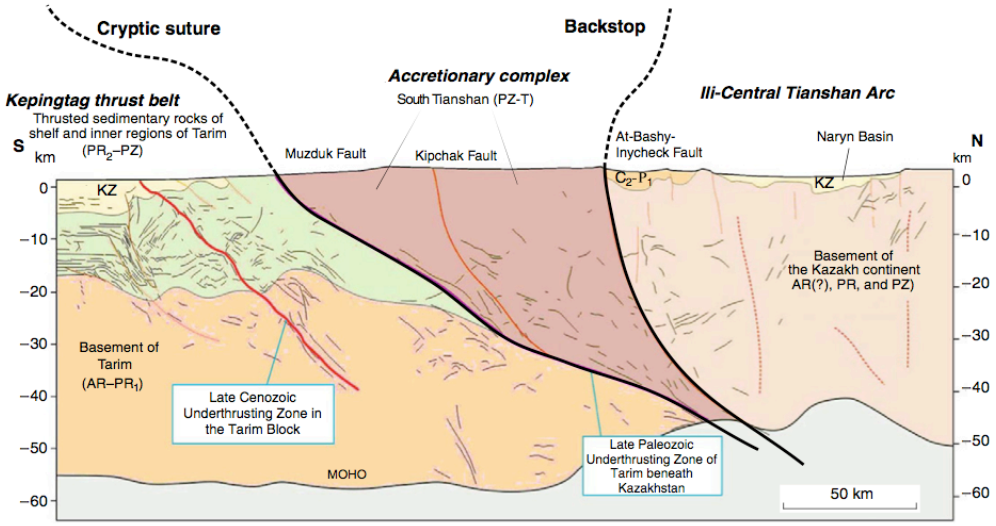

Figure 5.1 – Combined geological and geophysical cross-section showing the tectonic units and zonation of the South Tianshan near the China–Kyrgyzstan border (geophysical section is modified after Makarov *et al.*, 2010). Tectonic interpretation of the South Tianshan accretionary complex is from Xiao *et. al* (2012).

In the top 10 km of the Tien Shan crust, the slow anomalies clearly coincide with the locations of the main basins in the area, such as the Tarim basin, Naryn basin and Yssik Kul. Such correlation suggests that these slow anomalies are mainly caused by sediments in the basins. In addition, the slower anomalies correlate with the higher sediments thickness. The lowest velocity anomaly in the southwest Tien Shan corresponds to the thickest sediments of 14 km (Steffen, 2011). This anomaly also extends to the intermediate crust due to the extreme sediments thickness. At intermediate and lower crust, high velocity anomalies appear to the southern border of Tien Shan in the Tarim basin and to its north in the Kazakh shield. In the northern part very old rocks, from Vendian to early Paleozoic, have been found in outcrops (Xiao *et al.*, 2012) close to rocks of volcanic arc formed in late Paleozoic time, suggesting the fast anomaly is probably related to old, mafic rocks. The fast anomaly in the southern border of Tien Shan and the northern Tarim basin is the old and cold Tarim lithosphere. In the western part, the fast anomaly extends more northward and deeper (to 70 km), indicating the underthrusting of Tarim lithosphere. The anomaly in the central part is confined at a shallow depth of about 50 km.

A strong slow anomaly is imaged at the lower crust in the central part of the range, coincides with the central Tien Shan Paleozoic volcanic arc and relative thick crust along the range. The slow anomaly is probably originated from compositional variation such as high volatile or water content related to the old volcanic arc activity. Or it might be due to relative temperature increase to the crustal rock related to crust shortening and thickening process. Such a slow lower crust is likely weak and therefore deforms easily to accommodate the compression from the Tarim block. A weak and easily deformed central

Tien Shan crust also explains the absence of the Tarim underthrusting in this region because the stress at the border of the central Tien Shan and Tarim cannot hold high enough for the subduction to develop.

No low velocity anomaly is observed beneath the Naryn basin and beneath the Issyk-kul, suggesting relative strong crust in these places. The Naryn basin is on the Kazakh continental block, which is old and rigid; and the Issyk-Kul micro-continent also has a rigid basement, which had been a homogeneous structure during a long time period (Buslov et. al, 2003). In addition, Eartquakes of M>6 clearly mark the northern and southern margins of the lens-shaped Issyk-Kul micro-continent, indicating that old crustal heterogeneity control the recent tectonics of the northern Tien Shan structures.

5.2 Mantle

5.2.1 Lithosphere delamination

The most evident feature in the mantle is represented by a large slow anomaly beneath the whole western Tien Shan, well defined between 70 and at least 150 km depth. This anomaly is at the maximum strength at 100 km depth while its intensity decreases with depth and appears slightly shifted towards the Yssyk Kul at northeast beneath 100 km. Such a circular-shape slow anomaly could be due to high temperature and/or partial melt associated with asthenospheric mantle upwelling, which could happen after a lithospheric root or the subducted Tarim lithosphere is removed. Furthermore, Chen *et al.* (1997) and Tian *et al.* (2010) observed an elevated 410 km discontinuity beneath the Tien Shan and considered it as evidence for the detached root.

Beneath a range like Tien Shan the distributed shortening in the crust should be accompanied by a similar shortening in the lithosphere as predicted from the strike-normal model (Fleitout and Froidevaux, 1982; England and Houseman, 1986) with consequent formation of a lithospheric root. This thickened lithosphere becomes gravitationally unstable, and eventually detaches from the lower crust, and sinks into the underlying mantle. The space left in the upper mantle is then replaced by an influx of hot asthenosphere causing uplift of the crust and volcanism (England and Houseman, 1989). This model of lithospheric delamination has been introduced to explain the absence of a thick mantle lid beneath elevated plateaus (Bird, 1979; and Houseman *et al.*, 1981) and rapid uplift and mafic magmatism often accompanying the late stage of the orogenic process (Kay and Kay, 1993). Although lithospheric detachment has been proposed in many locations (the Himalayas, Andes, Alps, the Basin and Range province of the Western United States, the European Variscides), geophysical observations of the process are very few (Kosarev *et al.*, 1999 and Boyd *et al.*, 2004). This may be due to its ephemeral nature: numerical modeling indicates that the lithosphere root detaching is a catastrophic event and lasts only a few million years (Houseman *et al.*, 1981 and Schott and Schmeling, 1998).

In contrast to the slow anomaly beneath the western part of the Tien Shan range, a high velocity anomaly is imaged in the eastern part of the Tien Shan at the same depth range of 70 to 150 km (Fig 4.10). The variation of mantle velocity along the Tien Shan range is probably evident different stages of the mountain belt development.

In the western part, where the subduction start earlier and the mountain chain is wider, the lithosphere root was formed earlier and the stage of the lithosphere delamination has

already been reached; while in the eastern part the subduction is still in the early stage and the lithospheric root is still present. Further east to the Chinese Tien Shan range, Li *et al.* (2007) analysed receiver functions and found out that a clear mountain root does not exist and the crust-mantle boundary has a transitional structure, indicating that the differentiation between the crust and the mantle is not accomplished and that the orogenic process is still going on. It is possible that different segments of the Tien Shan range are experiencing different stages of mountain formation and development.

Alternatively, the delamination could happen to the subducted Tarim lithosphere slab instead of a thick lithospheric root. Along the profile CD in figure 4.10, the fast anomaly in the south is truncated sharply and extends vertically down to 200 km. It is hard to image how the subducted Tarim lithosphere can bend down with a right angle. This vertically extension of the fast anomaly could be caused by cold mantle downwelling in contrast to the upwelling beneath the Naryn basin. Along the profile GH in figure 4.10, a fast anomaly from 70 to 150 km extends horizontally and deepens slightly from the Tarim basin to the Tien Shan, which could be the subducted Tarim lithosphere. In this case, the velocity image reflects the different stage of the Tarim subduction along the Tien Shan range.

Many previous studies with different approaches supported the tectonic model of the Tarim and the Kazakh lithosphere underthrusting beneath the Tien Shan (Roecker et a., 1993, Ghose *et al.*, 1998, Xu *et al.*, 2002, Yang *et al.*, 2003, Lei and Zhao, 2007). The results from this study provide more details on the subduction of the Tarim lithosphere,

which is probably delaminated in the western central Tien Shan but still present in the eastern part. However, no fast anomaly is imaged beneath the northern part of the central Tien Shan. Instead, a slow anomaly is imaged beneath the mountain chain that extends through the Kazakh shield between about 50 km and 110 km, which could be compositional anomaly associated with the accretionary island arcs.

5.2.2 Mantle compositional anomaly

Although the large slow anomaly in the upper mantle beneath the western part of the central Tien Shan could be explained by the consequence of the lithosphere delamination, it might be also related to or partially contributed by a local mantle compositional anomaly such as high water or volatile content that was produced during the subduction of young oceanic lithosphere at the Paleozoic age. Anomalously low velocity and high attenuation have often been attributed to partial melting. But much of the effects of high water content are similar to those due to the presence of partial melting. Addition of water enhances anelasticity and reduces seismic wave velocities. Both seismic wave attenuation and velocities of olivine are sensitive to water content (Karato, 2003). Experimental studies under high pressures and analyses of naturally occurring minerals have established that a significant amount of water can be dissolved in anhydrous minerals such as olivine (Bell and Rossman, 1992; Ingrin and Skogby, 2000; Williams and Hemley, 2001).

In subduction zones, the regions of high water content in the shallow upper mantle (200 km) are localized beneath active or recent volcanoes (Karato, 2003). In addition, ocean

island basalts contain higher than normal water content. in fact, the low velocity zone in the upper mantle is predominantly an oceanic feature (Fig. 5.2 from Lebdev and Nolet, 2003). Low velocities characterizing the uppermost mantle in the fore-arc and are likely associated with serpentinization of fore-arc mantle due to the large volumes of water released from subducted oceanic crust and sediments (Hyndman and Peacock, 2003). Serpentinite is a hydrated form of peridotite and is known to exhibit lower seismic velocities than peridotite. At the same depth the shear wave velocity of serpentinite might be 2.38-2.41 km/s while velocities for peridotite might range from 4.46 to 4.68 km/s (Christensen, 1996). Geophysical observations suggest fore-arc mantle may commonly be about 20% serpentinized. Serpentinized mantle peridotite has been found on the northern margin of Tarim Craton (Li and Cui, 1994; Shu *et al.*, 2004)

At the depth of 100 km the basalt of the oceanic slab is converted to a denser metamorphic rock called eclogite. During the transition from basalt to eclogite, these hydrous materials break down, producing copious quantities of water, which at such great pressure and temperature exists as a supercritical fluid. The supercritical water, which is hot and more buoyant than the surrounding rock, rises into the overlying mantle where it lowers the melting temperature of the mantle rock and produce partial melting. Both partial melt and water help to lower the seismic velocity of the rock.

In the upper mantle, the large slow anomaly beneath the Naryn basin in the west part and the smaller slow anomalies beneath the mountain range in the Kazakh platform are similar to the slow anomaly imaged above the subducted Pacific slab under Japan (Zhao *et al.*, 1992), probably related to high content of water released during the subduction of the Kazakh lithosphere. This is not a surprise because the Tien Shan was formed by

accretion of a series of Paleozoic island arcs after closing two ancient oceans in the north and south (Xiao *et al.*, 2012). The location of the slow mantle anomaly beneath the Naryn basin is under a relative rigid crust that is belong to the stable Kazakh continental platform. The strong crust may act as a rigid lid that helped to prevent water or other light elements from migrating to shallow depth and keep that the high water content in the mantle, which leads to low seismic velocity. A similar scenario happened in the mountain range in the Kazakh shield, where a fast crust is above a slow mantle.

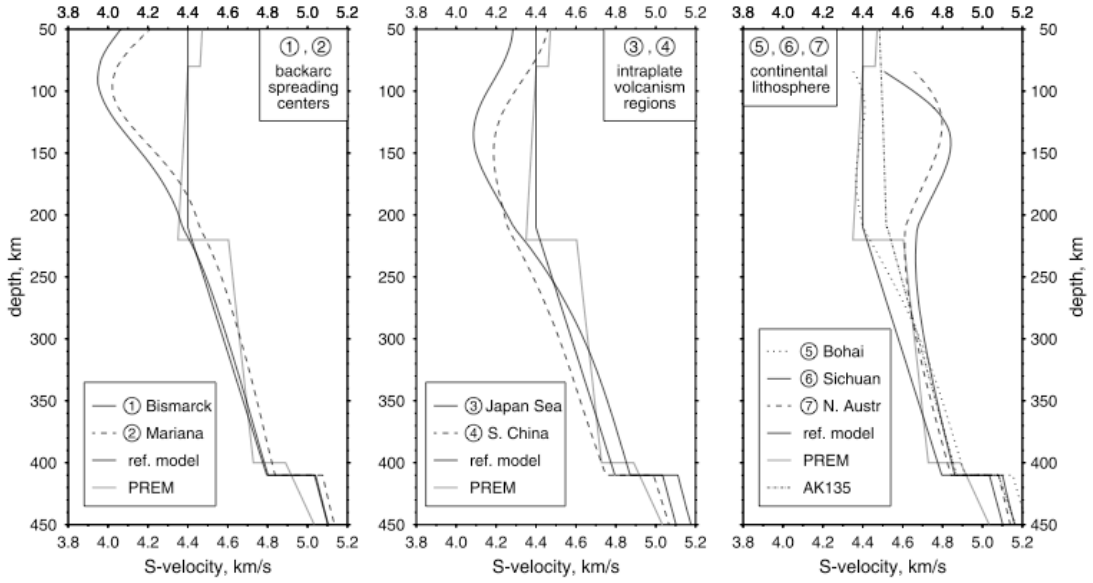

Figure 5.2 - 1-D S wave velocity profiles at different regions from the 3-D model by *Lebedev and Nolet* (2003): (left) the active spreading centers in the Bismarck (1) and Mariana (2) back-arc basin; (middle) Circum Sea of Japan (3) and south China region of intraplate basaltic volcanism; and (right) eastern Sino-Korean (5), Yangtze, and north Australian (7) cratons.

6 CONCLUSIONS

Rayleigh waves from ambient noise data and teleseismic events recorded at the CHENGIS and KENT stations were used to develop a 3-D shear wave velocity model beneath the central Tien Shan. Ambient noise tomography was used to resolve phase velocity variations from 8 to 35 s; and the two-plane-wave inversion technique was applied to teleseismic data for phase velocities from 20 to 133 s. Combining phase velocities from both methods improves the model resolution in the crust and mantle. This model has a lateral resolution of 50-70 km and a good vertical resolution from surface to 200 km depth.

In the shallow crust, slow velocities correlate with sediments in the Naryn basin, the Yssik Kul, and the southwest border of the central Tien Shan with the Tarim basin. The lower crust in middle of the central Tien Shan range is extremely slow, which is probably mechanically weak and easy to deform. In contrast, the mid-lower crust is imaged as fast anomaly in the northern Tarim and southern Kazakh shield that border the Tien Shan, indicating the crust there is cold and strong. This observation of velocity contrast between the Tien Shan and the Tarim crust provides evidence for the hypothesis that the Tien Shan is formed due to a strong Tarim lithosphere that is able to transfer stress from the India-Asia collision and a weak Tien Shan lithosphere that is easy to deform. In addition, the fast Tarim lithosphere extends northward into the southwest central Tien Shan and stops at the southern boundary of the Naryn basin, which is on the Kazakh continental platform and therefore probably strong enough to stop northern penetration of the Tarim underthrusting.

In the upper mantle the most interesting features are a large slow anomaly beneath the western part of central Tien Shan from 70 km to 150 km and a relative higher velocity at the same depth in the eastern part, indicating different dynamic processes along the range. The slow anomaly could be interpreted as hot temperature and partial melt due to asthenospheric upwelling as a consequence of a lithospheric root detachment or subducted Tarim lithosphere delamination. Alternatively, the slow anomaly could reflect a local mantle compositional anomaly due to high water or volatile content that was produced during the subduction of young oceanic lithosphere at the Paleozoic age. The fast anomaly in the eastern part continues from the Tarim to the Tien Shan and deepens slightly under the range. This fast anomaly could be the subducted Tarim lithosphere or the part under the Tien Shan could be a thickened lithospheric root, which is also possible considering a relative thick crust above. These observations and interpretations imply different mountain formation stages in the west and east of the central Tien Shan. In the western central Tien Shan, the subducted Tarim lithosphere or a thick Tien Shan lithosphere root was removed and the left space was filled by hot asthenosphere; while in the eastern part the subducted Tarim lithosphere or a thick Tien Shan lithosphere root is still present.

The new model from this study is clearly evident that the central Tien Shan lithosphere is not only different from the Tarim and Kazakh shields from south to north but also complex along the range in east-west direction. The dynamic process under the central Tien Shan is more complicated than suggested in previous models. Future geodynamic modeling including seismic constraints will help to improve understanding on the formation mechanism of the Tien Shan range.

7 REFERENCES

Abdrakhmatov, K.Ye., Aldazhanov, S.A., Hager, B.H., Hamburger, M.W., Herring, T.A., Kalabaev, K.B., Makarov, V.I., Molnar, P., Panasyuk, S.V., Prilepin, M.T., Reilinger, R.E., Sadybakasov, I.S., Souter, B.J., Trapeznikov, Yu.A., Tsurkov, V.Ye., and Zubovich, A.V., 1996. Relatively recent construction of the Tien Shan inferred from GPS measurements of present-day crustal deformation rates, *Nature, 384*, 450-453.

Allen, M.B., Windle, B.F., and Zhang, C., 1992. Paleozoic collisional tectonics and magmatism of the Chinese Tien Shan, central Asia, *Tectonophysics*, *220*, 89-115.

Allen, M.B, Vincent, S.J, and Wheeler, P.J., 1999. Late Cenozoic tectonics of the Kepingtagethrust zone: Interactions of the Tien Shan and Tarim Basin, northwest China, *Tectonics, 18*, 4, 639-654.

Avouac, J.P., Tapponier, P., Bai, M., You, H., and Wang, G., 1993. Active thrusting and folding along the northern Tien Shan, and Late Cenozoic rotation of the Tarim relative to Dzungaria and Kazakhstan, *J. Geophys. Res*., *98*, 6755-6804.

Bagdassarov, N., Batalev, V., and Egorova, V., 2011. State of lithosphere beneath Tien Shan from petrology and electrical conductivity of xenoliths, *J. Geophys. Res*., *116*, *B01202*, doi:10.1029/2009JB007125.

Barmin, M.P., Ritzwoller, M.H., and Levshin, A.L., 2001. A fast and reliable method for surface wave tomography, *Pure Appl. Geophys., 158(8*), 1351–1375.

Bazhenov, M.L., 1993. Cretaceous paleomagnetism of the Fargana Basin and adjacent ranges, Central Asia: tectonic implications, *Tectonophysics*, *221*, 251-267.

Bell, D.R, and Rossman, G.R., 1992. Water in the earth's mantle; the role of nominally anhydrous minerals, *Science, 255*, 1391-1397.

Bensen, G.D., Ritzwoller, M.H., Barmin, M.P., Levshin, A.L., Lin, F., Moschetti, M.P., Shapiro, N.M., and Yang, Y., 2007. Processing seismic ambient noise data to obtain reliable broad-band surface wave dispersion measurements, *Geophys. J. Int., 169*, 1239–1260.

Bielinski, R.A., Batalev, V., Jun S., Park, S.K., Rybin, A., and Sears, C., 2003. Lithospheric heterogeneity in the Kyrgyz Tien Shan imaged by magnetotelluric studies, *Geophys. Res. Lett*., *30*, *15*, doi:10.1029/2003GL017455.

Bird, P., 1979. Continental delamination and the Colorado Plateau, *J. Geophys. Res, 84*, 7561-7571.

Biske, Y.S., and Seltmann, R., 2010. Paleozoic Tian–Shan as a transitional region between the Rheic and Urals–Turkestan oceans, *Gondwana Research, 17*, 602–613.

Boyd, O.S., Jones, C.H., and Sheehan, A.F., 2004. Foundering Lithosphere Imaged Beneath the Southern Sierra Nevada, California, USA, *Science, 305, 5684*, 660-662, doi: 10.1126/science.1099181.

Burchfiel, B.C, and Royden, L.H., 1991. Tectonics of Asia 50 years after the death of Emile Argand, *Eclog. Geol. Helv., 84*, 599-629.

Burov, E.V., Kogan, M.G., Lyon-Caen, H., and Molnar, P., 1990. Gravity anomalies, the deep structure, and dynamic processes beneath the Tien Shan, *Earth Planet. Sci. Lett*., *96*, 367- 383.

Burov, E.V., and Molnar, P., 1998. Gravity anomalies over the Ferghana Valley (central Asia) and intracontinental deformation, *J. Geophys. Res*., *103*, *B8,* 18,137-18,152.

Burtman, V.S., 1975. Structural geology of the Variscan Tien Shan, USSR, *American Journal of Science*, *272A*, 157-186.

Burtman, V.S., Skobelev, S.F., and Molnar A.P., 1996. Late Cenozoic slip on the Talas-Fergana Fault, Tien Shan, Central Asia, *Geol. Soc. Am. Bull*., *108*, 1004-1021.

Buslov M.M., Klerkx, J., Abdarakhmatov, K., Delvaux, D., Batalev,VY., Kuchai, OA., Dehandschutter, D., and Muraliev, A., 2003. Recent strike-slip deformation of the northern Tien- Shan. In: Stori F, RE Holdsworth and F Salvini (eds). Intraplate strike-slip deformation belts, *The Geological Society, London Special Publications, 210*: 53-64

Cai, D.S., Lu, H.F., Jia, D., and Wu, S.M., 1995. Paleozoic plate tectonic evolution of southern Tianshan, *Chinese Geological Review, 41*, 432–442 (in Chinese with English abstract).

Carroll, A.R., Graham, S.A., Hendrix, M.S., Ying, D., and Zhou, D., 1995. Late Paleozoic tectonic amalgamation of northwestern China: sedimentary record of the northern Tarim, northwestern Turpan, and southern Junggar basins, *Geological Society of America Bulletin, 107*, 571–594.

Carroll, A.R., Graham, S.A., Chang, E.Z., and McKnight, C., 2001. Sinian through Permian tectonostratigraphic evolution of the northwestern Tarim basin, China. In: Hendrix, M.S., Davis, G.A. (Eds.), Paleozoic and Mesozoic Tectonic Evolution of Central and Eastern Asia, *Geological Society of American Memoir, 194*, 47–69.

Cawood, P.A., Kröner, A., Collins, W.J., Kusky, T.M., Mooney, W.D., and Windley, B.F., 2009. Earth Accretionary orogens through Earth history. In: Cawood, P.A., Kröner, A. (Eds.), Earth Accretionary Systems in Space and Time: *The Geological Society, London Special Publications, 318*, 1–36.

Charvet, J., Shu, L.S., and Laurent-Charvet, S., 2007. Paleozoic structural and geodynamic evolution of eastern Tianshan (NW China): welding of the Tarim and Junggar plates, *Episodes, 30*, 162–185.

Charvet, J., Shu, L.S., Laurent-Charvet, S., Wang, B., Faure, M., Cluzel, D., Chen, Y., and De Jong, K., 2011. Palaeozoic tectonic evolution of the Tianshan belt, NW China, *Science in China Series D: Earth Sciences, 54*, 166–184.

Chen, Y.H., Roecker, S.W., and Kosarev, G.L., 1997. Elevation of the 410 km discontinuity beneath the central Tien Shan: Evidence for a dethached lithospheric root, *Geophys. Res. Lett.*, *24*, 1531-1534.

Chen, C.M., Lu, H.F., Jia, D., Cai, D.S., and Wu, S.M., 1999. Closing history of the southern Tianshan oceanic basin, western China: an oblique collisional orogeny, *Tectonophysics, 302*, 23–40.

Clifford, A.A., 1975. Multivariate Error Analysis*, Wiley, New York*.

Cotton, F., and Avouac, J.P., 1994. Crustal and upper-mantle structure under the Tien Shan from surface wave dispersion, *Phys. Earth Planet. Inter*., *84*, 95-109.

Christensen, N.I., 1996. Poisson'sratio and crustal seismology, *J. Geophys. Res., 101, B2*, 3139-3156.

Dewey, J.F., Cande, S., and Pitman III, W.C., 1989. Tectonic evolution of the India/Eurasia collision zone. *Eclog. Geol. Helv,. 82*, 717-734.

Dziewonski, A.M., Bloch, S., and Landisman, M., 1969. A technique for the analysis of transient seismic signals, *Bull. Seism. Soc. Am., 59*, 427-444.

Engdahl, R., Van der Hilst, R., and Buland, R., 1998. Global teleseismic earthquake relocation with improved travel times and procedures for depth determination, *Bull. Seismol. Soc. Am., 88*, 722–743

England, P.C., and Houseman, G.A., 1985. Role of lithospheric strength heterogeneities in the Tectonics of Tibet and neighbouring regions, *Nature*, *315*, 297-301.

England, P., and Houseman, G., 1986. Finite strain calculations of continental deformation, 2, comparison with the India-Asia collision zone, *J. Geophys. Res*., *91*, 3664-36676.

England, P.C., and Houseman, G.A., 1989. Extension during continental convergence, with application to the Tibetan Plateau, *J. Geophys. Res., 94*, 17,561-17,579.

Fleitout, L., and Froidevaux, C., 1982. Tectonics and topography for a lithosphere containing density heterogeneities, *Tectonics*, *1*, 21-56.

Forsyth, W. D., and Li, A., 2005. Array analysys of two-dimensional variations in surface wave phase velocity and azimuthal anisotropy in the presence of multipathing interference, *Geophysical Minigraph Series, 157*, 10.1029/156GM06, 81-97.

Friedrich, A., Kruger, F., and Klinge, K., 1998. Ocean generated microseismic noise located with grafenberg array, *J. Seismol*., *2*, 47-64.

Fu, Y. V., Li, A., and Chen, Y. J., 2010. Crustal and upper mantle structure of southeast Tibet from Rayleigh wave tomography, *J. Geophys. Res*., *115*, *B12323*, doi:10.1029/2009JB007160.

Gan, W., Zhang, P., Shen, Z.K., Niu, Z., Wang, M. Wan, Y., Zhou, D., and Cheng, J., 2007. Present-day crustal motion within the Tibetan Plateau inferred from GPS measurements, *J. Geophys. Res., 112*, *B08416*, doi:10.1029/2005JB004120.

Ghose, S., Hamburger, M., and Virieux, J., 1998. Three-Dimensional Velocity Structure and Earthquake Locations beneath the Northern Tien Shan of Kyrgyzstan, Central Asia, *J. Geophys. Res*., *103, B2*, 2725-2748.

Graham, S.A., Hendrix, M.S., Hendrix, M.S., Wang, L.B., and Carroll, A.R., 1993. Collisional successor basins of western China: impact of tectonic inheritance on sand composition, *Geological Society of America Bulletin, 105*, 323–344.

Gripp, A.E., and Gordon, R.G., 2002. Young tracks of hotspots and current plate velocities, *Geophys. J. Int*., *150*, 321-364, doi:10.1046/j.1365-246X.2002.01627.x.

Hendrix, M.S., Graham, S.A., Carroll, A.R., Sobel, E.R., McKnight, C.L., Schulein, B.J., and Wang, Z., 1992. Sedimentary record and climatic implications of recurrent deformation in Tien Shan: evidence from Mesozoic strata of the north of Tarim, south Junggar, and Turpan basins, northwest China, *Geol. Soc. Amer. Bull*., *104*, 53-79.

Heubeck, C., 2001. Assembly of central Asia during the middle and late Paleozoic. In: Hendrix, M.S., Davis, G.A. (Eds.), Paleozoic and Mesozoic Tectonic Evolution of Central and Eastern Asia: *Geological Society of American Memoir, 194*, 1–22.

Houseman, G.A., McKenzie, D.P., and Molnar, P., 1981. Convective instability of a thickened boundary layer and its relevance for the thermal evolution of continental convergent belts, *J. Geophys. Res., 86, B7*, 6115-6132.

Huang, B.C., Piper, J.D.A., Wang, Y.C., He, H.Y., and Zhu, R.X., 2005. Paleomagnetic and geo-chronological constraints on the post-collisional northward convergence of the southwest Tian Shan, NW China, *Tectonophysics, 409*, 107–124.

Hyndman, R.D., and Peacock, S.M., 2003. Serpentinization of the forearc mantle, *Earth Planet. Sci. Lett*., *212*, 417-432.

Ingrin, J., and Skogby, H., 2000. Hydrogen in nominally anhydrous upper-mantle minerals: concentration levels and implications, *Eur. J. Mineral., 12*, 543-570.

Karato, S., 2003. Mapping Water Content in the Upper Mantle, inside the Subduction Factory: *Geophysical Monograph*, 138, pp.135-152, Copyright 2003 by the American Geophysical Union 10.1029/138GM08.

Karato, S., and Jung, H., 1998. Water, partial melting and the origin of seismic low velocity and high attenuation zone in the upper mantle, *Earth Planet. Sci. Lett*., *157*, 193-207.

Kay, R.W., and Kay, S.M., 1993. Delamination and delamination magmatism, *Tectonophysics, 219, 1–3*, 177–189

Kennett, B.L.N., Engdahl, E.R., and Buland, R., 1995. Constraints on seismic velocities in the Earth from travel times, *Geophys. J. Int., 122,* 108– 124.

Kondorskaya, V., and Shebalin, N., 1982. New Catalog of Strong Earthquakes in the USSR from Ancient Times Through 1977, pp. 608. World Data Cent, *A Solid-Earth Geophys*., Boulder, Colorado.

Kosarev, G.L., Petersen, N.V., Vinnik, L.P., and Roecker, S.W., 1993. Receiver functions for the Tien Shan analog broadband network: Contrasts in the evolution of structure across the Talas-Fergana fault, *J. Geophys. Res*., *98*, 4437-4448.

Kosarev, G., Kind, R., Sobolev, S.V., Yuan, X., Hanka, W., and Oreshin, S., 1999. Seismic Evidence for a Detached Indian Lithospheric Mantle Beneath Tibet, *Science, 283, 5406*, 1306-1309, doi: 10.1126/science.283.5406.1306

Kröner, A., Windley, B.F., Badarch, G., Tomurtogoo, O., Hegner, E., Jahn, B.M., Gruschka, S., Khain, E.V., Demoux, A., and Wingate, M.T.D., 2007. Accretionary growth and crust- formation in the Central Asian Orogenic Belt and comparison with the Arabian–Nubian shield. In: Hatcher Jr., R.D., Carlson, M.P., McBride, J.H., Martínez Catalán, J.R. (Eds.), 4-D Framework of Continental Crust: *Geological Society of America Memoir, 200*, 181–209.

Kumar, P., Yuan, X., Kind, R., and Kosarev, G., 2005. The lithosphere-asthenosphere boundary in the Tien Shan-Karakoram region from S receiver functions: Evidence for continental subduction, *Geophys. Res. Lett*., *32*, L07305, doi:10.1029/2004GL022291.

Lay, T., and Wallace, T.C., 1995. Modern Global Seismology, *Academic Press*.

Lebedev, S., and Nolet, G., 2003. Upper mantle beneath Southeast Asia from S velocity tomography, *J. Geophys. Res*., *108, B1*, 2048, doi:10.1029/2000JB000073.

Lei, J., and Zhao, D., 2007. Teleseismic P-wave tomography and the upper mantle structure of the central Tien Shan orogenic belt, *Phys. Earth planet. Inter*., *162*, 165-185.

Lei, J., 2011. Seismic tomographic imaging of the crust and upper mantle under the central and western Tien Shan orogenic belt, *J. Geophys. Res., 116*, B09305, doi:10.1029/2010JB008000.

Levshin, A.L., and Ritzwoller, M.H., 2001. Automated detection, extraction, and measurement of regional surface waves, *Pure Appl. Geophys., 158,8,* 1531–1545.

Li, A., 2011. Shear wave model of southern Africa from regional Rayleygh wave tomography with 2-D sensitivity kernels, *Geophys. J. Int.*, doi:10.1111/j.1365-246X.2011.04971.x.

Li, A., Forsyth, D.W., and Fisher, K.M., 2003. Shear velocity structure and azimuthal anisotropy beneath eastern North America from Rayleigh wave inversion, *J. Geophys. Res*., *108*, *B8*, 2362, doi:10.1029/2002JB002259.

Li, A., Forsyth, D.W., and Fisher, K.M., 2005. Rayleigh wavephase velocities and azimuthally anisotropic shear wave structure beneath the Colorado Rocky Mountains, Lithospheric Structure and Evolution of the Rocky Mountain Region, *AGU Monograph*, 154, pp385-401, eds K.E. Karlstrom and G.K. Keller, AGU, Washington, DC.

Li, A., and Chen, C., 2006. Shear wave splitting beneath the central Tien Shan and tectonic implications, *Geophys. Res. Lett*., *33*, L22303, doi:10.1029/2006GL027717.

Li, X.D., and Cui, X., 1994. Structures. In: Wang, B.Y., Lang, Z.J., Li, X.D., Qu, X., Li, T.F., Huang, C., Cui, X. (Eds.), Comprehensive survey of Geological Sections in the West Tian- shan of Xinjiang, *Science Press, China*, 126–168.

Li, Y., Liu, Q.Y., Chen, J.H., Li, S.C., Guo, B., and Lai, Y.G., 2007. Shear wave velocity structure of the crust and upper mantle underneath the Tianshan orogenic belt, *Sci. China, Ser. D: Earth Sci., 50, 3*, 321-330, doi:10.1007/s11430-007-0008-x.

Li, Z., Roecker, S., Zhihai, L., Bin, W., Haitao, W., Schelochkov, G., and Bragin, V., 2009. Tomographic image of the crust and upper mantle beneath the western Tien Shan from the MANAS broadband deployment: Possible evidence for lithospheric delamination, *Tectonophysics*, doi:10.1016/j.tecto.2009.05.007.

Lobkis, O. I., and Weaver, R. L., 2001. On the emergence of the Green's function in the correlations of a diffuse field, *J. Acoust. Soc. Am., 110, 6*, doi: 10.1121/1.1417528.

Long, X.P., Yuan, C., Sun, M., Zhao, G.C., Xiao, W.J., Wang, Y.J., Yang, Y.H., and Hu, A.Q., 2010. Archean crustal evolution of the northern Tarim craton, NW China: zircon U–Pb and Hf isotopic constraints, *Precambrian Research, 180*, 272–284.

Makarov, V. I., et al., 2010. Underthrusting of Tarim beneath the Tien Shan and Deep Structure of Their Junction Zone: Main Results of Seismic Experiment along MANAS Profile Kashgar–Song Köl, *Geotectonics*, *44*, No2, 102-126, doi10.1134/S0016852110020020.

Makeyeva, L.I., Vinnik, L.P., and Roecker, S.W., 1992. Shear wave splitting and small-scale convection in the continental upper mantle, *Nature*, *358*.

Menke, W., 1984. Geophysical data analysis : discrete inverse theory. *Academic press*.

Molnar, P., and Ghose, S., 2000. Seismic moments of major earthquakes and the rate of shortening across the Tien Shan, *Geophys. Res. Lett*., *27*, *16*, 2377-2380.

Molnar, P., and Tapponier, P., 1975. Cenozoic tectonics of Asia: effects of a continental collision, *Science*, *189*, 419-426.

Jean-PauMontagner, J.P, and Nataf, F.H.C., 1986. A simple method for inverting the azimuthal anisotropy of surface waves, *J. Geophys. Res., 91, B1*, 511-520.

Neil, E.A., and Houseman, G., 1997. Geodynamics of the Tarim basin and the Tien Shan in central Asia, *Tectonics*, *16*, 571-584.

Nicolas, A., and Christensen, N.I., 1987. Formation of anisotropy in uppermantle peridotites—a review, in The Composition, Structure and Dynamics of the Lithosphere-Asthenosphere System, *American Geophysical Union Geodynamics Series, edited by C. Froidevaux and K. Fuchs*, 111-123.

Niu, Z., et al. 2005. Contemporary velocity field of crustal movement of Chinese mainland from Global Positioning System measurements, *Chin. Sci. Bull.*, *50, 9*, 939-941.

Oreshin, S., Vinnik, L., Peregoudov, D., and Roecker, S., 2002. Lithosphere and asthenosphere of the Tien Shan imaged by S receiver functions, *Geophys. Res. Lett*., *29*, (8) doi:1029/2001GL014441.

Patriat, P., and Achache, J., 1984. India–Eurasia collision chronology has implications for crustal shortening and driving mechanism of plates, *Nature, 311*, 615-621 doi:10.1038/311615a0.

Park, J., and Levin, V., 2002. Seismic anisotropy: tracing plate dynamics in the mantle, *Science, 296*, 485–489.

Press, W.H., Teukolsky, S.A., Vetterling, W.T., and Flannery, B.P., 1992. Numerical Recipes in FORTRAN: The Art of Scientific Computing (2nd edition), *Cambridge Univ. Press, Cambridge*, 963 pp.

Pyle, M. L., D. A. Wiens, D. S. Weeraratne, P. J. Shore, H. Shiobara, and H. Sugioka, 2010. Shear velocity structure of the Mariana mantle wedge from Rayleigh wave phase velocities, *J. Geophys. Res.*, *115*, B11304, doi:10.1029/2009JB006976.

Reigber, Ch., Michel, G.W., Galas, R., Angermann, D., Klotz, J., Chen, J.Y., Papschev, A., Arslanov, R., Tzurkov, V.E., and Ishanov, M.C., 2001. New space geodetic constraints on the distribution of deformation in Central Asia, *Earth Planet. Sci. Lett.*, *191*, 157-165.

Ren, R., Han, B.-F., Ji, J.-Q., Zhang, L., Xu, Z., and Su, L., 2011. U–Pb age of detrital zircons from the Tekes River, Xinjiang, China, and implications for tectonomagmatic evolution of the South Tian Shan Orogen. *Gondwana Research, 19*, 460–470.

Rhie, J., and Romanowicz, B., 2004. Excitation of Earth's continuous free oscillations by atmosphere-ocean-seafloor coupling, *Nature, 431*, 552-556.

Ritzwoller, M.H., 2009. Ambient noise seismic imaging, *McGraw Hill Yearbook of Science and Technology*.

Roecker, S.W., Sabitova, T.M., Vinnik, L.P., Burmakov, Y.A., Golvanov, M.I., Mamatkanova, R., and Munirova, L., 1993. Three-Dimensional elastic wave velocity structure of the western and central Tien Shan, *J. Geophys. Res.*, *98*, 15,779-15,795.

Roecker, S.W., 2000. Crustal thickness and mantle anisotropy of the western Tien Shan from the analysis of GHENGIS broadband seismic data, *EOS Trans, AGU*, *81* (48).

Sabra, K., Gerstoft, G. P., Roux, P., Kuperman, W.A., and Fehler, M.C., 2005a. Extracting time-domain Green's function estimates from ambient seismic noise, *Geophys. Res. Lett., 32, L03310*, doi:10.1029/2004GL021862.

Sabra, K., Gerstoft, G., Roux, P., Kuperman, W.A., and Fehler, M.C., 2005b. Surface wave tomography from microseism in southern California, *Geophys. Res. Lett., 32*, L14311, doi:10.1029/2005GL023155.

Saito, M., 1988. DISPER80: a subroutine package for the calculation of seis- mic normal-mode solutions, in *Seismological Algorithms*, pp. 293–319, ed. Doornbos, D.J., Elsevier, New York, NY.

Saltzer, R. L., 2002. Upper mantle structure of the Kaapvaal craton from surface wave analysis – a second look, *Geophys. Res. Letts., 29, 6*, 1093, 10.1029/2001GL013702.

Schott, B., and Schmeling, H., 1998. Delamination and detachment of a lithospheric root,

Tectonophysics, 296, 3-4, 225-247.

Schreiber, D., Lardeaux, J.M., Martelet, G., Courrioux, G., and Guillen, A., 2010. 3-D modelling of Alpine Mohos in Southwestern Alps, *Geophys. J. Int. 180, 3*: 961-975 doi:10.1111/j.1365-246X.2009.04486.x

Shapiro, N.M., and Campillo M., 2004. Emergence of broadband Rayleigh waves from correlations of the ambient seismic noise, *Geophys. Res. Lett., 31*, L07614, doi:10.1029/2004GL019491.

Shapiro, N.M., Campillo, M., Stehly, L., and Ritzwoller, M.H., 2005. High-Resolution Surface wave Tomography from Ambient Seismic Noise, *Science*, 10.1126/science.1108339.

Searle, M.P., Windley, B. F., Coward, M. P., Cooper, D.J.W., Rex, A. J., Rex, D., Li, T., Xiao X., Jan, M.Q., Thakur, V.C., and Kumar, S., 1987. The closing of Tethys and the tectonics of the Himalaya, *Geological Society of America Bulletin 98, 6;* 678-701 doi: 10.1130/0016-7606.

Shu, L.S., Yu, J.H., Charvet, J., Laurent-Charvet, S., Sang, H.Q., and Zhang, R.G., 2004. Geological, geochronological and geochemical features of granulites in the Eastern Tianshan, NW China, *Journal of Asian Earth Sciences, 24*, 25–41.

Shu, L.S., Deng, X.L., Zhu, W.B., Ma, D.S., and Xiao, W.J., 2011. Precambrian tectonic evolution of the Tarim Block, NW China: new geochronological insights from the Quruqtagh domain, *Journal of Asian Earth Sciences, 42*, 774–790.

Smith, M.L., and Dahlen, F.A., 1973. The azimuthal dependence of Love and Rayleigh wave propagation in a slightly anisotropic medium, *J. Geophys. Res.*, *78*, 3321-3333.

Sobel, E., and Dumitru, T. A., 1997. Thrusting and exhumation around the margins of the western Tarim basin during the India-Asia collision, *J. Geophys. Res*., *102*, 5043-5063.

Steffen, R., Steffen, H., and Jentzsch, G., 2011. A three-dimensional Moho depth model for the Tien Shan fom EGM2008 gravity data, *Tectonics*, *30*, *TC5019*, doi:10.1029/2011Tc002886.

Stehly, L., Fry, B., Campillo, M., Shapiro, N.M., Guilbert, J., Boschi, L., and Giardini, D., 2009. Tomography of the Alpine region from observations of seismic ambient noise, *Geophys. J. Int., 178, 338–350,* doi: 10.1111/j.1365-246X.2009.04132.x

Tarantola, A., and Valette, B., 1982. Generalized non-linear problems solved using the least- squares criterion, *Rev. Geophys. Sp. Phys*., *20*, 219-232.

Tapponier, P., and Molnar, P., 1979. Active faulting and Cenozoic tectonics of Tien Shan, Mongolia and Baikal regions, *J. Geophys. Res*., *84*, 3425-3459.

Tapponnier, P., Peltzer, G., and Armijo, R., 1986. On the mechanics of the collision between India and Asia, in Collision Tectonics, edited by J. G. Ramsay, M. P. Coward, and A. C. Ries, *Geol. Soc. Spec. Publ., 19*, 115–157.

Thomas, J.C., Chauvin, A., Gapais, D., Bazhenov, M.L., Perroud, H., Cobbold, P.R., and Burtman, V.S., 1994. Paleomagnetic evidence for Cenozoic block rotations in the Tadjik depression (Central Asia), *J. Geophys. Res., 99*, 15141-15160.

Thompson, S.C., Weldon, R.J., Rubin, C.M., Abdrakhmatov, K., Molnar, P., and Berger, G.W., 2002. Late Quaternary slip rates across the central Tien Shan, Kyrgyzstan, Central Asia, *J. Geophys. Res., 107, B9*, 2203 http://dx.doi.org/10.1029/2001JB000596.

Tian, X., D. Zhao, H. Zhang, Y. Tian, and Z. Zhang, 2010. Mantle transition zone topography and structure beneath the central Tien Shan orogenic belt, *J. Geophys. Res., 115*, B10308, doi:10.1029/2008JB006229.

Trapeznikov, Y.A., Andreeva, E.V., Batalev, V.Y., Berdichevsky, M.N., Vanyan, L.L., Volykhin, A.M., Golubtsova, N.S., and Rybin, A.K., 1997. Magnetotelluric soundings in the Kyrgyz Tien Shan, *Phys. Solid Earth*, *33*, 1- 17.

Vinnik, L., Peregoudov, D., Makeyeva, L., Oreshin, S., and Roecker, S., 2002. Towarsd 3-D fabric in the continental lithosphere and asthenosphere: the Tien Shan, *Geophys. Res. Lett*., *29*, *16*, doi:10.1029/2001GL014588.

Vinnik, L.P., Reigber, C., Aleshin, I.M., Kosarev, G.L., Kaban, M.K., Oreshin, S.I., and Roecker, S.W., 2004. Receiver function tomography of the central Tien Shan, *Earth Planet. Sci. Lett*., *225*, 131-146.

Vinnik, L.P., Aleshin, I.M., Kaban, M.K., Kiselev, S.G., Kosarev, G.L., Oreshin, S.I., and Reigber, Ch., 2006. Crust and Mantle of the Tien Shan from Data of the Receiver Function Tomography, *Phys. of Solid Earth*, *42*, *8*, 639-651.

Wang, Q., Shu, L., Charvet, J., Faure, M., Ma, H., Natal'in, B., Gao, J., Kroner, A., Xiao, W., Li, J., Windley, B., Chen, Y., Glen, R., Jian, P., Zhang, W., Seltmann, R., Wilde, S., Choulet, F., Wan, B., Quinn, C., Rojas-Agramonte, Y., Wang, B., Lin, W., 2010. Understanding and study perspectives on tectonic evolution and crustal structure of the Paleozoic Chinese Tianshan: report on the international excursion and workshop, Urumqi, China. *Episodes, 33*, 242–266.

Wessel, P., and Smith, W.H.F., 1998. New, improved version of the Generic Mapping Tools Released, *EOS Trans., AGU, 79*, 579.

Williams, Q., and Hemley, R.J., 2001. Hydrogen in the deep earth: *Annual Reviews of Earth and Planetary Science, 29*, 365-418, doi:10.1146/annurev.earth.29.1.365.

Windley, B.F., Allen, M.B., Zhang, C., Zhao, Z.Y., and Wang, G.R., 1990. Paleozoic accretion and Cenozoic redeformation of the Chinese Tien Shan Range, Central Asia, *Geology,* 18, 128–131.

Windley, B.F., Alexeiev, D., Xiao, W., Kröner, A., and Badarch, G., 2007. Tectonic models for accretion of the Central Asian Orogenic belt, *Journal of the Geological Society, London, 164*, 31–47.

Wolfe, C.J., and Vernon III, F.L., 1998. Shear wave splitting at central Tien Shan: Evidence for rapid variation of anisotropic patterns, *Geophys. Res. Letts.*, *25*, no 8, 1217-1220.

Xiao, W.J., Windley, B.F., Badarch, G., Sun, S., Li, J.L., Qin, K.Z., and Wang, Z.H., 2004a. Palaeo- zoic accretionary and convergent tectonics of the southern Altaids: implications for the lateral growth of Central Asia, *Journal of the Geological Society of London, 161*, 339–342.

Xiao, W.J., Zhang, L.C., Qin, K.Z., Sun, S., and Li, J.L., 2004b. Paleozoic accretionary and colli- sional tectonics of the Eastern Tianshan (China): implications for the continental growth of central Asia, *American Journal of Science, 304*, 370–395.

Xiao, W.J., Windley, B.F., Huang, B.C., Han, C.M., Yuan, C., Chen, H.L., Sun, M., Sun, S., and Li, J.L., 2009. End-Permian to mid-Triassic termination of the accretionary processes of the southern Altaids: implications for the geodynamic evolution, Phanerozoic continental growth, and metallogeny of Central Asia, *International Journal of Earth Sciences, 98*, 1189–1287.

Xiao, W.J., Huang, B.C., Han, C.M., Sun, S., and Li, J.L., 2010a. A review of the western part of the Altaids: a key to understanding the architecture of accretionary orogens, *Gondwana Research, 18,* 253–273.

Xiao, W.J., Mao, Q.G., Windley, B.F., Qu, J.F., Zhang, J.E., Ao, S.J., Guo, Q.Q., Cleven, N.R., Lin, S.F., Shan, Y.H., and Li, J.L., 2010b. Paleozoic multiple accretionary and collisional processes of the Beishan orogenic collage, *American Journal of Science, 310*, 1553–1594.

Xiao, W., Windley, B.F., Allen, M.B., and Han, C., 2012. Paleozoic multiple accretionary and collisional tectonics of the Chinese Tianshan orogenic collage, *Gondwana Res.*, doi:10.1016/j.gr.2012.01.012

Xu, Y., Liu, F., Liu, J., and Chen, H., 2002. Crust and upper mantle structure beneath western China from *P* wave travel time tomography, *J. Geophys. Res*., *107*, *B10*, 2220, doi:10.1029/2001JB000402.

Xu, Y., Roecker, S.W., Wei, R., Zhang, W., and Wei, B., 2006. Analysis of Seismic Activity in the Crust from Earthquake Relocation in the Central Tien Shan, *Bull. Seism. Soc. Am.*, *96*, No. 2, 737-744, doi:10.1785/0120030220.

Xu, Y., Li, Z., and Roecker, S.W., 2007. Uppermost mantle structure and its relation with seismic activity in the central Tien Shan, *Geophys. Res. Lett*., *34*, L10304, doi:10.1029/2007GL029708.

Yang, X., Pavlis, G.L., Roecker, S.W., and Vernon, F.L., 2003. Teleseismic tomographic images of the central Tien Shan, *EOS-Trans., AGU, 84*, 1057.

Yang, Y., and Liu, M., 2002. Cenozoic deformation of the Tarim plate and the implications for mountain building in the Tibetan Plateau and the Tian Shan, *Tectonics*, *21*, NO 6, 1059, doi:10.1029/2001TC001300.

Yang, Y., and Forsyth, D.W., 2006. Rayleigh wave phase velocities, small scale convection, and azimuthal anisotropy beneath southern California, *J. Geophys. Res*., *111*, (B07306), doi:10.1029/2005JB004180.

Yang, Y., Ritzwoller, M.H., Levshin, A.L., and Shapiro, N.M., 2007. Ambient noise Rayleigh wave tomography across Europe, *Geophys. J. Int., 168*, 259–274.

Yao, H., Van der Hilst, R.D., and De Hoop, M.V., 2006. Surface wave tomography in SE Tibet from ambient seismic noise and two-station analysis: I.—Phase velocity maps, *Geophys. J. Int., 166*, 732–744, doi: 10.1111/j.1365–246X.2006.03028.x.

Yao, H., and Van der Hilst, R.D., 2009. Analysis of ambient noise energy distribution and phase velocity bias in ambient noise tomography, with application to SE Tibet, *Geophys. J. Int. 179*, 1113–1132, doi: 10.1111/j.1365-246X.2009.04329.x

Zheng, B.H., Zhu, W.B., Jahn, B.M., Shu, L.S., Zhang, Z.Y., and Su, J.B., 2010. Subducted Pre- cambrian oceanic crust: geochemical and Sr–Nd isotopic evidence from metaba- salts of the Aksu blueschist, NW China, *Journal of the Geological Society of London, 167*, 1161–1170.

Zhao, D., Hasegawa, A., and Horiuchi, S., 1992. Tomographic imaging of P and Swave velocity structure beneath northeastern Japan, *J. Geophys. Res., 97*, 19,909-19,928.

Zhao, J., Liu, G., Lu, Z., Zhang, X., and Zhao, G., 2003. Lithospheric structure and dynamic processes of the Tien shan orogenic belt and the Junggar basin, *Tectonophysics*, *376*, 199- 239.

Zhou, Y., Dahlen, F.A., Nolet, G., and Laske, G., 2005. Finite-frequency effects in global surface wave tomography, *Geophys. J. Int*, *163*, 1087-1111. Doi:10.1111/j.1365-246X.2005.02780.x.

Zhou, Y., F. A. Dahlen, and G. Nolet, 2004. 3-D sensitivity kernels for surface wave observables, *Geophys. J. Int., 158*, 142–168.